Application of fractional order system in the acoustics domain : Modeling and synthesis of a wind instrument

Gaby Abou Haidar

université de BORDEAUX

THÈSE

PRÉSENTÉE À

L'UNIVERSITÉ DE BORDEAUX

ÉCOLE DOCTORALE DES SCIENCES PHYSIQUES ET DE L'INGÉNIEUR

par

Gaby ABOU HAIDAR

POUR OBTENIR LE GRADE DE

DOCTEUR

SPÉCIALITÉ : AUTOMATIQUE

Systèmes à Dérivées Non Entières dans le domaine de l'acoustique: étude des pertes viscothermiques dans un instrument à vent

---

Soutenance prévue le 15 Juillet 2021

Après avis de :

Valérie BUDINGER,	Professeur à l'Institut Supérieur de l'Aéronautique et de l'Espace, ISAE
Clovis FRANCIS,	Professeur à l'Université Libanaise

Devant la Commission d'examen formée de :

Valérie BUDINGER,	Professeur à l'ISAE	*Rapporteur*
Clovis FRANCIS,	Professeur à l'Université Libanaise	*Rapporteur*
Rachid MALTI,	Professeur à l'Université de Bordeaux	*Examinateur*
Roy ABI ZEID DAOU,	Professeur associé à la Lebanese German University	*Co-encadrant*
Xavier MOREAU,	Professeur à l'Université de Bordeaux	*Directeur de thèse*

Avant-Propos

Cette thèse s'inscrit dans le cadre d'une collaboration internationale entre Lebanese German University (LGU), American University of Science and Technology (AUST) et l'Université de Bordeaux (UBx), au sein de l'équipe CRONE du Groupe Automatique du laboratoire IMS, UMR 5218 du CNRS.

Cette collaboration a débuté en 2008 (figure 1) avec Clovis FRANCIS, aujourd'hui Professeur à l'Université Libanaise et membre du Conseil National de la Recherche Scientifique du Liban (CNRS-L). En 13 ans, cette collaboration internationale a donné lieu à 4 thèses soutenues, 1 thèse en cours (objet de ce mémoire), une prochaine thèse (septembre 2021), une HDR en cours de préparation, 13 publications dans des Revues Internationales avec Comité de Lecture (RICL), 33 communications dans des Conférences Internationales avec Comité de Lecture (CICL), 5 chapitres d'ouvrages, 2 ouvrages de synthèse, …

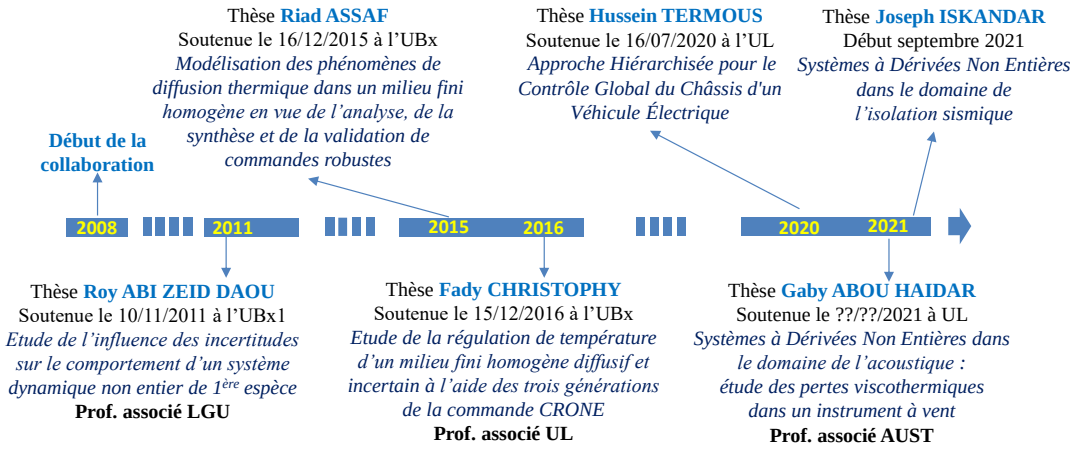

Figure 1 – Chronogramme illustrant 13 ans de collaboration avec le Liban

Les travaux présentés dans ce mémoire de thèse concernent les Systèmes à Dérivées Non Entières (SDNE) dans le domaine de l'acoustique avec l'étude des pertes viscothermiques dans un instrument à vent.

Contrairement aux travaux menés, par exemple, à l'IRCAM (*Institut de Recherche et Coordination Acoustique/Musique)* ou dans des laboratoires d'acoustique, les travaux présentés dans ce mémoire de thèse n'abordent pas le sujet sous l'angle de l'acoustique musicale, mais sous l'angle de l'Automatique, c'est-à-dire l'étude de la dynamique des systèmes complexes. La flûte à bec ne constitue qu'un support dont le domaine d'étude défini dans ce mémoire est beaucoup plus restreint que celui envisageable avec un instrument à vent.

Organisation et Contenu de la Thèse

Le mémoire de thèse comporte quatre chapitres dont la logique d'enchainement est illustrée à l'aide de la Figure 2.

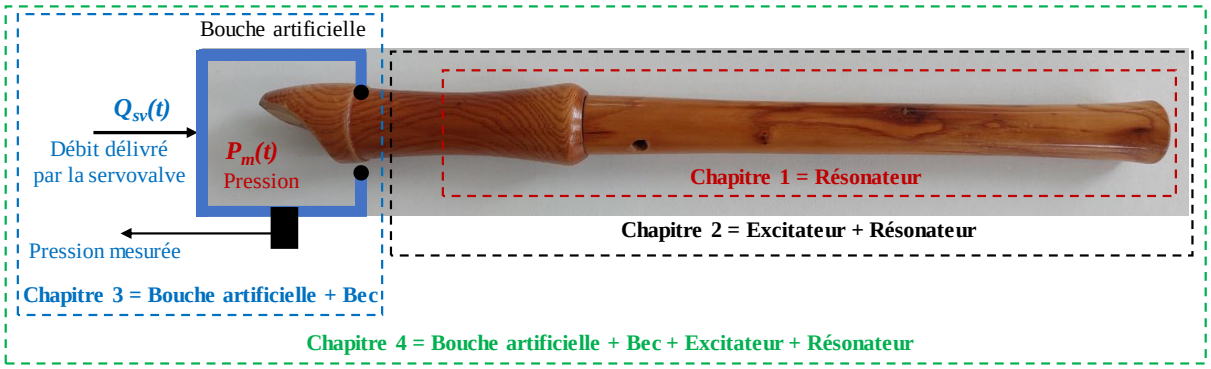

Figure 2 – Illustration de la progression et de la logique d'enchainement des chapitres du mémoire de thèse

Ainsi, le ***chapitre 1***, intitulé: « ***Etude des pertes viscothermiques au sein du résonateur d'un instrument à vent*** », est consacré, dans un premier temps, à la modélisation du résonateur seul en tant que tube acoustique (tous les trous permettant de faire varier la longueur apparente sont supposés fermés), modélisation qui aboutit à l'impédance générale $Y(x,s,L)$ (débit/pression) du résonateur en fonction, notamment, de la longueur L et de la position x comprise entre 0 (entrée du résonateur) et L (sortie du résonateur). Ensuite, une approche système (au sens de l'Automatique) permet de décomposer l'impédance d'entrée $Y_{in}(s,L) = Y(0,s,L)$ en sous-systèmes, facilitant ainsi l'analyse notamment lors du passage d'un système semi-infini à un système fini. De plus, l'introduction d'une extension de l'expression fractionnaire utilisée pour la prise en compte des pertes viscothermiques, où l'ordre m est habituellement égal à 0.5, permet de faire une première analyse de l'influence de l'ordre m, compris en 0 (système conservatif) et 1, sur la réponse fréquentielle de l'impédance du résonateur. Enfin, ce chapitre se termine par la présentation d'une méthode permettant de passer de la forme fractionnaire de l'impédance à ses formes rationnelles cascade et parallèle indispensables pour la simulation temporelle.

Le ***chapitre 2***, intitulé: « ***Etude du couplage entre l'excitateur non linéaire et le résonateur d'un instrument à vent*** », est dédié, dans le cas habituel où l'ordre m est égal à 0.5, à l'étude du couplage entre l'excitateur non linéaire et le résonateur. Sur la base d'une synthèse bibliographique, un modèle non linéaire fréquemment utilisé dans la littérature est développé. Ensuite, après avoir insisté sur le mauvais conditionnement numérique d'un tel modèle, une solution est proposée permettant la mise en oeuvre d'un simulateur numérique programmé sous MatLab/Simulink. Pour un domaine d'étude défini par une pression constante à l'entrée du bec de flûte bornée par une valeur minimale de 400 Pa et une valeur maximale de 1000 Pa, une analyse détaillée des réponses temporelles simulées met en évidence la présence de trois phases durant lesquelles les variations

- de la pression à l'entrée du résonateur,
- de la vitesse acoustique
- et du déplacement latéral du jet d'air

restent petites autour de zéro. Ce constat permet le développement de manière légitime et réaliste de deux modèles linéarisés, l'un pour l'analyse de la phase de démarrage de la simulation, l'autre pour celle de la phase des auto-oscillations (régime périodique stationnaire), facilitant ainsi la compréhension des phénomènes mis en jeu.

Le ***chapitre 3***, intitulé: « ***Conception et implémentation d'une bouche artificielle pour un instrument à vent*** », se focalise sur la démarche de conception et sur l'implémentation d'une bouche artificielle nécessaire pour contrôler la pression à l'entrée du bec de flûte. Durant la phase de conception, un premier simulateur a été développé sur la base d'une synthèse bibliographique concernant les bouches artificielles utilisées en acoustique musicale. Ce premier simulateur a permis de bien comprendre le fonctionnement d'un tel système, facilitant ainsi le choix et le dimensionnement des composants de la boucle de régulation (servovalve de débit, capteurs de débit et de pression, volume de la capacité pneumatique,…). A l'issue de la réalisation de la bouche artificielle, un travail de modélisation de ce dispositif expérimental a conduit à un deuxième simulateur. Ce dernier a fait l'objet d'un recalage à partir de comparaisons entre des résultats expérimentaux et de simulation. Ainsi, pour une flûte à bec bien réelle (en plastique dont la longueur du résonateur L = 30 cm, son rayon moyen r = 5 mm, l'ordre fractionnaire associé aux pertes viscothermiques m = 0.5, avec une fenêtre de l'excitateur dont les dimensions sont 1 cm x 0.4 cm, une hauteur du canal du bec h = 1 mm,…), le simulateur reproduit avec une bonne précision les conditions d'étude spécifiées au chapitre 2. Ce comportement bien réel (reproduit en simulation) est considéré au chapitre 4 comme le comportement nominal de référence.

Enfin, l'objectif du ***chapitre 4***, intitulé: « ***Analyse de l'influence de l'ordre fractionnaire sur le régime périodique stationnaire*** », est d'étudier l'influence de l'ordre m compris entre 0 et 1, autour de sa valeur nominale m_0 = 0.5, sur le régime périodique stationnaire. Ce chapitre commence par présenter l'organisation du simulateur global développé sous MatLab/Simulink à partir des travaux présentés dans les trois premiers chapitres. Ensuite, une analyse dans le domaine fréquentiel de l'influence de l'ordre m est développée, d'abord dans le cas de l'impédance du résonateur établie au chapitre 1, puis dans le cas de la fonction de transfert en boucle ouverte définie au chapitre 2. Cette analyse se poursuit dans le domaine temporel avec les réponses issues du simulateur global en reprenant les scénarios des deux exemples du chapitre 2. Ainsi, à partir de l'extension du modèle fractionnaire proposée au chapitre 1, il est possible avec un seul paramètre de haut niveau, l'ordre m en l'occurrence, de faire varier facilement les pertes viscothermiques, alors que d'un point de vue expérimental, il faudrait fabriquer et tester un nombre important de résonateurs avec des dimensions, des rugosités et des matériaux différents.

Xavier MOREAU
Directeur de thèse

Achnowledgment

My great and sincere thanks go to my supervisors Prof. Xavier Moreau and Dr. Roy Abi Zeid Daou, who provided valuable and continuous support and guidance during the course of this research project.

I would like to thank my committee members Professor Valerie Budinger, Professor Clovis Francis and Professor Rachid Malti for reviewing and reporting my thesis.

This study would not have been possible without the financial support provided by the University of Bordeaux - IMS Laboratory that were related to conference and accommodation fees, different types of precise sensors and actuators, in addition to travel fees.

A sincere thanks also goes to the American University of Science and Technology - Zahle Branch that supported me with all the laboratory resources and facilities during my four years' research process.

I would also like to express the deepest appreciation to the President of the American University of Science and Technology Dr. Hiam Sakr for her encouragement and continuous support.

Finally, I would like to express gratitude to my dear mother, sister, and brothers for their constant moral and financial support.

Motivation

Music has always been the source of creativity and imagination for most thinkers and a relaxing tool for stress and depression. The greatest minds and thinkers like Albert Einstein, Mozart, and Frank Lloyd Wright all had something in common in that they were constantly exploring their imagination and creativity through music to make discoveries, innovations and many other different fields. Music and sound synthesis are two faces for the same coin. Sound synthesis started with the wish to generate any kind of music (or sound) using mathematical techniques, and by research improvement, it became possible to generate or transform any sound conceivable. The available sound synthesis techniques are capable of a perfect reproduction of sound but not actually a perfect generation of a sound; this is why model-based digital instruments should be available. The main advantage behind model-based synthesis is the more control over the physical variables (which influence the sound reproduction) it gives for the player.

Thus, this work aims to model and control a flute wind musical instrument for better numerical performance. To have a completely automated system, the mouth and the flute musical instrument parts will be modeled and implemented. So, based on the delivered air pressure by the artificial mouth, a certain frequency will be generated from the instrument.

To achieve the preset goal, the physical implementation of the artificial mouth is first established. Then, a study for every part of the flute will be conducted, starting by the resonator and then the exciter. This resonator is of a particular importance as it has been shown that the air flow within its boundaries is subject to visco-thermal losses that are being modeled by a fractional transfer function of order 0.5.

The last stage of this work will be to confront the already presented theoretical study with the experimental measurements and the implementation of a system that most closely resembles the real system. Note that this Ph.D. thesis will be the first block in a much larger project that will aim to reach the final objective already listed. Thus, the outcome of this work is not to have a complete autonomous system as a first step but to be able to model this complicated system and to generate sound while controlling the mouth pressure and/or flow.

List of Abbreviations

CRONE	Command Robuste d 'Order Non Entier
PID	Proportional Integrator Derivative
v	Speed of light
p	Accoustic Pressure
U	Particle Velocity
k	wave number
J_m	Bessel Function
ζ	Damping Factor
γ	Normalized elastic material constant.
dB	Decibel
w	Angular Frequency
$\omega_{r,m}$	Transitional Frequency
$h(t)$	Impulse response
$Q_v(t)$	Air Flow
Q	Resonance Factor
ε	Visco-thermal losses
γ	Specific Heat Ratio
S	Cross Section
s	Laplace variable
$\Gamma(j\omega)$	Complex Wave Number
$tanh$	Tangent hyperbolic function
L	Length
r	Radius
Y	Acoustic Admittance
Z	Acoustic Impedance
H	Transfer Function
αi	Amplification Factor
C_v^e	Convection speed

Table of Contents

List of Figures

General Overview

1 – Introduction

The flute wind instrument family encompasses an extensive range of instrument types, each exhibiting notable differences in terms of sound production, instrument geometry, materials used, and their respective musical contexts (Terrien, 2015). Notched flutes such as the Latin American quena and the Japanese shakuhachi, along with pan flutes and globular flutes like the ocarina, are part of this diverse family. Additionally, transverse flutes, recorders, and mouth organ pipes contribute to the rich variety of instruments in this category.

One notable aspect highlighting the diversity within this family is the varying influence of the instrument itself and the musician on the instrument's geometry, and subsequently, sound production. Instruments like the recorder or mouth organ pipes have fixed geometries, determined by the instrument builder during construction. However, in flute types such as the quena or transverse flutes, the musician has the freedom to adapt geometric parameters while playing, as the channel is formed by the musician's lips. This flexibility grants the player more autonomy but poses challenges in controlling the instrument effectively.

Despite the multitude of instrument types within the flute family, they share a common mechanism for producing sound, involving the oscillation of an air jet around a bevel. This mechanism forms the foundation for generating the characteristic sounds associated with flutes, regardless of the specific instrument's design or playing technique employed. A state of the art of the different wind musical instruments, the sound formation, the main components of the flute and the problem statement will be discussed in the following sections of this general overview.

2 – Wind Musical Instrument

In this section, the human voice will be presented as it is the main source for the generation of sound. The voice is one of the most colorful interfaces for musical expression. It is certainly the most personal of all instruments (each voice is unique) – and the only one capable of presenting both words and musical sound simultaneously. Voices are classified by their tone-color, register and range. One can identify the following groups (FactMonster, 2001):

- *soprano:* highest female voice;
- *mezzo-soprano:* rich female voice mixing soprano and alto colors;
- *contralto or "alto":* lowest female voice;
- *countertenor:* a very high male voice;

• *tenor:* high male voice;

• *baritone:* rich male voice mixing tenor and bass colors;

• *bass:* very low male voice;

Hereafter, the different families of the wind musical instruments will be presented. For each family, the corresponding instruments will be shown along with their properties.

2.1 – Woodwind Family

The woodwind family as in Figure 3 is composed of wooden instruments that the player must blow into to create a musical sound. Most members of the modern woodwind family are "reed" instruments (a piece of wooden reed attached to its mouthpiece that adds character to the sound). The complete woodwind family became a standard part of the orchestra by the early 1800's. Common woodwind instruments include (FactMonster, 2001) :

• the piccolo (very high) and various-sized flutes;

• the oboe and the "English" Horn (a tenor oboe);

• the bassoon and contrabassoon (very low bassoon);

• various-sized clarinets;

• various-sized saxophones;

• various-sized recorders (ancestors to the modern flute family);

The standard range categorization of this family is the *flute* (soprano), the *oboe* (alto), the *clarinet* (tenor) and the *bassoon* (bass).

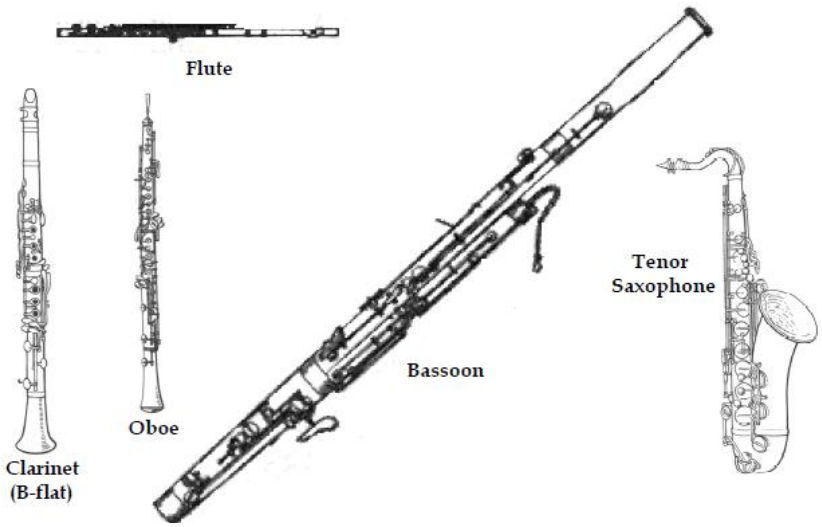

Figure 3 – Common Woodwind Instruments

2.2 – Brass Family

The brass family in Figure 4 is composed from powerful metallic instruments that must be blown into by the player to produce a musical sound. The tone-color (timbre) of most brass instruments can be altered by the use of various types of mutes which are inserted into the large end of the instrument. Until the invention of the valve, brass instruments could only produce a limited number of pitches, which lessened their usefulness to composers. Instrument builders experimented with various valves that would avail more pitch varieties to these instruments.

Many modern brass instruments have a system of three valves that can be combined in various combinations to produce different pitches. The modern "rotary" valve was invented in the early romantic period (c. 1830) – an invention that made the brass family more responsive and reliable. As a result, romantic composers made greater use of the brass family. The most common types of brass instruments include (FactMonster, 2001):

- various-sized trumpets (use valves to change pitch);
- various-sized trombones (use a slide instead of valves to change pitch);
- the "French Horn" (use valves to change pitch);
- the Tuba—a very low brass instrument (uses valves to change pitch);

The standard range categorization of this family is the *trumpet* (soprano), the *alto trombone* (alto), the *tenor trombone* that is equivalent to the *upper french horn* (tenor), the *bass trombone* that is equivalent to the *low french horn* (bass).

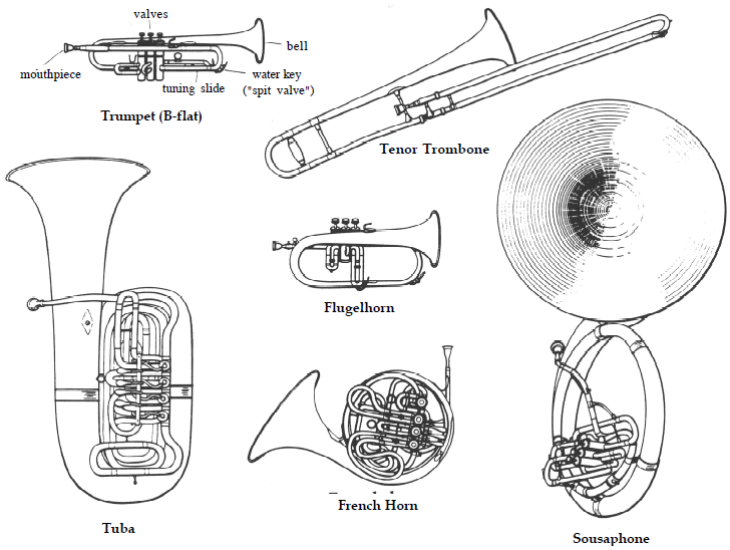

Figure 4 – Common Brass Instruments

2.3 – Flute Musical Instrument

The initial stages of modeling and understanding the functioning of flute-like instruments can be traced back to separate works conducted by Mersenne and Bernoulli (De la Cuadra, 2005). Their studies focused on analyzing the resonance frequencies of the instrument's bore. This approach remains relevant today and provides valuable insights into various construction properties, including the position and diameter of the resonator, height of the chimney, tone hole placements, and shape corrections. Please refer to Figure 5 for further details (Mersenne, 1636) (Bernoulli, 1762) (Terrien, 2015).

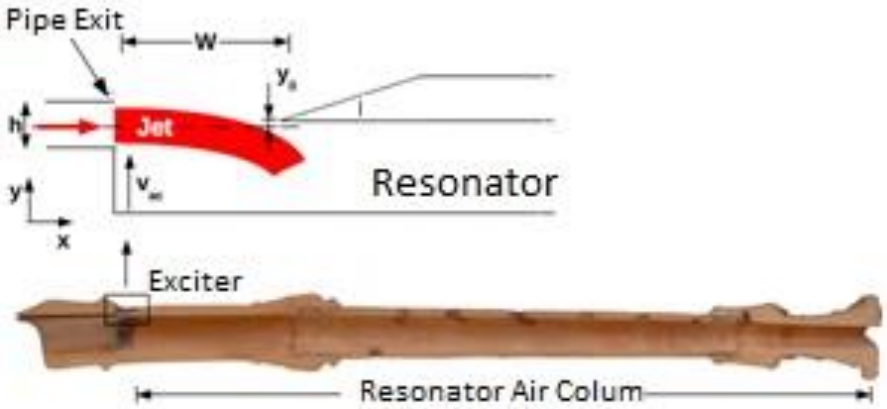

Figure 5 – Overall Flute System (see (Terrien, 2015))

Subsequent to the initial resonance frequency analysis, the modeling process advances to encompass the description of source mechanisms. This stage was pioneered by Helmholtz and Rayleigh. Helmholtz conceptualized the sources as flow sources or monopoles, while Rayleigh argued that due to their action at the open end of the bore, they should be characterized as dipoles (Rayleigh, 1984).

Interestingly, in the vicinity of the open end of the resonator, significant velocity fluctuations occur while the pressure fluctuations remain small. This observation led Helmholtz to revise his initial perspective, as reflected in the modified comments in the second version of his book. Surprisingly, a similar debate resurfaced in the 1960s between Elder Coltman and Fletcher, raising the same discussion. However, Coltman's pragmatic and astute approach, evident in his works, ultimately brought a definitive resolution to the debate (Coltman J. , 1968) (Elder, 1973).

In the early 1960s, Powell's research on the edge-tone phenomenon introduced a feedback loop model. The model considered various components as separate blocks that were subsequently interconnected. By analyzing the loop gain, the necessary phase and magnitude for sustained oscillations were determined, along with predictions for the conditions and frequency of oscillation in a linear model. However, for accurately predicting the amplitude of

the oscillations, a nonlinear model is required. Powell's approach has since served as inspiration for numerous descriptions based on loop systems in the field (Fletcher, 1979).

A significant phase in the advancement of flute models occurred with the research conducted by Mc Intyre *et al.*. They introduced a time simulation approach using simplified equations derived from physical models. Their models appeared elegant and promising, leading many researchers to believe that the essence of flute functioning had been captured within a physical model. However, it was eventually discovered that the model was more suitable for the violin and clarinet, as the published values did not result in oscillation for the flute. Fine-tuning the parameters and incorporating nonphysical elements, such as a DC blocking filter and white noise input, enabled the model to produce sound. Nonetheless, it became challenging to establish a direct relationship between the model's quantities and physical variables (McIntyre, 1983).

A more comprehensive approach, considering fluid mechanics and aero-acoustics, has been pursued by researchers such as Howe for the flute and Crighton and Elder for edge-tones. Simultaneously, a group based in Eindhoven, Netherlands, adopted an intermediate approach that drew inspiration from various researchers in the field. Their methodology strikes a balance between rigorous formulations and simplified descriptions, resulting in high-quality sound synthesis through models that incorporate lumped elements while incorporating a sufficient level of aero-acoustic considerations (Elder, 1973) (Howe, 1975).

Modern flute musical instruments are usually depicted from old versions of this instrument with some additions on the shape, size, and other effects. Although the normal old versions of flutes are more likely preferred by musicians, modern flutes are being used numerically with the help of embedded systems and computers adding new features to the way of playing and to the quality of sound (Heller, 2017). However, what is no doubt with is that playing a typical old musical flute naturally will produce the perfect sound associated with feelings and that what numerical flutes are not able to do so far.

The flute, as shown in the Figure 6, is mainly composed from three main parts: the exciter which contains the mouth piece and the whistle (exciter), the resonator that contains the holes, and the horn which act as a reflector of the output waves.

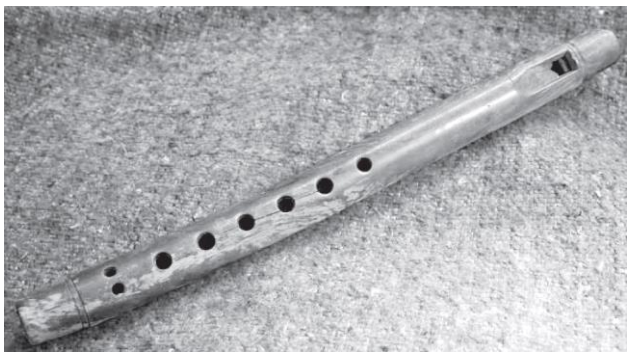

Figure 6 – Traditional flute musical instrument

Figure 7 shows a block diagram representation of this musical instrument. The system is composed from the musician's ear that serves as a sensor to form the loop and to act accordingly on the flow delivered by its mouth towards the flute exciter. The radiation at the output of this system is generated at the flute horn level.

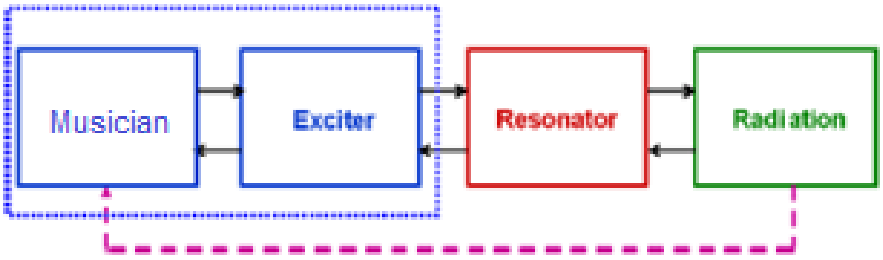

Figure 7 – Artificial loop based on the ear of the musician

Flutes are generally made from plastic, steel, or bamboo. Each type of material has a different effect on the quality of sound produced. This is due to the different types of materials used and to the visco-thermal effect of each material.

There are several types of flutes some are named according to the culture it is being used in (Chinese, Western, Indian, Irish, etc.), and others according to its shape and style (modern D, classical C, modern B, classical D, etc.). Every type has its own number of holes and their sizes and its own different shape and thus a different number of notes. For example, classical C flute has 6 holes and due to its shape, it can offer 8 notes. As for the classical D flute, it has the same number of holes (6 holes) but with only 6 notes because the D foot is smaller than the C foot; same number of holes, but different shape and size, give different number of notes. Classical flared flute has a larger number of holes (8 holes) and thus can offer more notes (23 notes) whereas baroque flute has 7 holes (less than classical flared flute) but yet can provide more notes due to its shape and size (32 notes to be precise). Figure 8 shows an illustration of these three types of flutes.

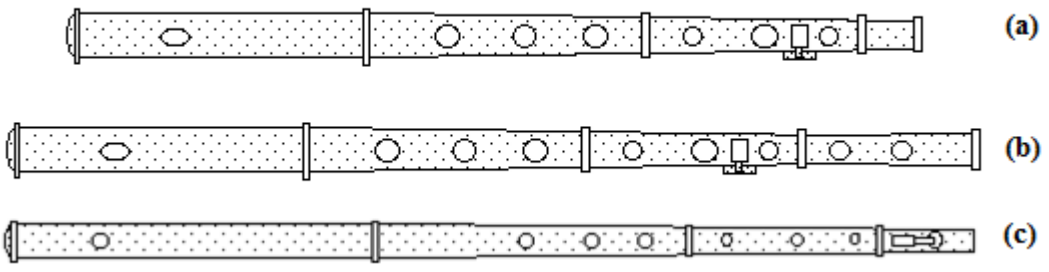

Figure 8 – Types of flutes: (a) Class D, (b) Classical Flared and (c) Baroque

3 – Sound Formation in Flutes

When a musician blows into the instrument, the pressure inside their mouth creates a flow within the channel (Terrien, 2015). This channel can either be a part of the instrument itself (as seen in Figure 5 – case of recorders) or formed by the musician's lips, as in the case of flutes. As the flow exits the channel, the viscosity of the air causes it to detach from the boundaries of the flute, resulting in the formation of an air jet. This jet is inherently unstable, and any disturbances it encounters will be amplified over time.

In the case of flutes, the jet generated at the exit of the channel remains confined within the window region until it encounters the bevel. The interaction between the jet and the bevel leads to a hydrodynamic feedback effect, which is a key mechanism responsible for the production of distinct bevel sounds. This phenomenon plays a significant role in shaping the acoustic characteristics of the flute (Powell, 1961) (Coltman J. , 1976). While the phenomenon of hydrodynamic feedback may become negligible once the steady state of the instrument is reached, it still plays a crucial role in the initial oscillation of the jet. The interaction between the jet and the bevel introduces the first disturbances to the jet, initiating its oscillation. As a result of the inherent instability of the air jet, these disturbances naturally amplify along the jet's path from the channel exit to the bevel, leading to oscillations on both sides of the bevel. This mechanism contributes to the sustained oscillation of the jet and influences the overall sound production of the flute (Verge M. , 1995)

As a result of the jet oscillation, flow alternately enters and exits the instrument, serving as the aero-acoustic source of pressure that supplies energy to the resonator (Chaigne & Kergomard, 2008). This pressure variation generates acoustic waves within the resonator, which propagate and primarily reflect at the first open hole. The superposition of outward and reflected waves forms a standing wave system within the resonator, disrupting the jet back to the level of the channel exit. This closure of the self-oscillation loop sustains the oscillation of the jet and, consequently, the sound production mechanism. The initial disturbance within the jet, amplified and maintained from the channel exit to the bevel, is instrumental in upholding the oscillatory behavior of the jet and the overall process of sound production.

In contrast to percussion, struck or plucked string instruments, the instruments within the flute family, along with reed instruments, bowed strings, and brass instruments, belong to the category of self-oscillating instruments. This classification arises from their ability to generate oscillations, specifically acoustic waves, from a continuous energy source supplied by the musician, or from slowly varying acoustic variables. The self-oscillation mechanism is inherently tied to the non-linear nature of these instruments. In musical acoustics, a common approach involves representing the instrument, as depicted in Figure 9, as a nonlinear excitation system coupled with a passive linear resonant system (McIntyre, 1983) (Rayleigh, 1984).

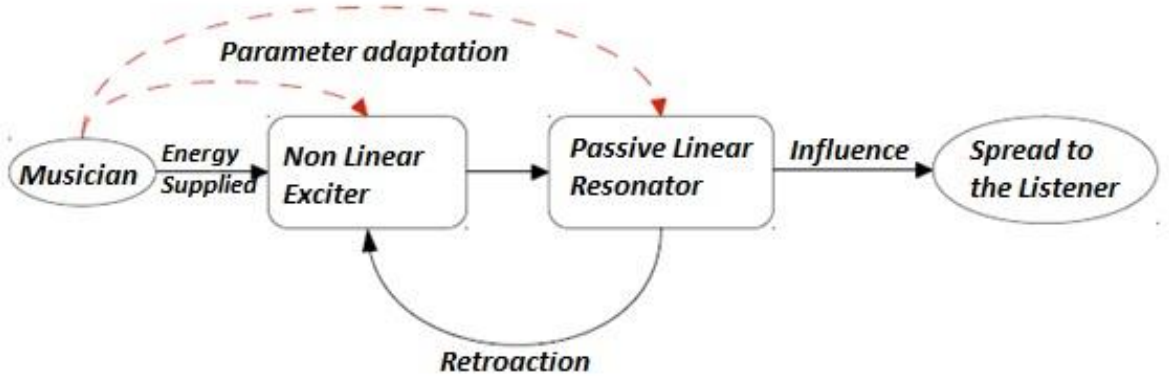

Figure 9 – Block diagram of the mechanism of sound production in auto-oscillatory musical instruments (Terrien, 2015)

3.1 – Acoustic Resonator of Wind Instruments

The resonator depicted in Figure 9 represents a passive linear resonator, extensively studied for centuries (Terrien, 2015). Due to its linear nature, it is relatively easier to describe, although some approximations may be required. In wind instruments like the flute, the resonator comprises the air column within the instrument's body, delimited by the instrument's hole or opening, which defines the geometric shape of the resonator.

The geometric characteristics of the air column, including conditions at the ends, size and position of note holes, and variations in bore section, play a significant role in governing the propagation of acoustic waves within the resonator. These characteristics directly influence the resonator's response to the provided excitation.

As shown in Figure 5, which provides an overview of the key components of a recorder, a substantial portion of flute family instruments possess two open ends, distinguishing them from most other wind instruments.

3.2 – Flute Exciter

While the propagation phenomena within the resonator continue to raise numerous questions, the characteristics of the exciter and its interaction with the resonator, which serves as its energy source, present an even greater complexity due to their non-linear nature.

Flutes possess a distinctive feature in terms of the exciter, as it involves the vibration of a solid body, unlike other wind instruments where reed blades or the instrumentalist's lips are involved. In the case of flutes, the excitation mechanism arises from the oscillation of an inherently unstable air jet around a bevel, as depicted in Figure 5.

In flutes, the self-oscillation mechanism relies on the synchronization between the oscillating jet and the acoustic waves. Similar to how one must continuously impart energy to a swing to maintain its oscillations, the jet-bevel system must excite the resonator periodically or at multiples of this periodicity within the sound field. This synchronization ensures the sustained oscillation of the jet and the generation of the desired sound.

3.3 – Closed-loop system

The generic modeling of self-oscillating instruments, represented by the looped system in Figure 9 (Terrien, 2015), can have specific applications tailored to the instruments within the flute family. Figure 10 illustrates a diagram highlighting the key physical phenomena incorporated in the state-of-the-art model for this particular family of instruments (Terrien, 2015).

This model takes into account the unique characteristics and mechanisms involved in flute instruments, encompassing the excitation of the resonator, propagation of acoustic waves, and the interaction between the jet and the bevel. By capturing these essential elements, the model provides a comprehensive representation of the flute family instruments' behavior and sound production.

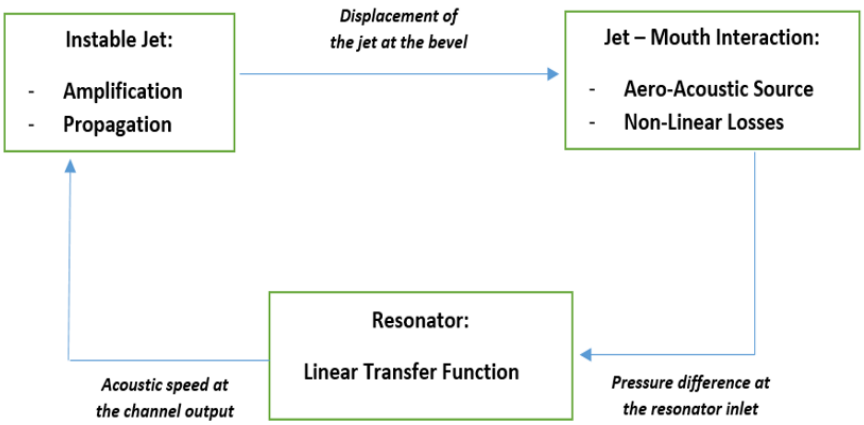

Figure 10 – Closed-Loop system of the self-oscillation mechanism of flute family instruments (Terrien, 2015)

4 – Literature Review

The production of a musical note by an instrument involves an intricate interplay between the instrument itself and the musician playing it (Terrien, 2011). Achieving the desired sound requires the instrumentalist to continuously adjust and adapt various parameters available to them. However, from an experimental standpoint, it can be challenging to expect a musician to precisely control and set all of these parameters simultaneously.

In fact, the system as shown in Figure 10 depends on two main entities, the musician and the flute instrument. As the ear and the musical experience of the musician plays a major role in controlling the air flow blowing in the exciter of the flute, the objective of this work will be to model all the parts of the system and then find some physical equivalence in order to be able to get the required frequency output precisely based on a closed loop control system.

Many researchers have been interested in the field of wind musical instruments (Mignot R. , 2009) (Lefebvre, 2011). They have studied this field from many perspectives. Some tried to model wind instruments mathematically as will be demonstrated in the coming discussions, others tried to control the blowing part, and few went deeply in discussing the visco-thermal losses and their effects on the musical output.

The work of Mignot dealt with the physical modelling of cylindrical acoustic tubes for digital simulation in real-time. The main application is the sound synthesis of wind instruments, with a realistic model, a modular method and a low-cost digital implementation. The acoustic model of "Webster-Lokshin", used in this work, is a unidimensional model which takes into account the "curvature" of the profile and the visco-thermal losses at the wall. With this acoustic model, a framework for simulation which is compatible with the "Waveguides" approach was obtained: a tube is then represented by a system with delays and closed loops, involving several sub-systems without internal delay (Mignot R. , 2009). Figure 11 shows a representation of the flute using the tools that Mignot has developed.

Digital waveguide synthesis models are computational physical models for certain classes of musical instruments (string, winds, brasses, etc.) which are made up of delay lines, digital filters, and often nonlinear elements. Digital waveguide models typically share the following characteristics:

- Sampled acoustic traveling waves;
- Follow geometry and physical properties of a desired acoustic system;
- Efficient for nearly lossless distributed wave media (strings, tubes, rods, membranes, plates, vocal tract);
- Losses and dispersion are consolidated at sparse points along each waveguide (Smith, 2006).

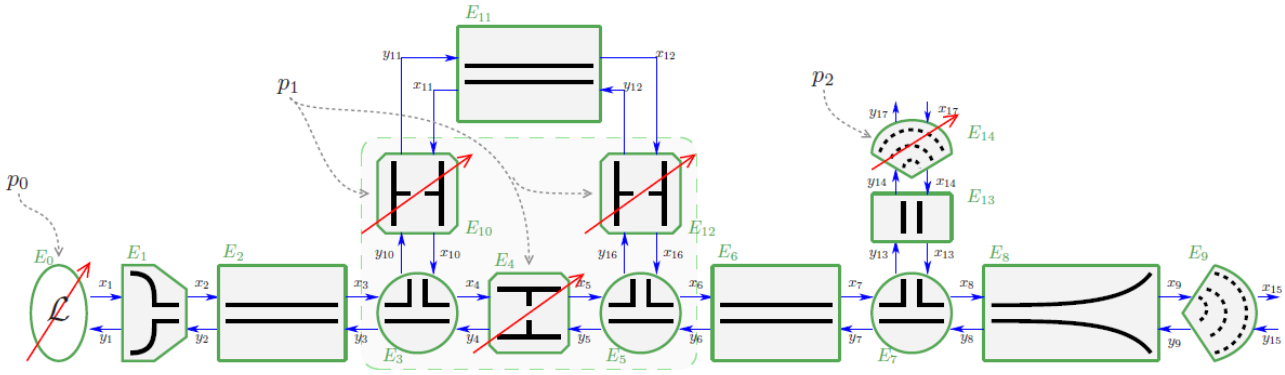

Figure 11 – Example of the musical wind instrument array

The structure shown in Figure 11 disregards the effects of sections (representing the coupling between two adjacent blocks), slopes at each extremity of the section, curvature and loss, and isolates wave propagators through the tube. Thus, it does not pretend to replace them, but allows to extend these models to a higher degree of refinement, considering the curvature and visco-thermal losses of the tube. Finally, the number of sections is imposed by the sampling frequency.

Another work presented a number of methods for the computational analysis of woodwind instruments which is the Transmission-Matrix Method (TMM) for the calculation of the input impedance. The latter is an approach based on the Finite Element Method (FEM) and it is applied to the determination of the transmission-matrix parameters of woodwind instrument tone holes, from which new formulas are developed that extend the range of validity of current theories. This approach is applied as well to tone holes on a conical bore, and, as a result, the tone hole transmission matrix parameters developed on a cylindrical bore are equally valid for use on a conical bore. A boundary condition for the approximation of the boundary layer losses for use with the FEM was developed, and it enables the simulation of complete woodwind instruments. The comparison of the simulations of instruments with many open or closed tone holes with calculations using the TMM reveal discrepancies that are most likely attributable to internal or external tone hole interactions. The maximal error is found to be smaller than 10 cents (Musical intervals are often expressed in cents, a unit of pitch based upon the equal tempered octave such that one tempered semitone is equal to 100 cents) (Lefebvre, 2011). Figure 12 shows an example of the different musical notes with their corresponding frequencies and the active holes that produces them.

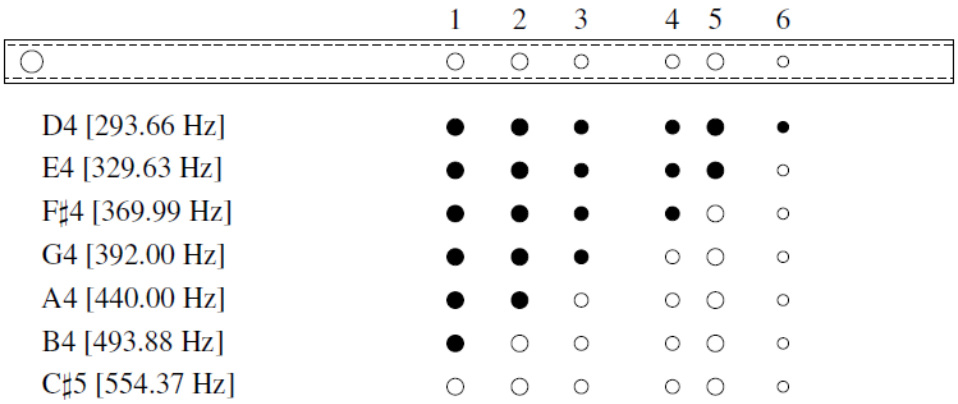

Figure 12 – Diagram of Keefe's flute

Furthermore, initial investigations using an artificial mouth specifically designed for the recorder have revealed previously unknown phenomena associated with this instrument (Terrien, 2011). These discoveries have sparked numerous inquiries and opened up new avenues of exploration to better understand the recorder and its intricate mechanisms.

First phenomenon: In certain fingerings, it has been observed that sounds can be detected at lower feed pressures than those typically used, sometimes even below the threshold for oscillation of the intended note. These oscillation phenomena resemble the "Aeolian sounds" observed in specific organ pipes or cross-sections, which manifest at very low supply pressures. While these sounds are sometimes musically utilized during organ decay or cross-blending, their presence in recorders has only recently been brought to light, and their distinctions from the "conventional" oscillation systems are not yet well understood. Further investigation is needed to elucidate these differences.

Second phenomenon: Indeed, there appears to be a significant diversity of behaviors, particularly concerning changes in pitch, depending on the specific fingering employed in the recorder. For certain fingerings, a bifurcation towards a higher note can be observed. From this new note, a subsequent bifurcation towards the original note occurs, gradually diminishing in strength. When conducting similar experiments with alternative fingerings, such as the B flat fingering, a transition to a quasi-periodic system can be perceived audibly, resulting in a rolling note effect. These observations underscore the intricate and varied dynamics at play in recorder playing, which contribute to the instrument's rich tonal palette (Terrien S. , 2011).

Added to that, Matignon classified the wind instrument into three main blocks which are the cup, pipe, bell, and radiation as shown in Figure 13. This design was represented in the form of blocks of delay lines which allowed each block to be modelled as a separate waveguide element, thus allowed to a more advanced sound synthesis technique (Matignon D. , 2014).

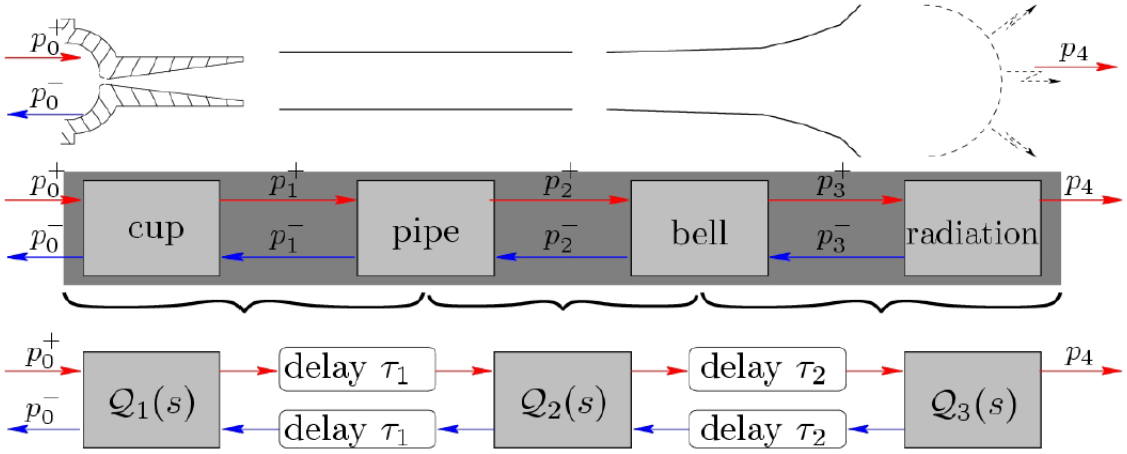

Figure 13 – Trumpet-like instrument- Decomposition into elementary subsystems

The musical instruments of the brass family are intricate physical systems that involve various phenomena, including the mechanics of deformable solids (such as muscles and tissues), fluid dynamics (jet and turbulence), and acoustic propagation (Lopes, 2016). From a dynamic systems perspective, they can be characterized as self-oscillating, nonlinear, and chaotic systems. Mastering the control of these instruments requires extensive training and expertise from musicians. Due to their complexity, the modeling, analysis, simulation, and control of brass instruments are active research areas. One approach involves the use of an artificial mouth coupled to an acoustic system, as depicted in Figure 14, to conduct calibrated and reproducible experiments. At IRCAM (Institut de Recherche et Coordination Acoustique/Musique), the robotic design of an artificial mouth specifically designed for brass instruments has been initiated. This work aims to develop models and simulations for the mouth system (including the lips and the instrument), while also creating a robotic version for studying control strategies. The "Hamiltonian formulation with ports" is a suitable approach for modeling complex physical systems, as it ensures well-balanced energy transfer and preserves passivity. Thus, this work encompasses the fields of musical acoustics, robotics, and control, bringing together expertise from these disciplines (Lopes, 2016).

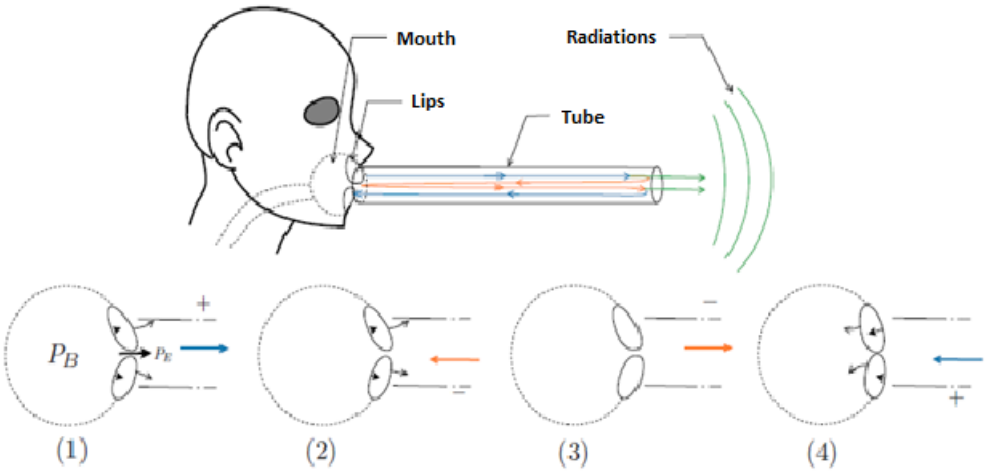

Figure 14 – Diagram of copper type instrument operation coupled to the musician (first resonance)

Current modeling of the flute family instruments allows a good prediction of their operation in transient and steady state. They allow to interpret a large part of the phenomena observed when the control parameters of the instrument vary slowly with respect to the time response of the instrument. The musician, however, constantly varies these parameters to articulate the musical discourse. During sudden spikes in particular, an instant variation in the supply pressure induce a gradual oscillation of the instrument. The birth of sound plays an important role in the perception of sound, the control of these sudden spikes is therefore an essential point in learning the concept of making flute instruments. The works presented focus on the study of sudden transients in flute instruments. The study is restricted to instruments whose jet geometry is fixed by the manufacturer.

At the end of this section, we have to mention the recent work presenting a comprehensive study of visco-thermal effects in quasi-2D artificial structures which are designed to exhibit double-negative behavior using a digital waveguide approach. The building units consist of structured cylinders made of a rigid material having air cavities penetrating deeply into the waveguide. The reported experimental characterization of these types of metamaterials is unable to demonstrate any features confirming double-negative effects. Extensive numerical simulations based on the boundary-element method were treated, which has been improved and adapted to tackle visco-thermal losses in these metamaterial structures. These structures are very efficient in absorbing the energy of acoustic waves traveling through them. For frequencies within the first passband, the absorbed energy reaches values as high as 80% of the amount of absorbance being directly proportional to the reciprocal of the group velocity in the band. The visco-thermal losses, which are enhanced due to the extremely low value of the group velocity inside this narrow-band region, in addition to the possibility of reducing the relevance of losses by applying a scaling factor to the dimensions of the initial samples were treated. So, the study lead to the conclusion that final based metamaterial structures are not able to exhibit the predicted double-negative behavior because of the strong dissipation

associated with visco-thermal losses. A large amount of losses has also been reported in other rigid-based structures with embedded resonances, where the lack of a significant signal in the transmitted energy made them unfeasible for developing practical devices. These results may indicate that visco-thermal losses are relevant to any rigid-based double negative metamaterials. The rigid-based metamaterial structures could become interesting alternatives to conventional absorbers in particular situations, e.g., when treating low frequencies or when the excitation is narrow banded, such as damped and low-frequency resonances in room acoustics (Henríquez & Chocano, 2017).

Chapter 1- Study of Viscothermal Losses Within the Resonator of a Wind Musical Instrument

1.1 – Introduction

Historically, the first efficient and inexpensive simulations introduced for simple models (conservative plane waves) were based on signal processing tools: the so-called digital waveguide formalism (Tassart, 1999) (Helie T. , 2003) (Helie, Mignot, & Matignon, 2011) and more specifically, a factored form introduced by Kelly-Lochbaum (Matignon, Mignot, & Helie, 2007). The initial idea rested on the factoring of the alembertian of the equation of plane waves into two transport operators who each govern decoupled "round trip" progressive waves, from which we could derive a form in efficient delay system for the simulation (Mignot R. , 2009) (Helie T. , 2006).

Furthermore, 3D and 2D models with realistic boundary conditions are far too complex to be considered, especially in real-time sound synthesis. They can be effectively reduced to a 1D wave equation including a term that models the tube profile. It is about the *equation of the pavilions* also called model of Webster. A more elaborated version of this conservative model includes the effect of visco-thermal losses due to the boundary layers in the vicinity of the walls. This dissipative model, known as *de Webster-Lokshin 1D* (Lokshin & Rok, 1978) (Haddar, Hélie, & Matignon, 2003) (Haddar & Matignon, 2008), includes a term which involves a fractional derivation in time of order 3/2. This operator plays a crucial role from a perceptual point of view on sound realiazation (Vigué, Vergez, Lombard, & Cochelin, 2019).

The objective of this chapter is, first, to establish a ***knowledge model*** from partial differential equations which define the Webster-Lokshin model of an acoustic tube of constant radius *r*. Thus, a conventional resolution in the operational field leads to the analytical expression of the acoustic impedance and admittance of the tube as a function of the position *x*, its length *L* and its radius *r*. This working methodology will be similar to the one used for the modelling of the diffusive phenomenon in a semi-infinite homogeneous tube already proposed in previous works (Assaf, 2015). Then, a system vision is proposed aiming to causally decompose the whole model into sub-models in order to facilitate the analysis in the frequency domain. In addition, the introduction of uncertainty at the fractional order level makes it possible to study its influence on visco-thermal losses. Finally, for the time domain simulation in Chapters 2 and 4, two rational forms composed of an integrator and *N* second-order cells, one in cascade and the other in parallel, are introduced in as a ***role model***. The parametric values of the cascaded rational form are then determined using the ***Frequency Domain System Identification*** (FDSI) module of the CRONE Toolbox, with the frequency response of the

knowledge model as target. As for the parametric values of the parallel form, they are obtained by the decomposition of the cascade form into simple elements.

1.2 – Modelling

1.2.1 – System Definition

Consider an acoustic tube of length L and constant radius r subjected to an acoustic flow (also called volume flow) $Q_v(t)$ with $x = 0$ where $x \in [0\,;L]$ (Figure 1.1).

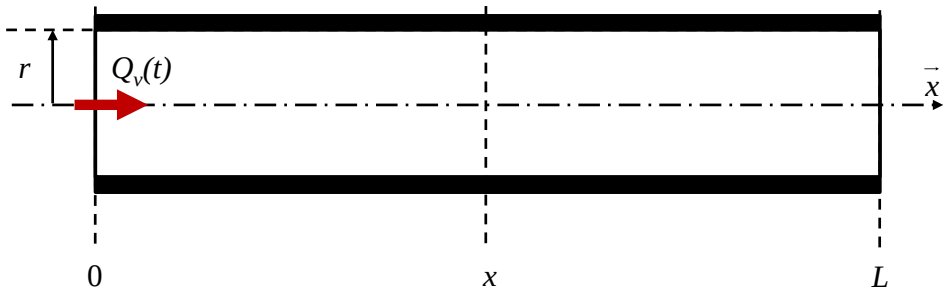

Figure 1.1 – One-dimensional description of an acoustic tube of radius r = constant and of finite length L subjected to an acoustic flow $Q_v(t)$ with $x = 0$

When an acoustic wave propagates in the air, this sets the particles of the fluid in motion which vibrate at a speed $v(t)$ around their equilibrium position. The acoustic flow $Q_v(t)$ then measures the flow [in m^3/s] of this speed through a surface and present it as a scalar quantity (Blanc, 2009) (Ducasse E. , 1990) (Ségoufin C. , 2000) (Ducasse E. , 2001) (Terrien., 2014).

The acoustic impedance $\boldsymbol{Z_{ac}}$ (also called *specific* acoustic impedance, because it is an intensive quantity) of a medium is defined in steady state by the ratio between the acoustic pressure [in Pa] and the speed [in m/s] of the associated particle. When the medium is air, $\boldsymbol{Z_{ac}}$ is equal to the product between the density of air, ρ_a, and the speed of sound in air, c_a, thus $\boldsymbol{Z_{ac}} = \rho_a\, c_a$. These two parameters depend also on the air temperature T_a. For more illustration, Table 1.1 gives the values of the speed of the sound c_a, the density ρ_a and the characteristic acoustic impedance Z_{ac} as a function of the temperature T_a of the air.

Table 1.1 – Values of the speed of sound c_a, the density ρ_a and the characteristic acoustic impedance Z_{ac} as a function of the air temperature T_a

$\boldsymbol{T_a}$ (°C)	-10	-5	0	5	10	15	20	25	30
$\boldsymbol{c_a}$ (m/s)	325.4	328.5	331.5	334.5	337.5	340.5	343.4	346.3	349.2
$\boldsymbol{\rho_a}$ (kg/m^3)	1.341	1.316	1.293	1.269	1.247	1.225	1.204	1.184	1.164
$\boldsymbol{Z_{ac}}$ (Pa s/m)	436.5	432.4	428.3	424.5	420.7	417	413.5	410	406.6

The model used in this work is that of Webster-Lokshin (Haddar, Hélie, & Matignon, 2003). It is a model with mono-spatial dependence which characterizes the linear propagation of acoustic waves in tubes with axial symmetry. This model takes also into account visco-thermal losses at the wall boundaries with the assumption of wide tubes (Mignot R. , 2009).

Thus, in an axisymmetric tube of constant section $S = \pi r^2$, the acoustic pressure $P(x,t,L)$ and the acoustic flow $Q_v(x,t,L)$ are governed by the *equation of the pavilions*, also called Webster-Lokshin, and Euler equation, leading to system (1.1):

$$\begin{cases} \dfrac{r}{c_a}\dfrac{\partial^2}{\partial t^2}P(x,t,L) + 2\varepsilon\dfrac{r}{c_a}\dfrac{\partial^{3/2}}{\partial t^{3/2}}P(x,t,L) - r\dfrac{\partial^2}{\partial x^2}P(x,t,L) = 0\ ,\ \ x\in[0\,;L]\ ,\ \ t>0 \\ \dfrac{\rho_a}{S}\dfrac{\partial}{\partial t}Q_v(x,t,L) + \dfrac{\partial}{\partial x}P(x,t,L) = 0 \end{cases} , \qquad (1.1)$$

where ε is a parameter associated with visco-thermal losses. More precisely, ε is given by the relation:

$$\varepsilon = \frac{K_0}{r}\ , \quad \text{with} \quad K_0 = \sqrt{l_v} + (\gamma - 1)\sqrt{l_h}\ , \qquad (1.2)$$

where l_v and l_h represent the characteristic lengths of viscous ($l_v = 4 \times 10^{-8}$ m) and thermal ($l_h = 6 \times 10^{-8}$ m) effects, γ being the ratio of specific heats.

The phenomenon of visco-thermal losses is a dissipative effect at the wall of the tube, which is due to the viscosity of the air and to the thermal conduction (Mignot R. , 2009) (Boutin, Le Conte, Le Carrou , & Fabre, 2018). For the case of wind musical instruments resonators, the assumption of wide tubes is used. This hypothesis is expressed by the following relation:

$$r \gg \max\,[\, r_v = (l_v\,\lambda)^{0.5};\ r_h = (l_h\,\lambda)^{0.5}], \qquad (1.3)$$

where $\lambda = c_a/f$ represents the wavelength (in m) and f the frequency (in Hz).

Thus, for a speed of the sound c_a and a frequency f_{min} corresponding to the lower limit of the frequency domain of study of the model, it is possible to determine the minimum value of the radius r_{min} of the acoustic tube below which the model is not valid.

As an illustration where $l_v = 4 \times 10^{-8}$ m, $l_h = 6 \times 10^{-8}$ m and $c_a = 346.3$ m/s (at a constant temperature $T_a = 25°C$), Figure 1.2 presents the curves of $r_v(f) = (l_v\, c_a/f)^{0.5}$ (in red) and $r_h(f) = (l_h\, c_a/f)^{0.5}$ (in blue) with respect to the frequency f.

If we consider that the frequency domain of study of the Webster-Lokshin model is that of the frequencies audible by the human ear, frequencies ranging between 20 Hz (most serious frequency) and 20 000 Hz (most acute frequency), then $f_{min} = 20$ Hz. For this value of f_{min}, the model is valid for acoustic tube radius greater than 1 mm (in next section, entitled ***1.2.3 - Frequency Response Analysis***, $r = 5$ mm).

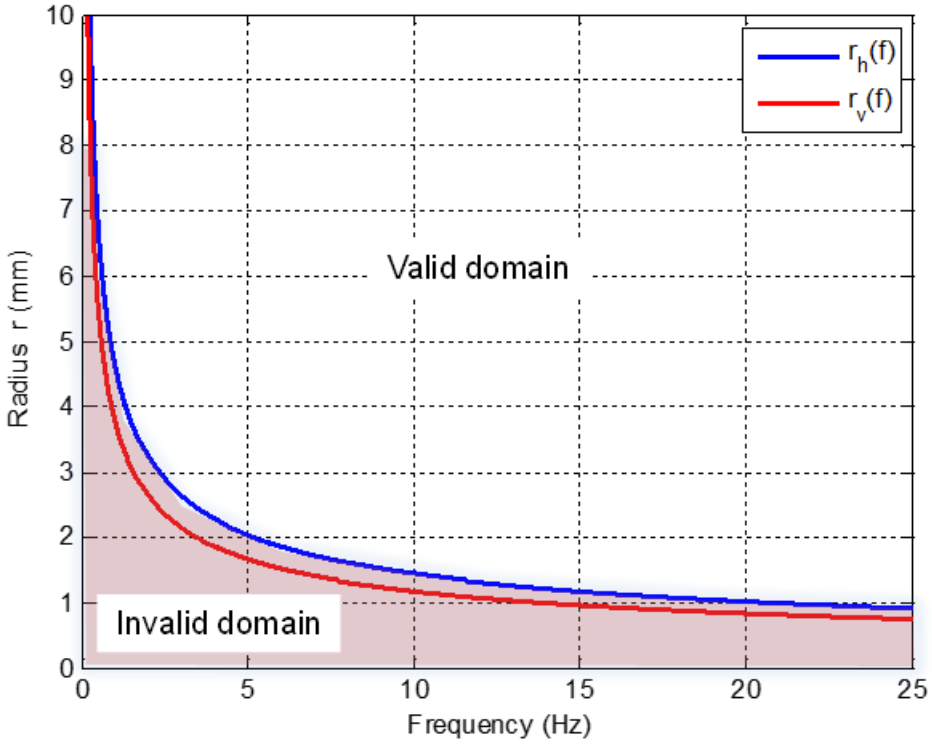

Figure 1.2 – Curves $r_v(f) = (l_v\, c_a/f)^{0.5}$ (in red) and $r_h(f) = (l_h\, c_a/f)^{0.5}$ (in blue) with respect to the frequency f

1.2.2 Resolution in the Symbolic Domain

Under the assumption of zero initial conditions, the Laplace transformation applied to the system (1.1) leads to:

$$\begin{cases} \left[\left(\left(\frac{s}{c_a}\right)^2 + 2\varepsilon\left(\frac{s}{c_a}\right)^{3/2}\right) - \frac{\partial^2}{\partial x^2}\right] r\,\overline{P}(x,s,L) = 0 \\ \frac{\rho_a}{S}\, s\,\overline{Q}_v(x,s,L) + \frac{\partial}{\partial x}\overline{P}(x,s,L) = 0 \end{cases}, \tag{1.4}$$

with $\overline{P}(x,s,L) = \mathrm{TL}\{P(x,t,L)\}$ and $\overline{Q}_v(x,s,L) = \mathrm{TL}\{Q_v(x,t,L)\}$, s being the Laplace variable and TL its transformation.

Solving the Webster-Lokshin equation (Haddar, Hélie, & Matignon, 2003) gives the solution $\overline{P}(x,s,L)$ in the general form:

$$\overline{P}(x,s,L) = \frac{A(s)}{r}\, e^{x\,\Gamma(s)} + \frac{B(s)}{r}\, e^{-x\,\Gamma(s)}, \tag{1.5}$$

where *A(s)* and *B(s)* are rational functions of *s* which depend on the boundary conditions, and $\Gamma(j\omega) = j\,k(\omega)$, $k(\omega)$ being a standard complex wave number. $\Gamma(s)$ is given in the Laplace domain by (Mignot, Hélie, Matignon, & ., 2011):

$$\Gamma(s) = \sqrt{\left(\frac{s}{c_a}\right)^2 + 2\varepsilon\left(\frac{s}{c_a}\right)^{3/2}}\ , \quad \text{with} \quad R_e\left(\Gamma(s)\right) \geq 0 \ \text{ if } \ \varepsilon \geq 0\ . \tag{1.6}$$

The expression of the solutions of $\overline{Q}_v(x,s,L)$ is deduced in two ways:

1- Using the Euler equation in the Laplace domain (second equation of the system (1.4)), that is:

$$\overline{Q}_v(x,s,L) = -\frac{S}{\rho_a}\frac{1}{s}\frac{\partial}{\partial x}\overline{P}(x,s,L), \tag{1.7}$$

2- By introducing the general solution of $\overline{P}(x,s,L)$ in relation (1.7), that is:

$$\overline{Q}_v(x,s,L) = -\frac{S}{\rho_a}\frac{1}{s}\frac{\partial}{\partial x}\left(\frac{A(s)}{r}\,\mathrm{e}^{x\,\Gamma(s)} + \frac{B(s)}{r}\,\mathrm{e}^{-x\,\Gamma(s)}\right). \tag{1.8}$$

Finally, the solution of $\overline{Q}_v(x,s,L)$ is expressed in relation (1.9):

$$\overline{Q}_v(x,s,L) = -\left(\frac{S}{\rho_a\, r}\right)\frac{1}{s}\Gamma(s)\,A(s)\,\mathrm{e}^{x\,\Gamma(s)} + \left(\frac{S}{\rho_a\, r}\right)\frac{1}{s}\Gamma(s)\,B(s)\,\mathrm{e}^{-x\,\Gamma(s)}. \tag{1.9}$$

Taking into account the boundary conditions makes it possible to determine the two unknowns *A(s)* and *B(s)*, and finally the impedance $Z(x,s,L) = \overline{P}(x,s,L)/\overline{Q}_v(x,s,L)$ of the finite medium of length *L*.

As an example, consider a zero impedance at *x = L*, that is *Z (L, s, L) = 0*, which leads to $\overline{P}(L,s,L) = 0$. According to relation (1.5), we obtain:

$$\frac{A(s)}{r}\,\mathrm{e}^{L\,\Gamma(s)} + \frac{B(s)}{r}\,\mathrm{e}^{-L\,\Gamma(s)} = 0\ , \tag{1.10}$$

from which we deduce that

$$B(s) = -A(s)\,\mathrm{e}^{2L\,\Gamma(s)}\ . \tag{1.11}$$

Then, replacing *B(s)* by its expression (1.11) in the relation (1.5) of $\overline{P}(x,s,L)$, it comes:

$$\overline{P}(x,s,L) = \frac{A(s)}{r}\,\mathrm{e}^{x\,\Gamma(s)}\left(1 - \mathrm{e}^{2(L-x)\,\Gamma(s)}\right)\ . \tag{1.12}$$

In the same way, by replacing *B(s)* by its expression (1.10) in the relation (1.8) of $\overline{Q}_v(x,s,L)$, we obtain:

$$\overline{Q}_v(x,s,L) = -\left(\frac{S}{\rho_a\, r}\right)\frac{1}{s}\Gamma(s)\,A(s)\,\mathrm{e}^{x\,\Gamma(s)}\left(1+\mathrm{e}^{2(L-x)\,\Gamma(s)}\right). \qquad (1.13)$$

Finally, the impedance $Z(x,s,L) = \overline{P}(x,s,L)/\overline{Q}_v(x,s,L)$ is given by the relationship of relations (1.11) and (1.12), that is:

$$Z(x,s,L) = -\frac{\dfrac{A(s)}{r}\,\mathrm{e}^{x\,\Gamma(s)}\left(1-\mathrm{e}^{2(L-x)\,\Gamma(s)}\right)}{\left(\dfrac{S}{\rho_a\, r}\right)\dfrac{1}{s}\Gamma(s)\,A(s)\,\mathrm{e}^{x\,\Gamma(s)}\left(1+\mathrm{e}^{2(L-x)\,\Gamma(s)}\right)}\ , \qquad (1.14)$$

which gives after simplification:

$$Z(x,s,L) = -\frac{\rho_a}{S}\,\frac{s}{\Gamma(s)}\left(\frac{1-\mathrm{e}^{2(L-x)\,\Gamma(s)}}{1+\mathrm{e}^{2(L-x)\,\Gamma(s)}}\right)\ , \qquad (1.15)$$

knowing that *tanh(y) = - (*$1 - e^{2y}$*)/(*$1 + e^{2y}$*), tanh(.)* being the tangent hyperbolic function,

$$Z(x,s,L) = \frac{\rho_a}{S}\,\frac{s}{\Gamma(s)}\,\tanh\left((L-x)\,\Gamma(s)\right)\ . \qquad (1.16)$$

From the perspective of a system approach, the function $\Gamma(s)$ defined by the relation (1.5) is rewritten by putting the term s/c_a into factor, that is:

$$\Gamma(s) = \left(\frac{s}{c_a}\right)\sqrt{1+2\varepsilon\left(\frac{c_a}{s}\right)^{1/2}}\ , \qquad (1.17)$$

or again, in canonical form,

$$\Gamma(s) = \left(\frac{s}{c_a}\right)\sqrt{\frac{1+\left(\dfrac{s}{\omega_{r,m}}\right)^{m}}{\left(\dfrac{s}{\omega_{r,m}}\right)^{m}}} \quad \text{with} \quad \begin{cases} m = 0.5 \\ \varepsilon = 2\,m\,\dfrac{K_0}{r} \\ \omega_{r,m} = (2\,\varepsilon)^{1/m}\,c_a \end{cases}\ , \qquad (1.18)$$

where $\omega_{r,m}$ is a transitional frequency (in rad/s). Note that in the theoretical case where the system is conservative, that is to say $\varepsilon = 0$, the function $\Gamma(s)$ (relation (1.17)) is reduced to $\Gamma(s) = s/c_a$. By replacing $\Gamma(s)$ of relation (1.18) in relation (1.14), $Z(x,s,L)$ can be expressed as follows:

$$Z(x,s,L)=\frac{\rho_a\, c_a}{S}\sqrt{\frac{\left(\frac{s}{\omega_{r,m}}\right)^m}{1+\left(\frac{s}{\omega_{r,m}}\right)^m}}\ \tanh\left((L-x)\left(\frac{s}{c_a}\right)\sqrt{\frac{1+\left(\frac{s}{\omega_{r,m}}\right)^m}{\left(\frac{s}{\omega_{r,m}}\right)^m}}\right)\ , \qquad (1.19)$$

or again, by introducing the characteristic acoustic impedance $Z_{ac} = \rho_a\, c_a$ and the transitional frequency $\omega_{Lx} = c_a/(L-x)$ (in rad/s),

$$Z(x,s,L)=\frac{Z_{ac}}{S}\sqrt{\frac{\left(\frac{s}{\omega_{r,m}}\right)^m}{1+\left(\frac{s}{\omega_{r,m}}\right)^m}}\ \tanh\left(\left(\frac{s}{\omega_{L,x}}\right)\sqrt{\frac{1+\left(\frac{s}{\omega_{r,m}}\right)^m}{\left(\frac{s}{\omega_{r,m}}\right)^m}}\right)\ . \qquad (1.20)$$

Thus, from the analytical expression of the impedance *Z(x,s,L)* (1.20), knowing the flow $\overline{Q_v}(x,s,L)$ at any point *x* of the acoustic tube of length *L* makes it possible to deduce the pressure $\overline{P}(x,s,L)$ (Hélie, Gandolfi, & Hezard, 2014).

■ ***Remarks***

At ***x = L****, $1/\omega_{Lx} = 0$ hence, knowing that tanh(0) = 0, we verify that* $Z(L,s,L)=0$.

At ***x = 0****, the input impedance* $Z_{in}(s,L)=Z(0,s,L)$ *of the finite medium of length L is given by:*

$$Z_{in}(s,L)=\frac{\rho_a}{S}\ \frac{s}{\Gamma(s)}\ \ tanh\left(L\ \ \Gamma(s)\right)\ . \qquad (1.21)$$

Always at ***x = 0****, but for a semi-infinite medium ($L\to\infty$), knowing that* $\lim_{y\to\infty}\tanh(y)=1$ *the input impedance* $Z_{in}(s,\infty)=Z(0,s,\infty)$ *becomes:*

$$Z_{in}(s,\infty)=\lim_{L\to\infty}Z(x=0,s,L)=\frac{\rho_a}{S}\frac{s}{\Gamma(s)}\ . \qquad (1.22)$$

Finally, in the theoretical case of a purely ***conservative*** *system ($\varepsilon = 0$) the acoustic impedance Z(x, s, L), noted in this case $Z_0(x, s, L)$, of a* ***finite*** *medium is reduced to*

$$Z_0(x,s,L)=\frac{Z_{ac}}{S}\ \tanh\left(\frac{s}{\omega_{Lx}}\right)\ , \qquad (1.23)$$

and that of a semi-infinite medium, denoted $Z_0(x,s,\infty)$, at

$$Z_0(x,s,\infty)=\lim_{L\to\infty}Z(x,s,L)=\frac{Z_{ac}}{S}=cst\ . \qquad (1.24)$$

Note that the conservative case, although purely theoretical, allows by comparison to better observe the effect of visco-thermal losses. ■

To conclude this paragraph concerning the resolution in the symbolic domain, the study of asymptotic behaviors of *Z(x,s,L)*, that is

$$\lim_{s\to 0} Z(x,s,L) = \frac{Z_{ac}}{S}\frac{1}{\omega_{r,m}^{m}}\frac{1}{\omega_{L,x}} \quad \lim_{s\to 0} s^{m+1} \tag{1.25}$$

and

$$\lim_{s\to \infty} Z(x,s,L) \to \frac{Z_{ac}}{S} = cst \quad , \tag{1.26}$$

highlights that *Z(x,s,L)* tends towards a behavior of the following types:

- ***fractional derivative*** of order *m+1*, *i.e.* 1.5 with *m = 0.5*, when ***s tends to zero***;

- ***proportional***, whose gain value is fixed by Z_{ac}/S, when ***s tends to infinity***.

1.2.3 - Frequency Response Analysis

In stationary harmonic system, the frequency response *Z(x,jω,L)* is given by:

$$Z(x,j\omega,L) = \frac{Z_{ac}}{S}\sqrt{\frac{\left(\frac{j\omega}{\omega_{r,m}}\right)^{m}}{1+\left(\frac{j\omega}{\omega_{r,m}}\right)^{m}}}\ \tanh\left(\left(\frac{j\omega}{\omega_{L,x}}\right)\sqrt{\frac{1+\left(\frac{j\omega}{\omega_{r,m}}\right)^{m}}{\left(\frac{j\omega}{\omega_{r,m}}\right)^{m}}}\right) \quad , \tag{1.27}$$

where the transitional frequencies $\omega_{r,m}$ and $\omega_{L,x}$ have the following expressions:

$$\begin{cases} \omega_{r,m} = \dfrac{c_a}{\left(r/4mK_0\right)^{1/m}} \\ \omega_{L,x} = \dfrac{c_a}{L-x} \end{cases} \quad . \tag{1.28}$$

Thus, showing that $\omega_{r,m}$ decreases when the radius *r* increases and that, on the contrary, $\omega_{L,x}$ increases when the position *x* considered moves away from the origin and approaches the end of the acoustic tube, *L*.

For illustration, and in order to plot the frequency response *Z(x,jω,L)* in stationary harmonic system, let us consider an acoustic tube whose nominal dimensions are as follows:

- radius $r = 5 \times 10^{-3}$ m (value perfectly in accordance with the domain of validity of the Webster-Lokshin model);

- length $L = 0.3$ *m;*
- temperature of 25°C;
- density ρ_a = 1.184 kg/m^3 and a speed of sound in the air c_a = 346.3 m/s (refer to Table 1.1).

Note that these values of r and L representing the resonator of a recorder lead to the values of the transitional frequencies $\omega_{r,m}$ = 4.92 rad/s (0.78 Hz) and $\omega_{L,x}$ = 1154 rad/s (184 Hz) with x = 0, thus showing for such an instrument that $\omega_{r,m} << \omega_{L,x}$.

Figure 1.3 presents in $x = 0$ the Bode diagrams of $Z(0,j\omega,L)$ on the range [20; 20,000] Hz of the audible frequencies by the human ear (Figure 1.3.a) and on the range [20; 4000] Hz of the frequencies attainable with a recorder (Figure 1.3.b).

Although an in-depth analysis of the frequency response of the model is developed in the following paragraph, the observation of these diagrams over the range of audible frequencies leads to a remark which concerns the existence of two very distinct behaviors:

- The first on the frequency range [20; $\omega_{L,x}/2\pi = 184$] Hz with a derivative behavior of order 1, highlighting the absence of the fractional behavior on this frequency range which exists for frequencies lower than $\omega_{r,m}/2\pi = 0.78$ Hz ;
- The second on the frequency range [$\omega_{L,x}/2\pi = 184$; 20 000] Hz with an alternation of resonances and anti-resonances.

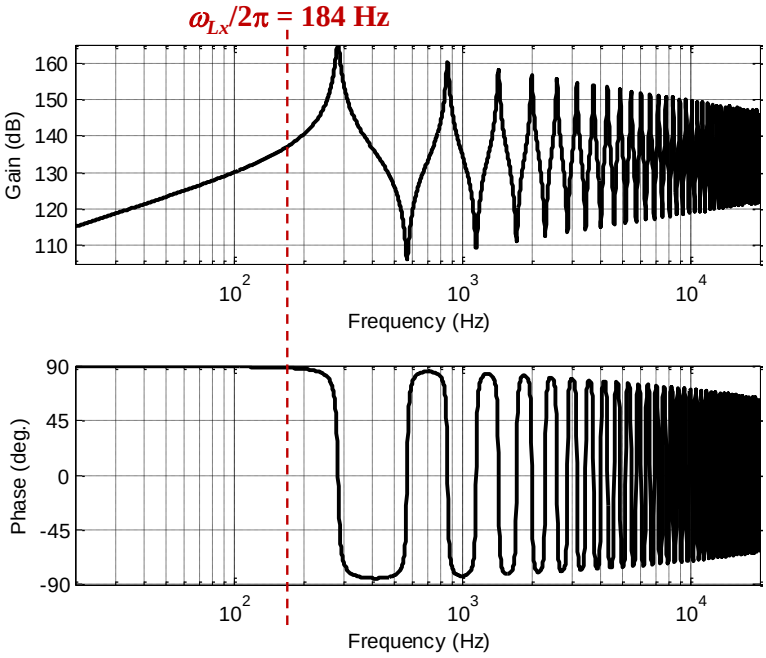

(a)

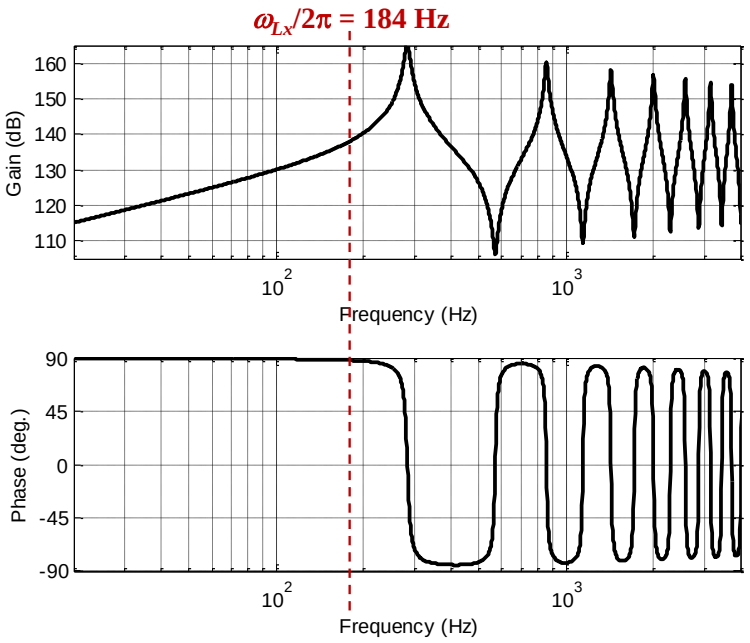

(b)

Figure 1.3 – Bode Diagrams of $Z(0,j\omega,L)$ on the range [20 ; 20 000] Hz of the frequencies audible by the human ear (a) and on the range [20 ; 4 000] Hz of frequencies attainable with a recorder (b)

1.3 - System Approach

As a reminder, the resonator is only a part of our simulator which includes a non-linear exciter (Chapter 2), an artificial mouth (Chapter 3), and the simulation of the whole system (Chapter 4).

From a causal point of view, the input of the resonator at $x = 0$ is defined by the pressure at the output of the nonlinear exciter. This is the reason why the system approach developed in this paragraph considers the admittance $Y(x,s,L) = Z^{-1}(x,s,L)$ and not the impedance $Z(x,s,L)$. More specifically, it is the input admittance at $x = 0$, denoted $Y_{in}(s,L) = Y(0,s,L)$. Note that this consideration of the admittance $Y_{in}(j\omega,L)$ leads to an integrative behavior for frequencies lower than $\omega_{L,x}$ (derivative for $Z(x,s,L)$), thus respecting integral causality, a fundamental notion in a system approach.

In addition, the global admittance $Y(x,s,L)$ is broken down into a cascade of local transfer functions of which all the parameters, as well as all the input and output variables will have a physical meaning. This decomposition then facilitates the frequency analysis of the Webster-Lokshin model, thus reaching a reduced model to be implemented in the simulator.

1.3.1 Decomposition of Admittance $Y(x, s, L)$ into Subsystems

The admittance $Y(x,s,L) = Z^{-1}(x,s,L)$ of an acoustic tube of length L at a point x between 0 and L is therefore defined by the expression:

$$Y(x,s,L) = \frac{\overline{Q}_v(x,s,L)}{\overline{P}(x,s,L)} = \frac{S}{Z_{ac}} \sqrt{\frac{1+\left(\frac{s}{\omega_{r,m}}\right)^m}{\left(\frac{s}{\omega_{r,m}}\right)^m}} \; \frac{1}{\tanh\left(\left(\frac{s}{\omega_{L,x}}\right)\sqrt{\frac{1+\left(\frac{s}{\omega_{r,m}}\right)^m}{\left(\frac{s}{\omega_{r,m}}\right)^m}}\right)} \quad , \quad (1.29)$$

relation that can be expressed as follows,

$$Y(x,s,L) = H_0 \; I_m(s) \; T(x,s,L) \quad , \quad (1.30)$$

by taking

$$H_0 = \frac{S}{Z_{ac}} = \frac{S}{\rho_a \, c_a} \quad , \quad (1.31)$$

$$I_m(s) = \sqrt{\frac{1+\left(\frac{s}{\omega_{r,m}}\right)^m}{\left(\frac{s}{\omega_{r,m}}\right)^m}} \quad , \tag{1.32}$$

and

$$T(x,s,L) = \frac{1}{\tanh(F(x,s,L))} \quad , \tag{1.33}$$

where

$$F(x,s,L) = \left(\frac{s}{\omega_{L,x}}\right) \; I_m(s) \quad . \tag{1.34}$$

For the following, the concept of ***acoustic admittance*** $Y(x,s,L) = \overline{Q}_v(x,s,L) / \overline{P}(x,s,L)$ is replaced by the concept of ***transfer function*** $H(x,s,L)$ defined between the pressure source $\overline{P}_{in}(s) = \overline{P}(x=0,s)$ at the input of the tube at *x = 0* and the flow $\overline{Q}_v(x,s,L)$ at any point *x* of the tube of length *L* (middle finite) and of constant radius *r*, that is:

$$H(x,s,L) = \frac{\overline{Q}_v(x,s,L)}{\overline{P}_{in}(s)} = H_0 \; I_m(s) \; T(x,s,L). \tag{1.35}$$

At *x = 0*, for this finite medium, the admittance of input $Y_{in}(s,L)$ has the expression:

$$Y_{in}(s,L) = H(0,s,L) = \frac{\overline{Q}_v(0,s,L)}{\overline{P}_{in}(s)} = H_0 \; I_m(s) \; T(0,s,L). \tag{1.36}$$

At *x* = 0, but for a semi-infinite medium ($L \to \infty$), the admittance of input $Y_{in}(s,\infty)$ is reduced to:

$$Y_{in}(s,\infty) = H(0,s,\infty) = \frac{\overline{Q}_v(0,s,\infty)}{\overline{P}_{in}(s)} = H_0 \; I_m(s). \tag{1.37}$$

Figure 1.4 presents the block diagrams associated with this system approach where the different transfer functions are defined by:

$$\begin{cases} H_0 = \dfrac{\bar{Q}_{in}(s)}{\bar{P}_{in}(s)} = \dfrac{S}{Z_{ac}} = cst \\ I_m(s) = \dfrac{\bar{Q}_v(0,s,\infty)}{\bar{Q}_{in}(s)} = \sqrt{\dfrac{1+\left(\dfrac{s}{\omega_{r,m}}\right)^m}{\left(\dfrac{s}{\omega_{r,m}}\right)^m}} \\ T(x,s,L) = \dfrac{\bar{Q}_v(x,s,L)}{\bar{Q}_v(0,s,\infty)} = \dfrac{1}{\tanh\left(\left(\dfrac{s}{\omega_{L,x}}\right) I_m(s)\right)} \end{cases} . \qquad (1.38)$$

Note that the quantity $H_0\ \bar{P}_{in}(s)$ is homogeneous at a flow, noted $\bar{Q}_{in}(s)$, corresponding to the conversion of the pressure source applied at *x=0* (Dirichlet condition) into an equivalent source of flow always applied at *x=0* (Neumann condition) (Assaf, 2015).

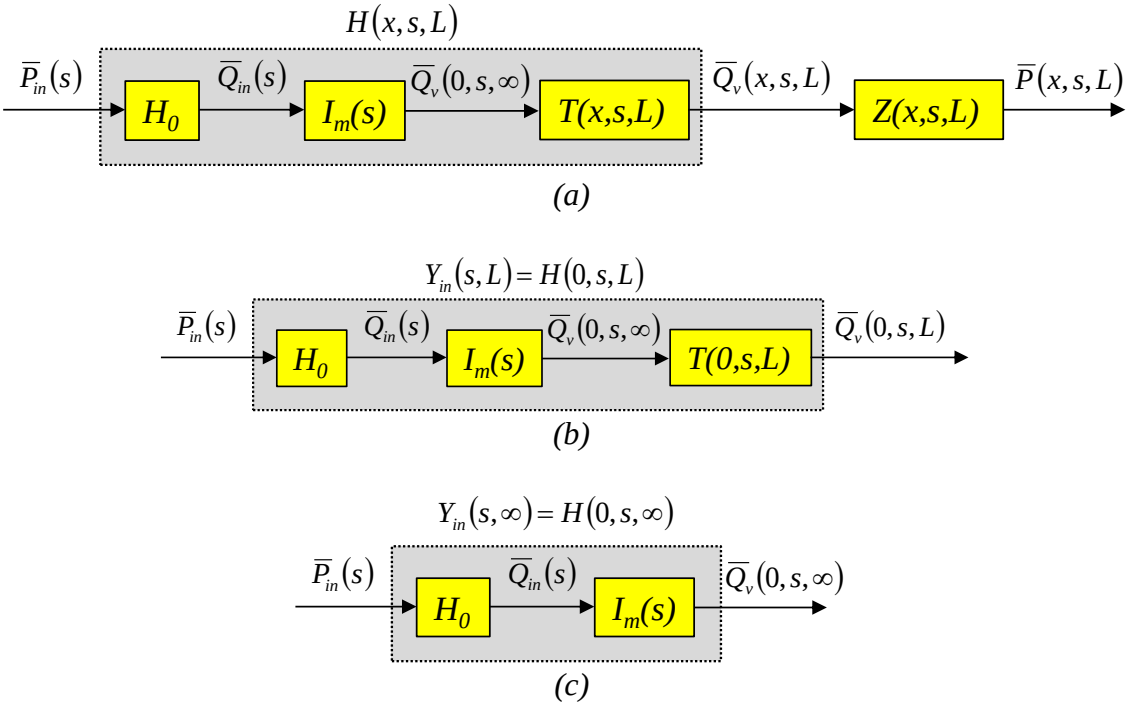

Figure 1.4 – Block diagrams associated with the system approach: Whatever *x* is between 0 an *L* (a), at *x*=0 for the finite system *L* (b), at *x*=0 for a semi finite system (c)

1.3.2 - Analysis in the Frequency Domain

In stationary harmonic system, the relation (1.35) becomes:

$$H(x, j\omega, L) = \frac{\bar{Q}_v(x, j\omega, L)}{\bar{P}_{in}(j\omega)} = H_0\ I_m(j\omega)\ T(x, j\omega, L)\ , \qquad (1.39)$$

with

$$I_m(j\omega) = \frac{\overline{Q}_v(0, j\omega, \infty)}{\overline{Q}_{in}(j\omega)} = \sqrt{\frac{1 + \left(j\frac{\omega}{\omega_{r,m}} \right)^m}{\left(j\frac{\omega}{\omega_{r,m}} \right)^m}} \tag{1.40}$$

and

$$T(x, j\omega, L) = \frac{\overline{Q}_v(x, j\omega, L)}{\overline{Q}_v(0, j\omega, \infty)} = \frac{1}{\tanh\left(F(x, j\omega, L)\right)} \quad , \tag{1.41}$$

where

$$F(x, j\omega, L) = \left(\frac{j\omega}{\omega_{L,x}} \right) \; I_m(j\omega) \quad . \tag{1.42}$$

The remaining part of this paragraph is dedicated to a detailed analysis of the frequency responses $I_m(j\omega)$, $F(x,j\omega,L)$ and $T(x,j\omega,L)$ of each subsystem, then of the frequency response $H(x,j\omega,L)$ of the overall system.

1.3.2.1 - Analysis of $I_m(j\omega)$

The analysis of $I_m\ (j\omega)$ highlights two behaviors whose transition zone is fixed by the transitional frequency $\omega_{r,m}$, these behaviors are:

- for $\omega << \omega_{r,m}$, a fractional integrative behavior of order $m/2 = 0.25$,

$$\forall\ \omega << \omega_{r,m}\ , \quad I_m(j\omega) = \sqrt{\frac{1 + \left(j\frac{\omega}{\omega_{r,m}} \right)^m}{\left(j\frac{\omega}{\omega_{r,m}} \right)^m}} \underset{\omega << \omega_{r,m}}{\approx} \left(\frac{\omega_{r,m}}{j\omega} \right)^{m/2} \quad \Rightarrow \quad \begin{cases} |I_m(j\omega)| = \left(\frac{\omega_{r,m}}{\omega} \right)^{m/2} \\ \arg I_m(j\omega) = -m\frac{\pi}{4} \end{cases} ; \tag{1.43}$$

- for $\omega >> \omega_{r,m}$, unit proportional behavior,

$$\forall\ \omega >> \omega_{r,m}\ , \quad I_m(j\omega) = \sqrt{\frac{1 + \left(j\frac{\omega}{\omega_{r,m}} \right)^m}{\left(j\frac{\omega}{\omega_{r,m}} \right)^m}} \underset{\omega << \omega_{r,m}}{\approx} 1 \quad \Rightarrow \quad \begin{cases} |I_m(j\omega)| = 1 \\ \arg I_m(j\omega) = 0 \end{cases} . \tag{1.44}$$

As an illustration, let us take the acoustic tube whose nominal dimensions are fixed by a radius $r = 5 \times 10^{-3}$ m and a length $L = 0.3$ m at a temperature of 25 °C, with $\rho_a = 1.184$ kg/m^3 and $c_a = 346.3$ m/s. In this case, and as a reminder, the numerical value of the transitional frequency $\omega_{r,m}$ (relation (1.28)) and 4.92 rad/s (0.784 Hz).

Figure 1.5 presents the Bode diagrams of the frequency response $I_m(j\omega)$ over the range $[10^{-4}; 10^4]$ Hz. The two behaviors appear clearly:

- for $\omega << \omega_{r,m}$, a gain diagram with a straight line with slope $p = -m/2*20$ dB/dec = -5 dB/dec and a phase diagram with a horizontal line at $-m/2*90° = -22.5°$;
- for $\omega >> \omega_{r,m}$, a gain diagram with a horizontal line at 0 dB and a phase diagram with a horizontal line at 0°.

Figure 1.6 presents the same frequency response of $I_m(j\omega)$ but only on the range [20; 20,000] Hz of the frequencies audible by the human ear, and this with a gain diagram in linear-linear scale and a phase diagram with the frequency axis also in linear scale. The observation of this answer makes it possible to affirm, for this representative example of a recorder, that the unit proportional behavior is dominant, that is:

$$\forall \quad \omega \geq 2\pi\, 20 \text{ rad/s}, \quad I_m(j\omega) = \frac{\overline{Q}_v(0, j\omega, \infty)}{\overline{Q}_{in}(j\omega)} \approx 1 \quad . \tag{1.45}$$

Thus, for the area of study considered in this work, area defined by the range [20; 20,000] Hz of the audible frequencies, the transfer $I_m(s)$ can be reduced to the unit which leads to $\overline{Q}_v(0, s, \infty) = \overline{Q}_{in}(s)$, leading to a reduction in the block diagrams of Figure 1.4.

The direct consequence is that in the case of a semi-infinite medium at $x = 0$ (Figure 1.4.c), the fractional integrative behavior has no influence on the range of audible frequencies.

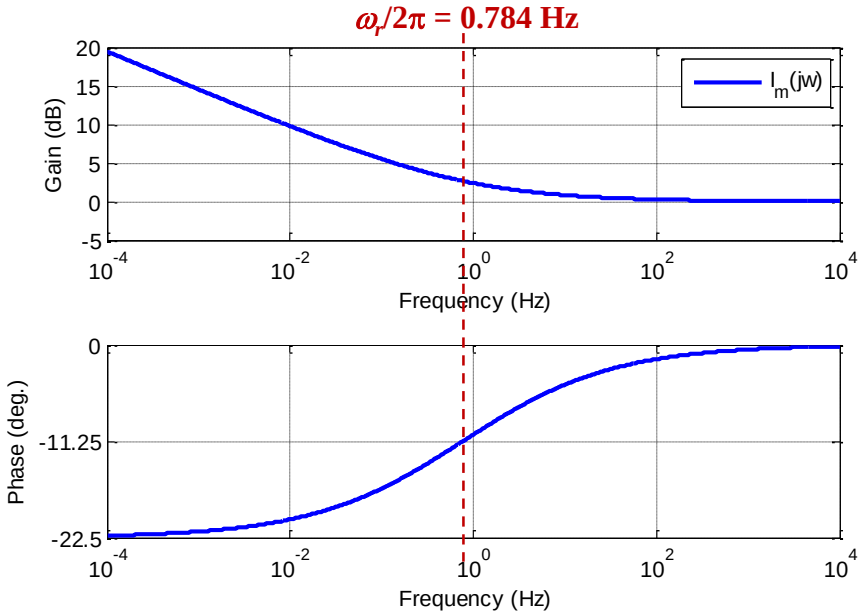

Figure 1.5 – Bode diagrams of $I_m(j\omega)$ on the range $[10^{-4}; 10^4]$ Hz

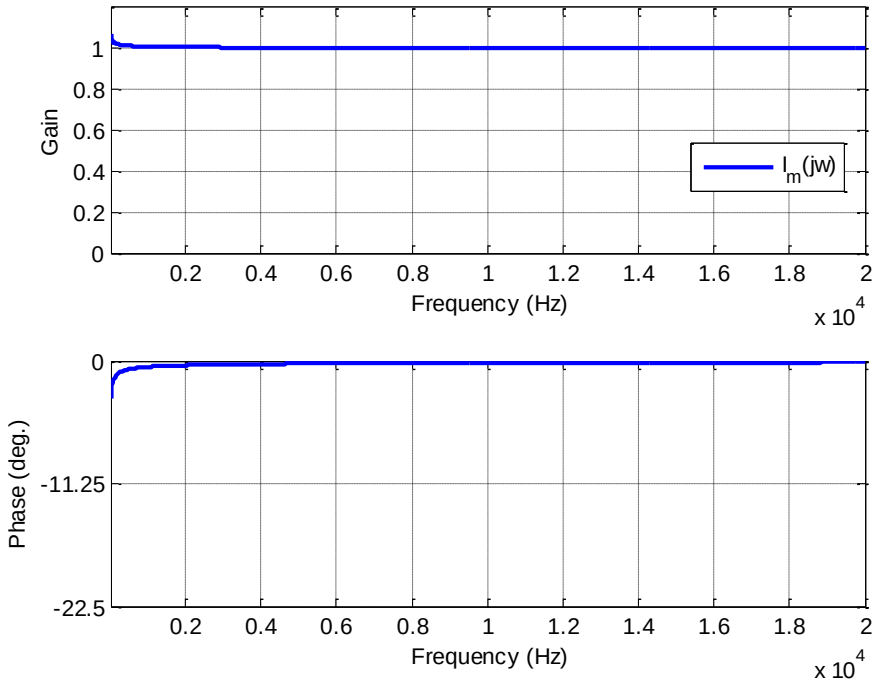

Figure 1.6 – Frequency response of $I_m(j\omega)$ on the range [20; 20,000] Hz of the audible frequencies

1.3.2.2 - Analysis of F(0,jω,L)

Knowing that in the case of a recorder $\omega_{r,m} << \omega_{L,x}$, the analysis of $F(0,j\omega,L)$ again highlights two behaviors whose transition zone is fixed by the transitional frequency $\omega_{r,m}$, that is:

- for $\omega << \omega_{r,m}$, a ***fractional derivative*** behavior of order (1- *m/2*) = 0.75,

$$\forall\, \omega << \omega_{r,m}\ , \quad F(x, j\omega, L) = \left(\frac{j\omega}{\omega_{L,x}}\right)\sqrt{\frac{1+\left(j\dfrac{\omega}{\omega_{r,m}}\right)^{m}}{\left(j\dfrac{\omega}{\omega_{r,m}}\right)^{m}}} \underset{\omega << \omega_{r,m}}{\approx} \left(\frac{\omega_{r,m}^{m/2}}{\omega_{L,x}}\right)(j\omega)^{(1-m/2)} \quad , \quad (1.46)$$

hence the module and the argument are defined as follows:

$$\begin{cases} \left|F(x, j\omega, L)\right| = \left(\dfrac{\omega_{r,m}^{m/2}}{\omega_{L,x}}\right)\omega^{(1-m/2)} \\ \arg F(x, j\omega, L) = \left(1-\dfrac{m}{2}\right)\dfrac{\pi}{2} \end{cases} ; \qquad (1.47)$$

- for $\omega_r << \omega$, a ***derivative*** behavior of order 1,

$$\forall\ \omega_{r,m} << \omega\ ,\quad F(x,j\omega,L)=\left(\frac{j\omega}{\omega_{L,x}}\right)\sqrt{\frac{1+\left(j\frac{\omega}{\omega_{r,m}}\right)^{m}}{\left(j\frac{\omega}{\omega_{r,m}}\right)^{m}}}\underset{\omega_{r,m}<<\omega}{\approx}\left(\frac{j\omega}{\omega_{L,x}}\right)\Rightarrow\begin{cases}\left|F(x,j\omega,L)\right|=\dfrac{\omega}{\omega_{L,x}}\\ \arg F(x,j\omega,L)=\dfrac{\pi}{2}\end{cases}\quad .(1.48)$$

Figure 1.7 presents at $x = 0$ the Bode diagrams of the frequency response $F(0,j\omega,L)$ on the range $[10^{-4}\ ;\ 10^{4}]$ Hz. The two behaviors appear clearly:

- for $\omega << \omega_{r,m}$, a gain diagram with a straight line with $p_1 = (1-m/2)*20$ dB/dec = 15 dB/dec and a phase diagram with a horizontal line at $(1-m/2)*90° = 67.5°$;
- for $\omega >> \omega_{r,m}$, a gain diagram with a straight line with slope $p_2 = 20$ dB/dec of this a phase diagram with a horizontal straight line at 90 °.

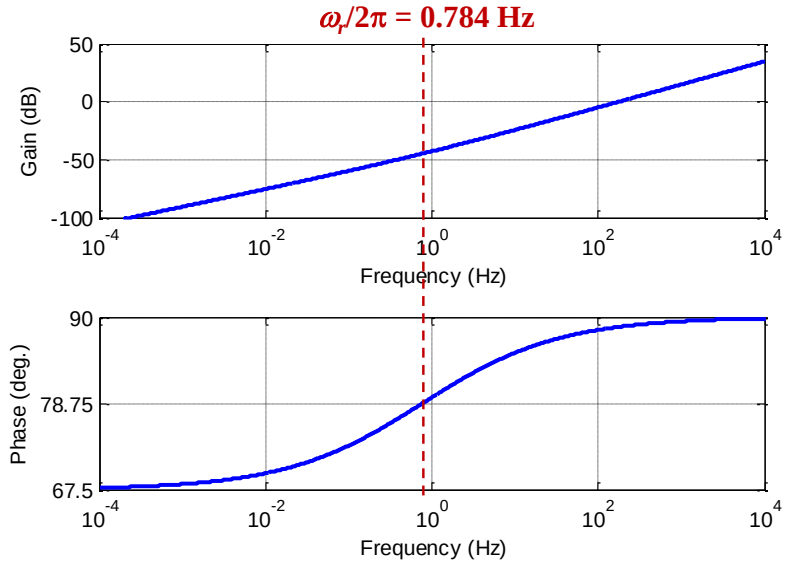

Figure 1.7 – Bode diagrams of $F(0, j\omega,L)$ on the range $[10^{-4}; 10^{4}]$ Hz

1.3.2.3 - Analysis of T(0,jω,L)

The analysis of $T(x,j\omega,L)$ highlights three behaviors whose transition zones are fixed by the transitional frequencies $\omega_{r,m}$ and ω_{Lx} :

- for $\omega << \omega_{Lx}$, an ***integrative behavior with two different orders*** according to the frequency range. Indeed,

$$\forall\ \omega << \omega_{L,x}\ ,\quad T(x,j\omega,L)=\frac{1}{\tanh\left(F(x,j\omega,L)\right)}\underset{\omega<<\omega_{L,x}}{\approx}\frac{1}{F(x,j\omega,L)}\ ,\qquad (1.49)$$

with, for $\omega << \omega_{r,m}$, an orderly ***fractional integrative*** behavior - $(1- m/2) = - 0.75$, that is

$$\forall\ \omega << \omega_{r,m}\ ,\quad \frac{1}{F(x,j\omega,L)} \underset{\omega << \omega_{r,m}}{\approx} \left(\frac{\omega_{L,x}}{\omega_r^{m/2}}\right)\frac{1}{(j\omega)^{(1-m/2)}} \Rightarrow \begin{cases} |T(x,j\omega,L)| = \left(\frac{\omega_{L,x}}{\omega_r^{m/2}}\right)\frac{1}{\omega^{(1-m/2)}} \\ \arg T(x,j\omega,L) = \left(1-\frac{m}{2}\right)\frac{\pi}{2} \end{cases} \quad (1.50)$$

and, for $\omega_{r,m} << \omega$, a ***derivative*** behavior of order 1, that is

$$\forall\ \omega_{r,m} << \omega\ ,\quad \frac{1}{F(x,j\omega,L)} \underset{\omega_{r,m} << \omega}{\approx} \left(\frac{\omega_{L,x}}{j\omega}\right) \Rightarrow \begin{cases} |T(x,j\omega,L)| = \frac{\omega_{L,x}}{\omega} \\ \arg T(x,j\omega,L) = -\frac{\pi}{2} \end{cases} ; \quad (1.51)$$

- for $\omega_{L,x} << \omega$, a behavior composed of an alternation of ***anti-resonances*** and ***resonances***, giving the expression of *T(x,jω,L)*,

$$\forall\ \omega_{L,x} << \omega\ ,\quad T(x,j\omega,L) = \frac{1}{\tanh\left(\left(\frac{j\omega}{\omega_{L,x}}\right)\sqrt{\frac{1+\left(j\frac{\omega}{\omega_{r,m}}\right)^m}{\left(j\frac{\omega}{\omega_{r,m}}\right)^m}}\right)}\ . \quad (1.52)$$

Figure 1.8 shows the Bode diagrams of $1/F(0,j\omega,L)$ (in red) and of $T(0,j\omega,L)$ (in blue) over the range $[10^{-4}\ ;\ 10^{4}]$ Hz (Figure 1.8.a) and on the range [20; 4000] Hz of the audible and achievable frequencies with a recorder (Figure 1.8.b).

Below the first cutoff frequency [10^{-4}; $\omega_{Lx}/2\pi = 184$] Hz, the responses of $1/F(0,j\omega,L)$ (in red) and $T(0,j\omega,L)$ (in blue) overlap where:

- a ***fractional integration behavior*** of order -0.75 over the range [10^{-4}; $\omega_r/2\pi = 0.784$] Hz is observed;

- an ***integrative behavior*** of order 1 over the range [$\omega_{r,m}/2\pi = 0.784$; $\omega_{Lx}/2\pi = 184$] Hz is observed.

Beyond 184 Hz, the frequency response $T(0,j\omega,L)$ (in blue) clearly presents an alternation of anti-resonances and resonances introduced by the hyperbolic tangent function.

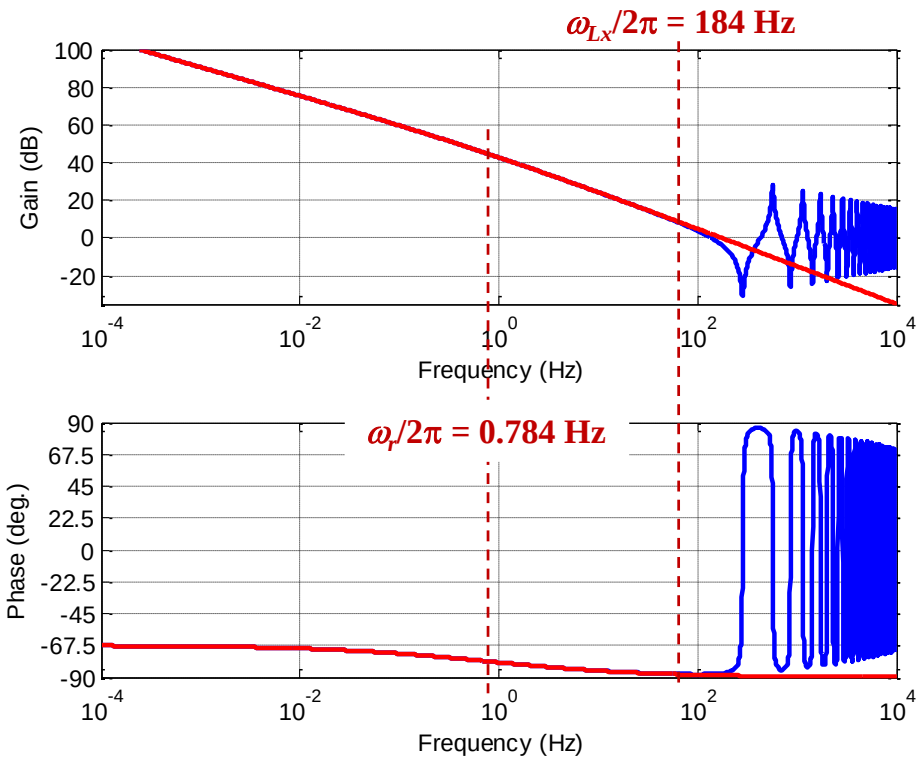

(a)

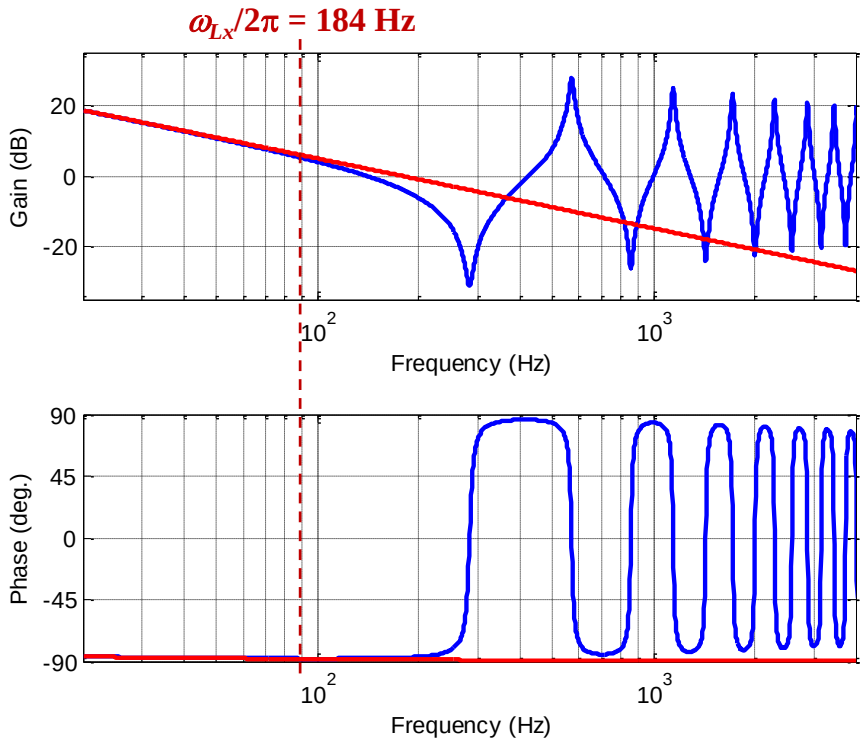

(b)

Figure 1.8 – Bode diagrams of 1/F(0,jω,L) (in red) and of *T(0,jω,L)* (in blue) on the range [10^{-4}; 10^{4}] Hz (a) and on the range [20; 4000] Hz of audible and achievable frequencies with a recorder (b)

1.3.2.4 - Analysis of H(x,jω,L)

The analysis of *H(x,jω,L)* highlights three behaviors whose transition zones are fixed by the transitional frequencies ω_r and ω_{Lx}:

- for $\omega << \omega_r << \omega_{Lx}$, an orderly ***fractional integrative behavior*** - (1- *m/2*) = - 0.75, that is

$$\forall\ \omega << \omega_{r,m}\ ,\quad H(x,j\omega,L) \underset{\omega << \omega_{r,m}}{\approx} \left(\frac{\omega_{L,x}}{\omega_{r,m}^{m/2}}\right)\frac{H_0}{(j\omega)^{(1-m/2)}} \Rightarrow \begin{cases} |H(x,j\omega,L)| = \left(\dfrac{\omega_{L,x}}{\omega_{r,m}^{m/2}}\right)\dfrac{H_0}{\omega^{(1-m/2)}} \\ \arg H(x,j\omega,L) = \left(1-\dfrac{m}{2}\right)\dfrac{\pi}{2} \end{cases} ;(1.53)$$

- for $\omega_{r,m} << \omega << \omega_{Lx}$, a ***derivative behavior*** of order 1, that is:

$$\forall\ \omega_{r,m} << \omega << \omega_{L,x},\quad H(x,j\omega,L) \underset{\omega_{r,m} << \omega << \omega_{L,x}}{\approx} H_0\left(\frac{\omega_{L,x}}{j\omega}\right) \Rightarrow \begin{cases} |H(x,j\omega,L)| = H_0\dfrac{\omega_{L,x}}{\omega} \\ \arg H(x,j\omega,L) = -\dfrac{\pi}{2} \end{cases} ;(1.54)$$

- for $\omega_{Lx} << \omega$, a behavior composed of an alternation of ***anti-resonances*** and ***resonances***, that is:

$$\forall\ \omega_{L,x} << \omega\ ,\quad H(x,j\omega,L) \underset{\omega_{L,x} << \omega}{\approx} \frac{H_0}{\tanh\left(\left(\dfrac{j\omega}{\omega_{L,x}}\right)\sqrt{\dfrac{1+\left(j\dfrac{\omega}{\omega_{r,m}}\right)^m}{\left(j\dfrac{\omega}{\omega_{r,m}}\right)^m}}\right)}\ . \qquad (1.55)$$

Figure 1.9 presents at $x = 0$ ($\omega_{Lx}/2\pi$ = 184 Hz), in $x = L/2$ ($\omega_{Lx}/2\pi$ = 368 Hz) and at $x = 3L/4$ ($\omega_{Lx}/2\pi$ = 735 Hz) the Bode diagrams of *H(0,jω,L)* (in black), of *H(L/2,jω,L)* (in blue) and of *H(3L/4,jω,L)* (in red) on the range [20; 4000] Hz of the audible and achievable frequencies with a recorder.

Over the range [20; $\omega_{Lx}/2\pi$] Hz, the three responses of *H(x,jω,L)* present an integration behavior of order 1. The fractional integration behavior of order -0.75 does not appear over this range as it is present within a much lower frequency (0.784 Hz). Beyond ω_{Lx}, the three responses present a succession of alternation of anti-resonances and resonances introduced by the hyperbolic tangent (*tanh*) function. In the journal (Abou Haidar, Moreau, & Abi Zeid Daou, 2021), the authors show that the influence of the order *m* is essentially located:

- for ***gain diagrams***, at the peaks of resonances and anti-resonances, quantifiable effects using quality factors for anti-resonances and for resonances illustrating well the phenomenon of dissipation associated with visco-thermal losses;
- for ***phase diagrams***, at the crossing points at 0° with a local slope which is important as the order is small where the slope becomes infinite for *m = 0* (purely conservative case).

Moreover, note that the farther the position x moves away from the origin, the higher the transitional frequency ω_{Lx} pushes the anti-resonance and resonance frequencies towards the high frequencies.

In addition, the position x has no influence on the transitional frequency $\omega_{r,m}$, the fractional integrative behavior of order -0.75 still does not appear on this frequency range.

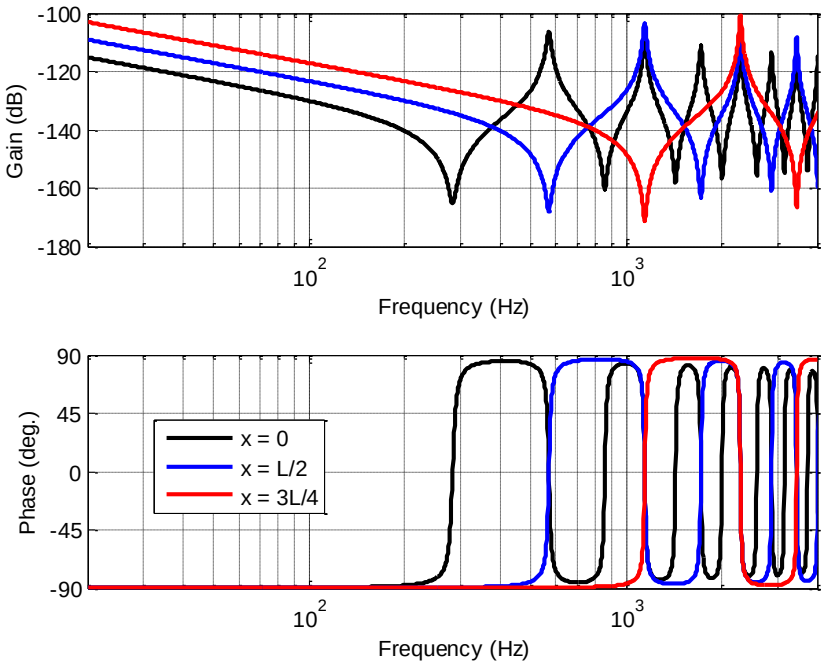

Figure 1.9 – Bode diagrams in $x = 0$ ($\omega_{Lx}/2\pi$ = 184 Hz), in $x = L/2$ ($\omega_{Lx}/2\pi$ = 368 Hz) and in $x = 3L/4$ ($\omega_{Lx}/2\pi$ = 735 Hz) of $x = 3L/4$ ($\omega_{Lx}/2\pi$ = 735 Hz) (in black), of $H(L/2,j\omega,L)$ (in blue) and of $H(3L/4,j\omega,L)$ (in red) in the range [20; 4000] Hz of audible and achievable frequencies

1.3.3 - Study of the Influence of the Fractional Order *m*

In the Webster-Lokshin model, the fractional order m has the value 0.5. The objective of this paragraph and the rest of this chapter is to analyze the influence of the order m on the behavior of the resonator by considering that m belongs to the interval [0; 1] with a nominal value m_0 = 0.5, a consideration which facilitates the introduction of the concept of parametric uncertainty (additive or multiplicative) at the fractional order level. Thus, by generalizing the expression of the parameter $\varepsilon = K_0/r$ (relation (1.2)) associated with visco-thermal losses in the Webster-Lokshin model at $\varepsilon = 2\ m\ K_0/r$ (relation (1.18) which for m = 0.5 gives the same expression), the analytical link is naturally established between visco-thermal losses and fractional order.

Thus, the fractional order occurs only in the presence of visco-thermal losses. In the theoretical case of a purely ***conservative*** system, the parameter ε is zero which is equivalent to

$m = 0$, taking into account the relation (1.17). In this case, the expression of the acoustic transfer $H(x, s, L)$, denoted as $H_0(x, s, L)$, of a ***finite medium*** is reduced to:

$$H_0(x,s,L) = \frac{H_0}{\tanh\left(\frac{s}{\omega_{L,x}}\right)} \quad . \tag{1.56}$$

Figure 1.10 shows the Bode diagrams at $x = 0$ of $H(0,j\omega,L)$ for different values of the fractional order over the range [20; 4000] Hz of the audible and achievable frequencies with a recorder (Figure 1.10).

In order to magnify the different curves in Figure 1.9 for better observation, Figure 1.11 presents the reduced frequency responses $H(0,j\omega,L)/H_0$ with the frequency axis on a linear scale over the range [20; 1000] Hz.

The observation of these frequency responses shows that the influence of the order m is essentially located:

- for ***gain diagrams***, at the peaks of resonances and anti-resonances, quantifiable effects using quality factors Q_{zi} for anti-resonances and Q_{pi} for resonances illustrating well the phenomenon of dissipation associated with visco-thermal losses;
- for ***phase diagrams***, at the crossing points at 0° with a local slope which is all the more important as the order is small, slope which becomes infinite for $m = 0$ (purely conservative case).

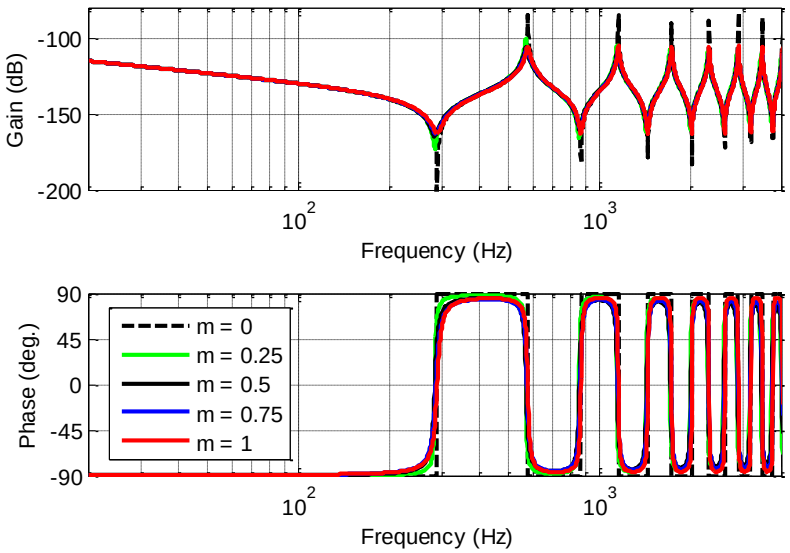

Figure 1.10 – Bode diagrams at $x = 0$ of $H(0, j\omega,L)$ for different values of the fractional order m on the range [20; 4000] Hz of audible and achievable frequencies with a recorder

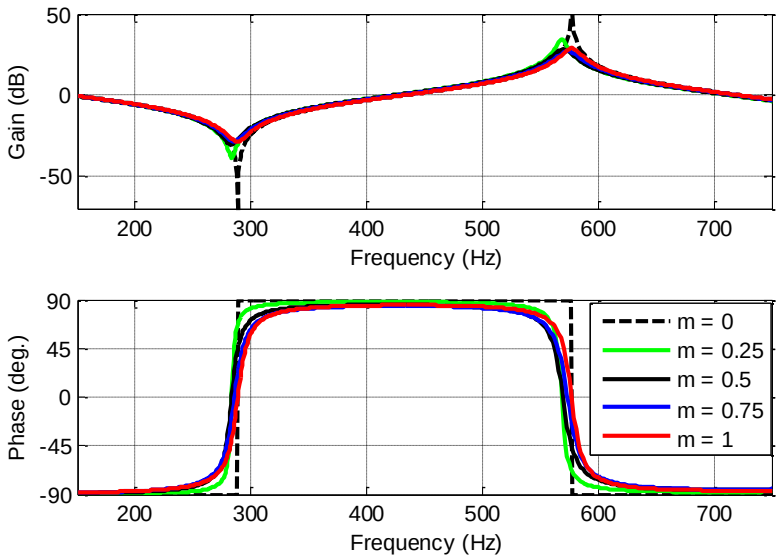

Figure 1.11 – Reduced frequency responses $H(0, j\omega,L) / H_0$ with the frequency axis on a linear scale over the range [150; 750] Hz

1.4 - From the Simplified Fractional Model to its Rational Forms

For the area of study defined by the range [20; 20,000] Hz of the audible frequencies, the analysis presented in the previous paragraph shows that the frequency response $I_m(j\omega)$, is:

$$I_m(j\omega) = \sqrt{\frac{1+\left(j\dfrac{\omega}{\omega_{r,m}}\right)^m}{\left(j\dfrac{\omega}{\omega_{r,m}}\right)^m}} \quad , \tag{1.57}$$

can be reduced to the unit (see paragraph ***1.3.2.1***). This is the reason why for this field of study the frequency response $H(x, j\omega, L)$ defined, as a reminder, by

$$H(x, j\omega, L) = \frac{\overline{Q}_v(x, j\omega, L)}{\overline{P}_{in}(j\omega)} = H_0\ I_m(j\omega)\ T(x, j\omega, L)\ , \tag{1.58}$$

is simplified and noted $\tilde{H}(x, j\omega, L)$, that is:

$$\tilde{H}(x, j\omega, L) = H_0\ T(x, j\omega, L)\ , \tag{1.59}$$

with, always as a reminder,

$$T(x, j\omega, L) = \frac{\tilde{H}(x, j\omega, L)}{H_0} = \frac{1}{\tanh\left(\left(\dfrac{j\omega}{\omega_{L,x}}\right) I_m(j\omega)\right)} = \operatorname{cotanh}\left(\left(\frac{j\omega}{\omega_{L,x}}\right) I_m(j\omega)\right) . \tag{1.60}$$

It is important to note that this simplification does not concern $T(x,j\omega,L)$ because the absence of $I_m(j\omega)$ in relation (1.59) corresponds to the conservative case where ε and m are zero (see paragraph 1.3.3 relation (1.55)). Figure 1.12 shows the block diagrams associated with this simplification in the field of study.

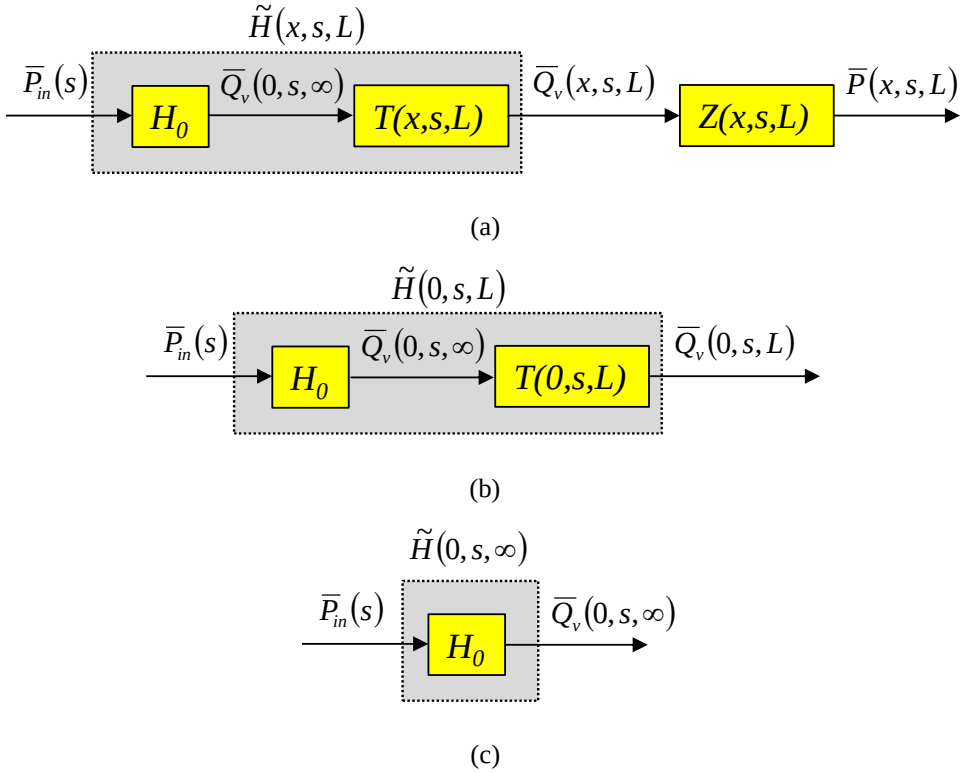

Figure 1.12 – Block diagrams associated with the simplified model: whatever x is between 0 and *L* (a), at *x = 0* for the finite system of length *L* (b) and at *x = 0* for a semi-infinite system (c)

In general, the time simulation of fractional models often requires the use of rational models (Assaf, 2015). Thus, the fractional form defined by the relation (1.58) can be put in a rational form of N cells in cascade, noted $\tilde{H}_{N,c}(x,s,L)$, that is:

$$\tilde{H}_{N,c}(x,s,L)=\frac{A_0}{s}\prod_{i=1}^{N}\left(\frac{1+2\,\zeta_{zi}\,\dfrac{s}{\omega_{zi}}+\left(\dfrac{s}{\omega_{zi}}\right)^2}{1+2\,\zeta_{pi}\,\dfrac{s}{\omega_{pi}}+\left(\dfrac{s}{\omega_{pi}}\right)^2}\right), \tag{1.61}$$

or in a rational form of N cells in parallel, noted $\tilde{H}_{N,p}(x,s,L)$,

$$\tilde{H}_{N,p}(x,s,L)=\frac{A_0}{s}+\sum_{i=1}^{N}\left(\frac{A_i\,s+B_i}{1+2\,\zeta_{pi}\,\dfrac{s}{\omega_{pi}}+\left(\dfrac{s}{\omega_{pi}}\right)^2}\right), \tag{1.62}$$

with $A_0 = H_0\ \omega_{L,x}$ where the ω_{zi} and ζ_{zi} represent the frequencies and the damping factors associated with the anti-resonances, ω_{pi} and ζ_{pi} the frequencies and the damping factors associated with the resonances while changing from the cascade form (1.60) to the parallel form (1.61) by decomposing into simple elements. Note that the parallel rational form facilitates the return to the time domain by inverse Laplace transform and that it is often associated with a decomposition in a modal space (Debut, 2004).

From a theoretical point of view, ω_{zi} corresponds to the roots of the numerator of $T(x,j\omega,L)$, that is:

$$\cosh\left(\left(\frac{j\omega}{\omega_{L,x}}\right)\sqrt{\frac{1+\left(j\frac{\omega}{\omega_{r,m}}\right)^{m}}{\left(j\frac{\omega}{\omega_{r,m}}\right)^{m}}}\right)=0 \quad , \tag{1.63}$$

and the ω_{pi} correspond to the roots of the denominator of $T(x,j\omega,L)$, that is:

$$\sinh\left(\left(\frac{j\omega}{\omega_{L,x}}\right)\sqrt{\frac{1+\left(j\frac{\omega}{\omega_{r,m}}\right)^{m}}{\left(j\frac{\omega}{\omega_{r,m}}\right)^{m}}}\right)=0 \quad . \tag{1.64}$$

From a practical point of view, finding these roots by analytical resolution is complex, if not impossible (Fabrice, 2009). On the other hand, the search by numerical resolution does not pose any particular problem. For example, it is possible to use the fact that the alternation of ω_{zi} and ω_{pi} appears clearly on the phase from when passing at 0 °, from -90 ° to + 90 ° for ω_{zi}, and from + 90 ° to -90 ° for ω_{pi}.

In the context of the work of this thesis, the rational forms of N cells in cascade and in parallel are considered as behavior models whose numerical values of the parameters are obtained using an optimal approach aiming to minimize the difference between the target frequency response defined by the fractional form $\tilde{H}(x,s,L)$ and the frequency response of the rational cascade form $\tilde{H}_{N,c}(x,s,L)$. This digital procedure is available in the ***Frequency Domain System Identification*** (FDSI) module of the CRONE Toolbox (Malti & Victor, 2015).

As an illustration, let us take the acoustic tube used as an example throughout this chapter: $r = 5\text{x}10^{-3}$ m, $L = 0.3$ m, $\rho_a = 1.184$ kg/m^3, $c_a = 346.3$ m/s, $\omega_{L,x} = 1{,}154$ rad/s at $x = 0$, $H_0 = 19.15\text{x}10^{-8}$ m^{3}s^{-1}Pa^{-1} and $A_0 = 22.11\text{x}10^{-5}$ rad/s. Figure 1.13 shows two screenshots from the CRONE Toolbox before optimization (Figure 1.13.a) and after optimization (Figure 1.13.b) at $x = 0$ in the nominal case $m = 0.5$.

The procedure consists, in a first step, from generating the target frequency response $\widetilde{H}(x, j\omega, L)$ of the fractional form which appears in red (Data) in Figure 1.13.a. Then, cells are added one after the other by clicking on the "***Add New Cell***" command in the "***Cells actions***" menu (in green at the top right), then by positioning the mouse cursor on the phase diagram at point considered where the cutting phase of $\widetilde{H}(x, j\omega, L)$ axis 0°, and going from the lowest values (left) to the most important (right). Note that in this graphical interface, the term "cell" corresponds to a polynomial (numerator or denominator). Thus, with each addition in the "Transfer function" menu (in purple at the bottom) a column in blue for the numerator and in yellow for the denominator appears. The first line "***Cell Frequency***" gives the value in rad/s of ω_{zi} or ω_{pi}, the second "***Cell Order***" the highest order of the polynomial (here +2 for the numerator and -2 for the denominator), the third "Local Order" is equal to +1 (for the numerator) and -1 (for the denominator) insofar as these are explicit forms (Malti & Victor, 2015), and finally the fourth "***Damping Factor***" gives the value of ζ_{zi} or ζ_{pi}. All these values in the columns can be modified by clicking in the corresponding box. Thus, in the case of the resonator, all the values of ζ_{zi} or ζ_{pi} are initialized to 0.01.

This first stage of the procedure therefore makes it possible to fix the structure of the behavior model, as well as the initial values of its parameters. The second step is an optimization step launched using the "***Tools***" menu (in orange at the bottom right). For the example of illustration, the result appears in Figure 1.13.b in particular the optimal values of ω_{zi}, ω_{pi}, ζ_{zi} and ζ_{pi}.

Thus, the blue curve corresponds to the frequency response $\widetilde{H}_{N,c}(j\omega, s, L)$ of the rational cascade form (gain and phase) obtained before optimization (Figure 1.13.a) and after optimization (Figure 1.13.b). As for the green lines, these are asymptotic lines.

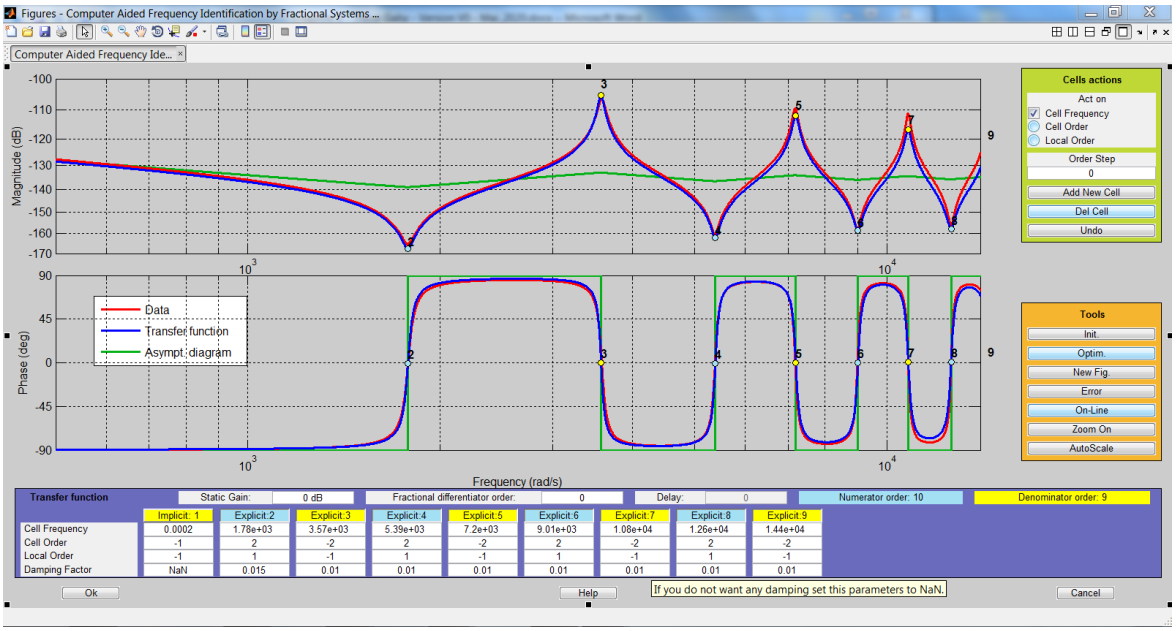

(a)

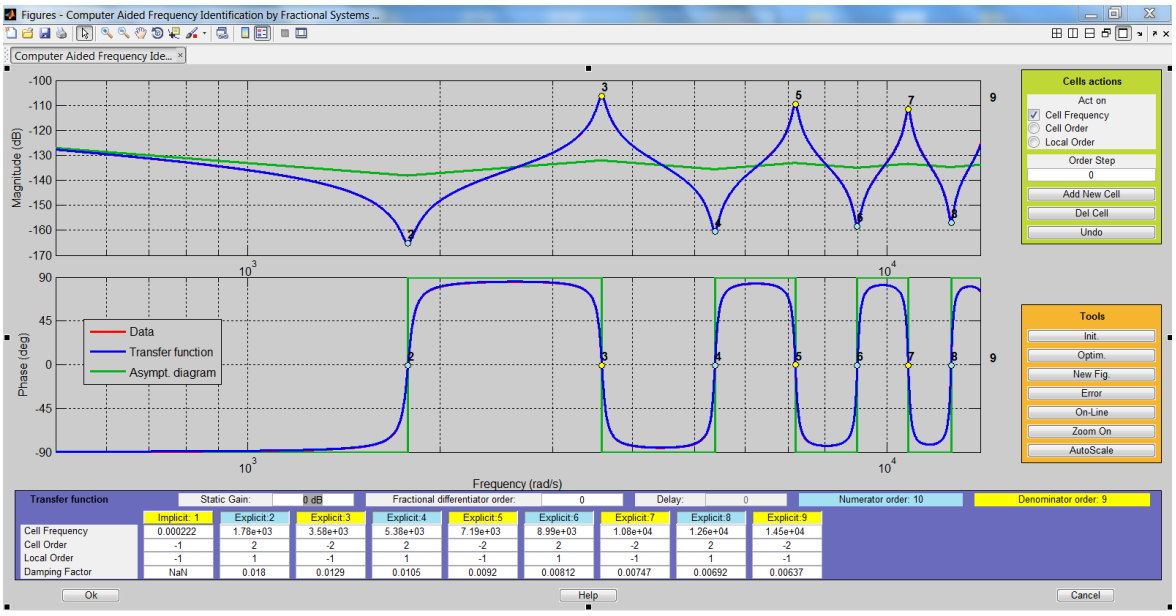

(b)

Figure 1.13 – Screenshots from the CRONE Toolbox before optimization (a) and after optimization (b) at $x = 0$ in the nominal case $m = 0.5$

In summary, the cascade form defined by the relation (1.60) comprises $N = 4$ cells, that is $2N = 8$ "***cells***" as defined in Figure 1.13, to which we must add the integrating cell A_0/s, either in total $N + 1 = 5$ cells, or else $2N + 1 = 9$ "cells".

■ ***Remark***

In linear systems dynamics, in the general case of a polynomial of order 2 having 1 pair of conjugate complex roots, the damping factor ζ and the resonance factor Q associated with this pair are linked by a relation of the form :

$$Q = \frac{1}{2\,\zeta\,\sqrt{1-\zeta^2}} \quad . \tag{1.65}$$

In instrument acoustics (Chaigne & Kergomard, 2013), *and in particular in the specific case of resonators of wind instruments, the damping factors are very small compared to the unit. This is the reason why the relation (1.64) is reduced to:*

$$\forall\ 0<\zeta<<1, \quad Q \approx \frac{1}{2\,\zeta} \quad \Leftrightarrow \quad \zeta \approx \frac{1}{2\,Q}. \tag{1.66}$$

Note that in instrument acoustics, the term quality factor is used in place of the ***resonance factor****. Thus, in many works, the taking into account of the visco-thermal losses is made directly using the parallel rational form defined by the relation (1.62) in which the* ζ_{pi} *are replaced by the corresponding* Q_{pi} *(relation (1.66))* (Chaigne & Kergomard, 2013) *without going through fractional models.* ■

Table 1.2 summarizes the final numerical values of the parameters ω_{zi}, ζ_{zi}, Q_{zi}, ω_{pi}, ζ_{pi} and Q_{pi} of the $N = 4$ cells of the cascade form (relation (1.60)) to which we must not forget the cell number zero, namely the integrator A_0/s.

As for Table 1.3, it gives the numerical values of the parameters A_i, B_i, ω_{pi}, ζ_{pi} *and* Q_{pi} of $N = 4$ cells of the parallel form (relation (1.61)) to which cell A_0/s is added.

Table 1.2 – Final numerical values of the parameters ω_{zi}, ζ_{zi}, Q_{zi}, ω_{pi}, ζ_{pi} and Q_{pi} of the $N = 4$ cells of the cascade form

N	ω_{zi} (rad/s)	ζ_{zi}	Q_{zi}	ω_{pi} (rad/s)	ζ_{pi}	Q_{pi}
1	1780	$18\ 10^{-3}$	27.78	3580	$12.9\ 10^{-3}$	38.76
2	5380	$10.5\ 10^{-3}$	47.62	7190	$9.2\ 10^{-3}$	54.35
3	8990	$8.12\ 10^{-3}$	61.8	10800	$7.47\ 10^{-3}$	66.93
4	12600	$6.92\ 10^{-3}$	72.25	14500	$6.37\ 10^{-3}$	78.5

Table 1.3 – Numerical values of parameters A_i, B_i, ω_{pi}, ζ_{pi} and Q_{pi} of $N = 4$ cells of the parallel form

N	A_i	B_i	ω_{pi} (rad/s)	ζ_{pi}	Q_{pi}
1	$36.02\ 10^{-12}$	$16.63\ 10^{-10}$	3580	$12.9\ 10^{-3}$	38.76
2	$98.24\ 10^{-13}$	$64.99\ 10^{-11}$	7190	$9.2\ 10^{-3}$	54.35
3	$53.38\ 10^{-13}$	$43.07\ 10^{-11}$	10800	$7.47\ 10^{-3}$	66.93
4	$58.98\ 10^{-13}$	$54.47\ 10^{-11}$	14500	$6.37\ 10^{-3}$	78.5

Figure 1.14 presents the Bode diagrams of the response $\tilde{H}_{N,c}(j\omega, s, L)$ of the cascade form (in blue) and the response $\tilde{H}_{N,p}(j\omega, s, L)$ of the parallel form (in green) on the range [100: 2000] Hz where we observe the perfect superposition of the two curves.

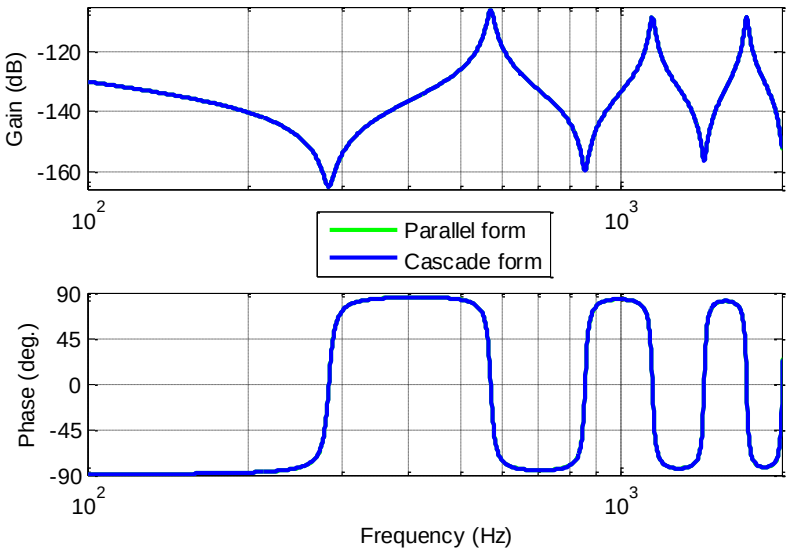

Figure 1.14 – Bode diagrams of the response $\widetilde{H}_{N,C}(j\omega, s, L)$ of the cascade form (in blue) and of the response $\widetilde{H}_{N,P}(j\omega, s, L)$ of the parallel form (in green) over the range [100: 2000] Hz

Thus, the procedure presented in this paragraph, and illustrated in the nominal case m = 0.5, must be repeated for each value of m considered over the interval [0; 1].

1.5 – Conclusion

The structure and progression of this chapter are organized in a didactic way so that readers with no idea about visco-thermal losses in wind instruments can understand the dynamic behavior of an acoustic tube of constant radius. From the two partial differential equations which define the Webster-Lokshin model, a classical resolution in the operational domain leads to the analytical expression of the acoustic impedance and admittance of the function tube of position x, its length L and its radius r.

Moreover, a system vision is proposed aiming to causally decompose the global model into sub-models, thus facilitating analysis in the frequency domain. One of the conclusions of this frequency analysis is that the fractional model can be simplified over the range [20; 20,000] Hz of the audible frequencies. In Addition, the introduction of an uncertainty at the level of the fractional order (whose value considered as nominal is that of the initial Webster-Lokshin model, namely m_0 = 0.5) allows to study the influence of the order m when this varies between 0 (conservative case) and 1. Although the fractional order behavior (fractional integrator) is only present for very low non-audible frequencies (less than 1 Hz), the influence of the fractional order m does appear at resonances and anti-resonances (in the audible frequencies), illustrating well the phenomenon of dissipation associated with visco-thermal losses.

The simulation in the time domain of fractional models requires the establishment of rational forms. Thus, two rational forms composed of an integrator and N second-order cells,

one in cascade and the other in parallel, are introduced. The parameters of the cascade form are then determined using the ***Frequency Domain System Identification*** (FDSI) module of the CRONE Toolbox. As for the parameters of the parallel form, they are obtained by a decomposition into simple elements of the cascade form.

More generally in the fractional model, this study of visco-thermal losses within the resonator of a wind instrument leads to a finding similar to that already made in other fields. Indeed, the main interest of the fractional form resides in the parametric parsimony, that is to say the capacity which the integral-differential operator of non-integer order has to model the greatest number dynamic phenomena with a minimum of parameters. Thus, the study of parametric sensitivity, in particular in the frequency domain, is simpler.

In the case of visco-thermal losses treated in this chapter, the study of the sensitivity is reduced to the only parameter m. The same parametric sensitivity study in the frequency domain with one of the two rational forms presented here is much more complex because this form has $4N$ parameters (4 parameters for each of the N cells, *i.e.* 16 for the example of illustration presented corresponding at the only value $m = 0.5$). The transition to one of the rational forms is then carried out only for time simulation.

Chapter 2- Study of the Nonlinear Exciter of a Wind Musical Instrument

2.1 – Introduction

The self-oscillation mechanism is defined by the instrument's capability to generate an acoustic wave from an energy source that remains stationary or quasi-stationary concerning the acoustic variables. This characteristic is closely linked to the instrument's nonlinear nature. In the realm of musical acoustics, a conventional method outlined by Kergomard and Chaigne (Kergomard & Chaigne, 2013) depicts the instrument (refer to Figure 2.1, (Terrien, 2015)) as a nonlinear excitation system connected to a passive linear resonant system, as discussed in Chapter 1.

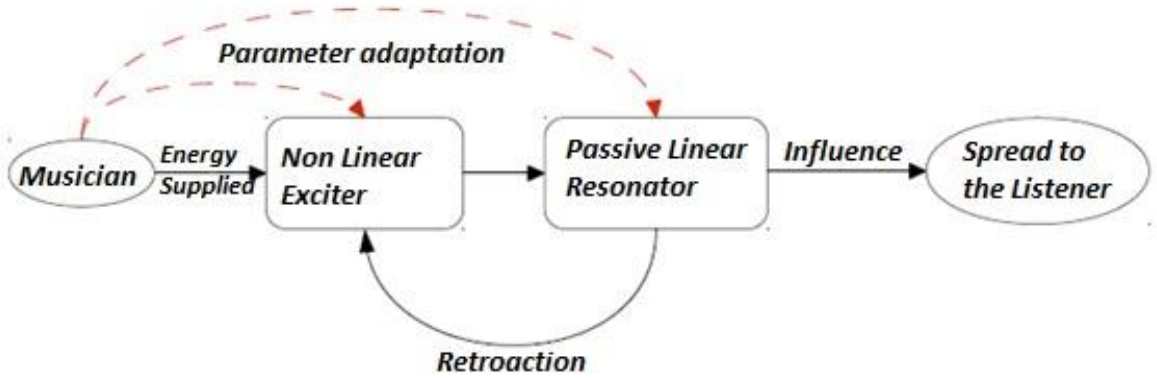

Figure 2.1 – Schematic representation of the mechanism of sound production in self-oscillating musical instruments (see (Terrien, 2015))

Due to its non-linear nature, modeling the exciter and its coupling with the resonator that is the energy source is very complex. Indeed, the phenomenon results from the oscillation of a naturally unstable air jet around a bevel (Figure 2.2). Thus, the self-oscillation mechanism relies on a synchronization of the oscillation of the jet and the acoustic waves. It is therefore necessary that the jet-bevel system excites the resonator at the periodicity of the acoustic field.

In order to fully understand the phenomena involved and to be able to reproduce them by numerical simulation, this chapter proposes, first of all, a modeling by the proper diagram and parameters of the various essential elements of the system, then by recalling the mechanism of sound production. Then, from a bibliographic synthesis, a complete nonlinear model frequently used in the literature is developed. Moreover, after focusing on the poor digital conditioning of such a model, a solution is proposed in order to be able to develop a digital simulator programmed in MatLab/Simulink. A scenario is then defined for several values of the pressure at the input of the mouthpiece of the flute. This scenario is defined by respecting, not only the

domain of validity of the nonlinear model, but also the values of pressure achievable experimentally by the artificial mouth presented in chapter 3. Thus, for this field of study, a detailed analysis of the time responses simulated is proposed. This analysis makes it possible, in particular, to observe that the variations of a certain number of physical quantities (pressure at the input of the resonator, acoustic speed, etc.) are small and around zero. On the basis of this observation, a linearization is developed leading to two linearized models, one for the analysis of the start-up phase of the simulation (*phase 1*), the other for that of the self-oscillations (*phase 3*). Finally, the last paragraph analyzes the conditions of self-oscillation of such a system.

2.2 – Modelling

2.2.1 – Schematic and Configuration of the Exciter

Figure 2.2 (which is a more detailed representation of the flute shown in Figure 1.3 in Chapter 1) shows a cross section of a recorder, as well as a schematic representation of its exciting mechanism (consisting of the interaction of an air jet with a bevel) where the notations that appear in the figure are defined by:

- **1**: outlet of the channel; **2**: bevel; **3**: resonator (air column); **4**: exciter;
- $R = (o\,;\vec{x}\,;\vec{y})$: local reference associated with the jet;
- h: height of the spout channel;
- w: distance between the outlet of the channel and the tip of the bevel;
- x_0: lateral offset of the tip of the bevel from the longitudinal $\vec{y}$ axis of the channel;
- $P_m(t) = P_m^e + p_m(t)$: pressure generated at the input of the mouthpiece, P_m^e is the stationary component at the operating point and $p_m(t)$ the variation around P_m^e.

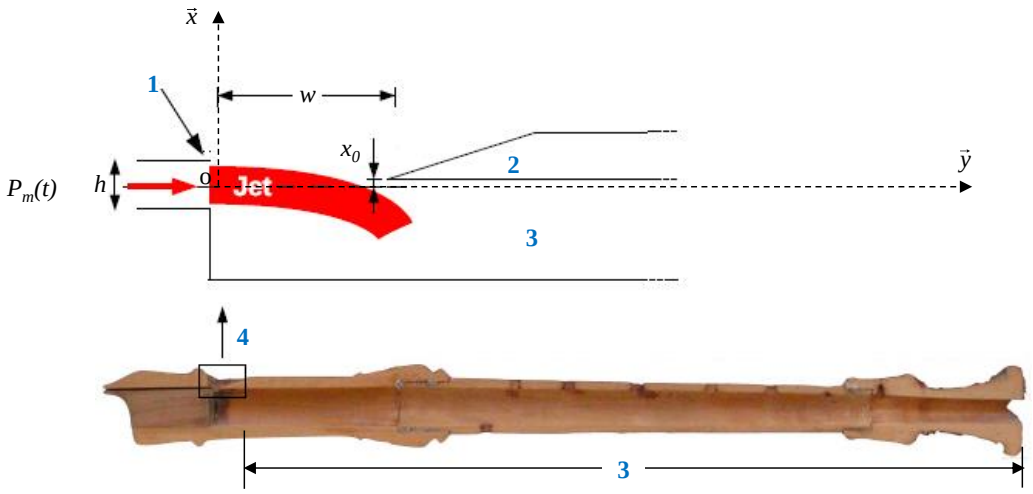

Figure 2.2 – Cross section of a recorder and schematic representation of its excitation mechanism consisting of the interaction of an air jet with a bevel with: 1: spout channel output; 2: bevel; 3: resonator (air column); 4: exciter (see (Terrien, 2015))

2.2.2 - Sound Production Mechanism: Reminder

From a causal point of view, the generation of a pressure input $P_m(t)$ at the mouthpiece of the flute (imposed by the musician or by an artificial mouth device as defined in chapter 3) gives rise to a flow in the spout channel (Figure 2.2). Upon exiting the channel, the viscosity of the air hinders the flow from adhering to the walls' geometry (Terrien S. , 2015). Consequently, the flow deviates from the walls, resulting in an air jet with an initial speed denoted as $U_j(x = 0, t)$ at $x = 0$. This air jet exhibits inherent instability (Kergomard & Chaigne, 2013). While the flow near the origin at $x = 0$ may initially display a well-ordered pattern, the development of eddies becomes apparent as the flow moves away from the starting point. The inherent instability of the air jet causes even the slightest disturbance to be magnified over time (Kergomard & Chaigne, 2013).

The jet created at the channel output flows inside the excitation window. It meets the bevel, the point of which is located at a distance w from the channel output and laterally offset by x_0 with respect to the longitudinal axis $\vec{y}$ of the flow. The interaction between the jet and the bevel induces a hydrodynamic feedback on the jet, a crucial element in initiating the jet's oscillation by introducing its initial disturbances (Terrien, 2015). Given the inherent instability of the air jet, disturbances naturally magnify along its path from the channel exit to the bevel, resulting in oscillations on both sides of the bevel. This oscillation leads to a periodic alternation of flow injection into and out of the instrument, forming the aero-acoustic source of pressure that channels energy to the resonator (Kergomard & Chaigne, 2013).

The acoustic waves generated within the resonator, as discussed in Chapter 1, propagate and undergo reflection, primarily occurring at the first open hole. The combination of the outgoing wave and its reflected counterpart results in a series of standing waves within the resonator. These standing waves, in turn, influence the returning jet at the channel exit, completing the self-oscillation loop. The initial disturbance of the jet, caused by the standing waves, perpetuates its oscillation, sustaining the mechanism responsible for sound production.

2.2.3 - From a Phenomenon with Distributed Parameters to a Model with Localized Parameters

The sound production models in flutes are founded on the loop system depicted in Figure 2.3 (Terrien, 2015). These models intricately involve the representation and modeling of each of the three primary phenomena:

- the instability of the jet;
- the aero-acoustic sources related to the jet-bevel interaction;
- the propagation of acoustic waves in the resonator.

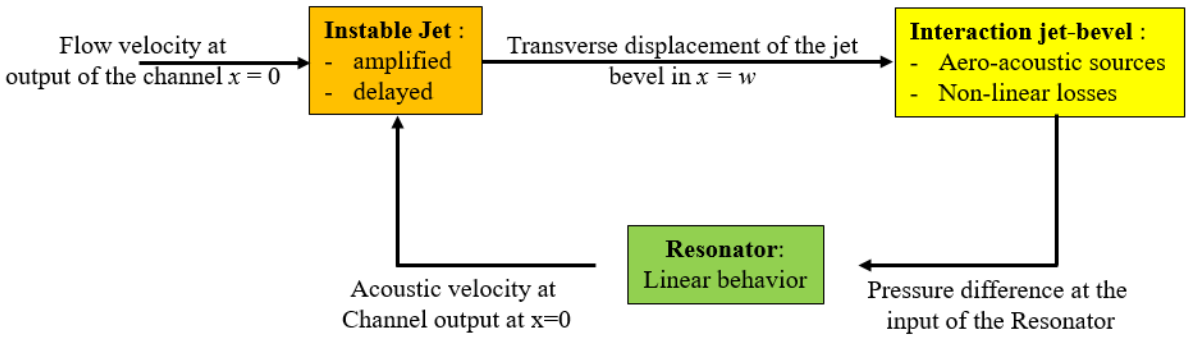

Figure 2.3 – Functional diagram of the loop system describing the self-oscillation mechanism of instruments of the flute family (see (Terrien, 2015))

The division of the three key phenomena in action and the assumption that their interactions are localized give rise to a distinctive and significant limitation in this representation. This approach might appear counterintuitive as the boundaries between these distinct elements remain somewhat indistinct. An illustrative example is the challenge of determining the precise location of flow sources arising from the oscillation of the jet (Terrien 2015). The inherent complexity lies in the interconnected nature of these phenomena, making it challenging to precisely define their individual boundaries within the system.

Nevertheless, these phenomena operate on different scales, necessitating distinct hypotheses. For low frequencies, corresponding to the initial acoustic resonances, the region affected by the developing unstable air jet is relatively small compared to the wavelengths of the acoustic waves. Consequently, the jet can be analyzed under the assumption of incompressibility, a hypothesis that becomes incompatible with the description of wave propagation within the resonator. As highlighted by Fabre and Hirschberg (Hirschberg, 2000), the ability to represent these diverse phenomena as distinct blocks with localized interactions is made possible precisely because they are described under different, albeit seemingly paradoxical, assumptions. In the functional diagram of Figure 2.3, each highlighted block represents a specific aspect of the system, with the physical phenomena in action and their corresponding models explained in the subsequent part of this paragraph. This comprehensive model, incorporating different assumptions for various phenomena, stands as the most widely utilized in the literature (Hirschberg, 2000).

2.2.3.1 - Receptivity: Initial Disturbance of the Jet

Once self-oscillations are established, the disturbance of the jet is induced by the acoustic field within the resonator. Because of the assumption of a non-viscous fluid used in describing the jet, this phenomenon, termed receptivity, is considered to be localized at the point where the jet separates, specifically at the channel exit at $x = 0$ (Kergomard & Chaigne, 2013). Various receptivity models have been proposed in the literature, notably by Fabre and

Hirschberg (Hirschberg, 2000) and by Blanc (F Blanc, 2014). These models offer insights into how the acoustic field influences and triggers disturbances in the jet, contributing to a more comprehensive understanding of the self-oscillation mechanism.

In the rest of this chapter, the applied model refers the one proposed by de la Cuadra (Cuadra P. d., 2005). It is based on Schlieren visualizations of a jet subjected to a transverse acoustic field. One of the hypotheses which reduces the domain of validity of this model is that the pressure $P_m(t) = P_m^e + p_m(t)$ in the musician's mouth or the artificial mouth (see Chapter 3) is assumed to be stationary (or quasi-stationary), an assumption which leads to a central jet speed $U_j(x=0,t) = U_j^e + u_j(x=0,t)$ at the exit of the channel also stationary. This is the reason why in the rest of this chapter, we consider that:

$$\begin{cases} P_m(t) \approx P_m^e \\ U_j(x=0,t) \approx U_j^e \end{cases}, \tag{2.1}$$

where, according to Bernoulli's law in stationary system at the channel exit (Cuadra P. d., 2005) ,

$$U_j^e = \sqrt{\frac{2\,P_m^e}{\rho}}\ , \tag{2.2}$$

ρ being the density of air.

Thus, for this domain of validity, the initial disturbance of the jet at $x = 0$ at the exit of the channel is represented by a transverse displacement $\eta_0(x = 0, t)$, noted $\eta_0(t)$, linked to the acoustic speed $v_{ac}(t)$ of the resonator always at $x = 0$ by a relation of the form:

$$\eta_0(t) = \frac{h}{U_j^e}\, v_{ac}(t)\ . \tag{2.3}$$

2.2.3.2 - Jet Instability: Amplification and Convection of Disturbances

As previously mentioned, the air jet extending between the channel exit and the bevel is inherently unstable. This instability, recognized as Kelvin-Helmholtz instability (Reid, 2002), arises from the natural instability of shear layers characterized by different velocities, essentially the interfaces between the jet and the stationary external environment. The innate instability of the jet leads to the amplification and propagation of even the slightest disturbances. Rayleigh (Rayleigh, 1984)) was the first to propose a linear description of this phenomenon, specifically in the context of small perturbations affecting a semi-infinite jet. The amplification of perturbations was expressed as an exponential function correlated with the convection distance.

In flute family instruments, the jet evolves within an excitation window, bounded on one end by the channel at $x = 0$ and on the other by the interacting bevel at $x = w$. An experimental investigation conducted by de la Cuadra (Cuadra P. d., 2005) demonstrated that the exponential amplification of the initial disturbance $\eta_0(t)$ with the convection distance x remains a reasonably accurate approximation. In the case of the flute, specifically at the bevel located at $x = w$, the transverse displacement $\eta(w, t)$ of the disturbance can be expressed as follows:

$$\eta(x = w, t) = \eta_0(t - \tau)\ \exp(\alpha_i\ w)\ , \tag{2.4}$$

where, still according to de la Cuadra (Cuadra P. d., 2005), the estimate of the amplification factor α_i as a function of the height h of the channel is approximated by:

$$\alpha_i \approx \frac{0.4}{h}\ . \tag{2.5}$$

The delay τ, introduced in equation (2.4) is linked to the convection time of the initial disturbance $\eta_0(t)$ through the jet, from the exit of the channel at $x = 0$ to the wedge at $x = w$. Several experimental results (Cuadra, Vergez , & Fabre, 2007) (Nolle, 1998) and theoretical studies (Rayleigh, 1984) have revealed that, in a steady state, the convection speed C_v^e of transverse disturbances along a jet is correlated with the difference in speed between the jet and the external environment $C_v^e \in \left[0.3\,U_j^e\,;\,0.5\,U_j^e\right]$. Therefore, through this chapter, the mean value $C_v^e = 0.4\,U_j^e$ is used and the expression of the delay τ can be represented as follows:

$$\tau = \frac{w}{0.4\,U_j^e}\ . \tag{2.6}$$

2.2.3.3 - Jet-Bevel Interaction: Aero-Acoustic Sources

In wind instruments, the oscillation of the jet around the bevel serves as an exciter, generating the acoustic energy transmitted to the resonator. While Helmholtz initially described this source using a monopole, the dipole modeling introduced by Rayleigh (Rayleigh, 1984), is now commonly employed. The jet-drive model, initially proposed by Coltman (Coltman J. , 1976), and later refined by Verge (Verge M. , 1995) (Verge, Hirschberg, & Caussé, 1997) is based on the representation of the source term through a force. Figure 2.4 schematically illustrates the behavior of the jet in this context.

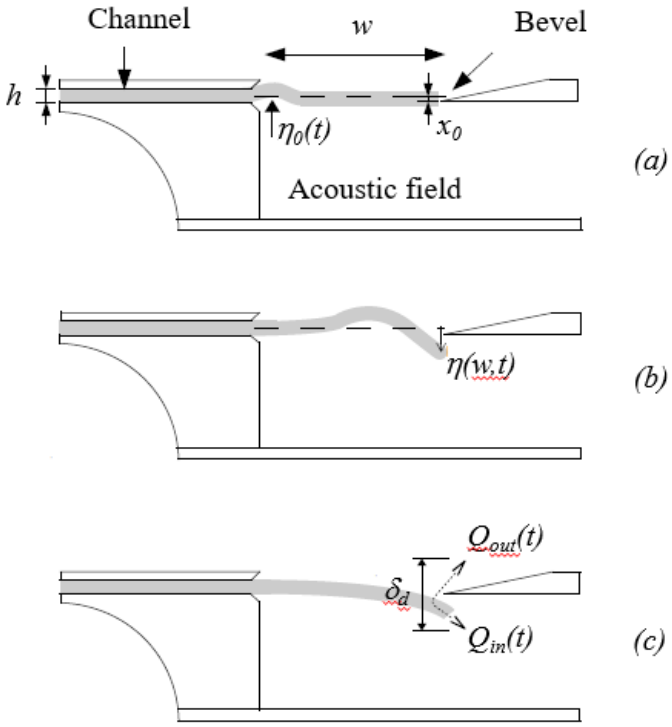

Figure 2.4 – Schematic representation of the behavior of the jet, according to Fabre in [Chaigne, 2013]: (a) disturbance of the jet at the outlet of the channel by the acoustic field present in the resonator; (b) convection and amplification of the disturbance (c) oscillation of the jet around the bevel which gives rise to the aero-acoustic sources

Based on the bevel (Figure 2.4.a), the jet, experiencing a transverse displacement $\eta(w,t)$, oscillates on both side of this bevel (Figure 2.4.b). The flow rate associated with the jet is subsequently split into two separate flow rates: the first one $Q_{in}(t)$ enters the resonator whereas the second $Q_{out}(t)$ leaves the resonator (Figure 2.4.c). Both flow sources in phase opposition are located at two distinct points close to the bevel; however, they separated by an equivalent distance δ_d. To calculate the potential difference, Verge (Verge M. , 1995) estimated:

$$\delta_d \approx \frac{4}{\pi}\sqrt{2\,h\,w}\ . \tag{2.7}$$

Since this equivalent distance δ_d is tiny compared to the acoustic wavelengths, the mass of air situated between the two flow injection points can be treated as incompressible. The reciprocal sloshing motion of this air mass, prompted by the oscillation of the jet, imparts a force on the acoustic field. This force is represented by a pressure difference, denoted as $\Delta p_{src}(t)$, whose expression is described as follows (Terrien S. , 2015):

$$\Delta p_{src}(t) = \left(\frac{\rho\,\delta_d\,b\,U_j^e}{w}\right)\frac{d}{dt}\left[\tanh\left(\frac{\eta(w,t)-x_0}{b}\right)\right], \tag{2.8}$$

where b indicates the estimated half-thickness of the jet and is expressed as follows (M P Verge B. F., 1994) (Ségoufin C. , 2000):

$$b = \frac{2}{5} h \ , \tag{2.9}$$

where *tanh(.)* represents the hyperbolic tangent function.

Additionally, the excitation window of the flute, spanning from the channel exit at $x = 0$ to the bevel at $x = w$, represents both an open end and a constriction when viewed from the resonator's perspective. In practice, its cross-sectional area is often smaller than the bore section of the instrument. Consequently, the acoustic speeds observed in this region can be significant and generally cannot be disregarded in relation to the speed of the jet. The presence of a sharp edge (the bevel), in conjunction with the effects of viscosity, induces flow separation at this juncture (Kergomard & Chaigne, 2013). This, in turn, leads to the detachment of vortices at the level of the bevel, as experimentally illustrated by Fabre and Hirschberg (B Fabre, 1996).

Considering this phenomenon associated with energy loss in instrument models appears crucial for accurately describing the mechanisms governing the saturation of oscillation amplitude (B Fabre, 1996) (R Auvray, 2012). While various models have been suggested to address this phenomenon (B Fabre, 1996), a commonly adopted approach, primarily due to its simplicity (Kergomard & Chaigne, 2013)), involves modeling it through an additional pressure difference $\Delta p_{los}(t)$ between the two sides of the bevel, as follows:

$$\Delta p_{los}(t) = -\frac{\rho}{2}\left(\frac{v_{ac}(t)}{\alpha_{vc}}\right)^2 \operatorname{sign}\left[v_{ac}(t)\right] \ , \tag{2.10}$$

where α_{vc} is a factor corresponding to the effect of *vena contracta*, estimated at 0.6 in the case of a sharp arrest (Falkovich, 2011) and where represents using the sign function.

Finally, the aero-acoustic pressure source $\Delta p(t)$ at the bevel is expressed as follows (Terrien S. , 2015):

$$\Delta p(t) = \Delta p_{src}(t) + \Delta p_{los}(t) \ . \tag{2.11}$$

2.2.3.4 – Complete Model

The complete model of the instrument retained within the framework of this study is finally composed of a system of three equations, each one being linked to a given element of the looped system shown in (Figure 2.5), namely:

$$\begin{cases} \eta(w,t) = \dfrac{h\exp(\alpha_i\, w)}{U_j^e}\; v_{ac}(t-\tau) \\ \Delta p(t) = \left(\dfrac{\rho\,\delta_d\, b\, U_j^e}{w}\right)\dfrac{d}{dt}\left[\tanh\left(\dfrac{\eta(w,t)-x_0}{b}\right)\right] - \dfrac{\rho}{2}\left(\dfrac{v_{ac}(t)}{\alpha_{vc}}\right)^2 \operatorname{sign}\left[v_{ac}(t)\right] \\ v_{ac}(t) = \dfrac{1}{S}\;\mathrm{TL}^{-1}\left\{Y_{in}(s,L)\;\Delta P(s)\right\} \\ \text{with}\;\; \tau = \dfrac{w}{0.4\,U_j^e} \end{cases} \quad (2.12)$$

where S and L represent the section and the length of the resonator, $Y_{in}(s,L)$ its input admittance (defined in Chapter 1) and $\Delta P(s) = \mathrm{TL}\{\Delta p(t)\}$, TL designating the Laplace Transform.

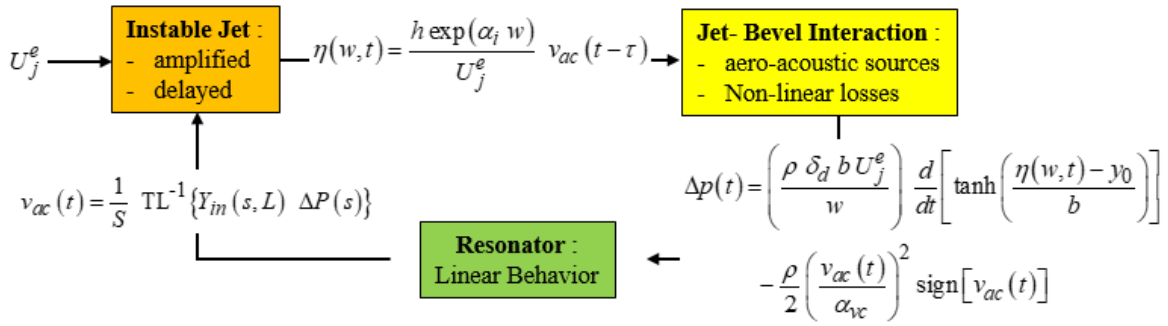

Figure 2.5 – Functional diagram of the complete model

2.2.3.5 - Limits of the Model: Reminder of the Validated Domain

The capability of the comprehensive model to qualitatively replicate numerous phenomena observed experimentally has been established in various studies (Auvray, Fabre, & Lagrée, 2012) (S Terrien, 2012) . However, like any model, its validity is confined to a specific range, and this constraint should be considered when interpreting the results.

The theoretical validity of the linear description of jet instability is limited to small amplitudes of transverse deflection $\eta(x,t)$. When the value of $\eta(x,t)$ approaches the thickness of the jet, the jet folds upon itself, creating a sequence of vortices that can be represented as a Von Karman alley (Kergomard & Chaigne, 2013). It's important to note that the model presented by the system of equations (2.12) does not incorporate this nonlinear phenomenon.

On the other hand, when the jet speed U_j^e becomes sufficiently high, a transition to a turbulent state can be observed. As a reminder (Terrien S. , 2015), , the transition from a laminar (linear) flow to a turbulent (nonlinear) flow typically occurs at a Reynolds number between 2500 and 3000. The Reynolds number represents the ratio between inertial forces and viscous

forces. According to Fabre (Kergomard & Chaigne, 2013), in the case of a turbulent flow at the channel exit, the modeling should account for various factors not addressed in the current model.

Finally, the model is well suited (Terrien S. , 2015) for:
- low values of the number of Strouhal θ defined by:

$$\theta = \frac{w}{U_j^e} f_0 \ , \tag{2.13}$$

where f_0 represents the self-oscillation frequency in Hz of the waves within the resonator;
- jets with a thin thickness compared to the length w;
- rather large hydrodynamic wavelengths.

2.3 – Numerical Simulation

2.3.1 – Digital Packaging Problem

The complete model, as defined by the system of equations (2.12), is poorly conditioned from a numerical point of view. Indeed, the presence of a derivation in the second equation of the system (2.12) reveals a causality problem. Moreover, assuming that the derivation can be programmed without posing a numerical problem, if the initial conditions associated with the variables $\eta(w,t)$, $v_{ac}(t)$ and $\Delta p(t)$ are zero (which is the case physically as long as the pressure $P_m(t)$ at the mouthpiece input is zero), then there is no generating process to initiate the start of a transient system which must then make it possible to reach a steady periodic system imposed by the self-oscillation conditions. Finally, the presence of the flow speed $U_j(t)$ at the denominator of the first equation of the system (2.12) excludes any zero initial value of this speed at the start of the digital simulation, and therefore of the pressure $P_m(t)$ at the entry of the mouthpiece of the flute, a situation however very physically realistic.

The solution adopted in this thesis concerning the derivation is the use of a frequency truncated differentiator whose expression $D(s)$ in the symbolic domain is defined by:

$$D(s) = \frac{s}{\left(1 + \frac{s}{\omega_c}\right)^{n_h}} \ , \tag{2.14}$$

ω_c being the cutoff pulse (in rad/s) and n_h the order of the low-pass filter. The useful effect of the low-pass filter is to prevent $D(s)$ from tending to infinity as s tends to infinity (i.e. the first instants taking into account the applicable time-frequency duality to this linear operator), the parasitic effect being its phase shift all the more important as the order n_h is important. Faced with this dilemma, a good compromise is $n_h = 2$ which leads to:

$$\lim_{s \to \infty} D(s) \to 0 \ . \tag{2.15}$$

This value of n_h must be combined with a cut-off pulse ω_c compared to the largest natural un-damped pulse ω_{pi} of the rational form of the impedance $Y_{in}(s,L)$ as defined in Chapter 1.

It is important to note that the choice of this operator makes it possible, not only to solve the numerical problem related to the derivation, but also to introduce a generator process allowing, in the presence of zero initial conditions, to initially trigger the start of a transient system then leading to a stationary periodic system (self-oscillation conditions). The following paragraph illustrates and then demonstrates this result.

2.3.2 - Simulator Developed using MatLab / Simulink

The complete model in the presence of operator $D(s)$ is programmed in MatLab / Simulink with the following parametric values:

ρ =1.184 kg/m^3:	density of air at 25°C;
ν = 15.6x10^{-6} m^2/s:	kinematic viscosity of air at 25°C;
h = 10^{-3} m:	height of the spout channel;
w = 4.25x10^{-3} m:	distance between the outlet of the nozzle channel and the tip of the bevel;
b = 0.4x10^{-3} m:	half-thickness of the jet;
δ_d = 3.7x10^{-3} m:	equivalent distance between the 2 sources of flow Q_{in} and Q_{out} at the level of the bevel
α_{vc} = 0.6:	effect factor *vena contracta*;
x_0 =0.1x10^{-3} m:	lateral offset of the tip of the bevel from the longitudinal axis of the channel;
L = 0.3 m:	length of the resonator tube;
r = 5x10^{-3} m:	radius of the resonator tube;
S = 7.854x10^{-5} m^2:	section of the resonator tube;
n_h = 2:	order of the low-pass filter of the operator $D(s)$;
ω_c = 2πx50 000 rad/s:	cutoff pulse of the low-pass filter of the operator $D(s)$.

As a reminder (see Chapter 1), Figure 2.6 shows the frequency response of the input admittance $Y_{in}(s,L)$ of the resonator on the range [100; 2000] Hz and Table 2.1 gives the numerical values of the parameters A_i, B_i, ω_{pi}, ζ_{pi} and Q_{pi} of its parallel rational form for the $N = 4$ first modes of the resonator.

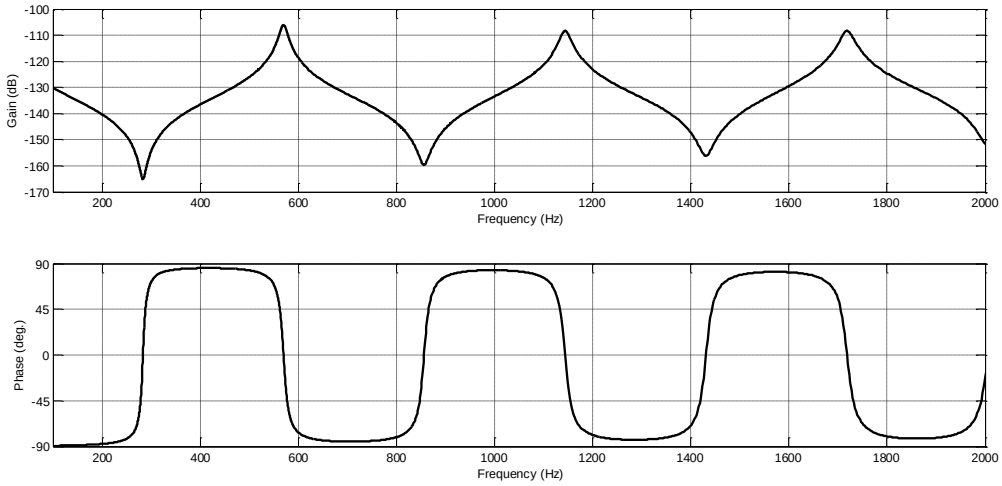

Figure 2.6 – Frequency response of the input admittance *Yin(s, L)* of the resonator considered over the range [100; 2000] Hz.

Table 2.1 – Numerical values of the parameters A_i, B_i, ω_{pi}, ζ_{pi} and Q_{pi} of the parallel rational form of the input admittance $Y_{in}(s,L)$ for the $N = 4$ first modes of the resonator

N	A_i	B_i	ω_{pi} (rad/s)	ζ_{pi}	Q_{pi}
1	$36.02\ 10^{-12}$	$16.63\ 10^{-10}$	$2\pi\ 570$	$12.9\ 10^{-3}$	38.76
2	$98.24\ 10^{-13}$	$64.99\ 10^{-11}$	$2\pi\ 1145$	$9.2\ 10^{-3}$	54.35
3	$53.38\ 10^{-13}$	$43.07\ 10^{-11}$	$2\pi\ 1720$	$7.47\ 10^{-3}$	66.93
4	$58.98\ 10^{-13}$	$54.47\ 10^{-11}$	$2\pi\ 2309$	$6.37\ 10^{-3}$	78.5

■ ***Remark 2.1***

With a ratio ω_c/ω_{p4}, the cut-off pulsation $\omega_c = 2\pi$ x 50,000 rad/s of the low-pass filter of the operator D(s) is sufficiently large compared to the largest natural non-damped pulsation $\omega_{p4} = 2\pi$ x 2,309 rad/s of the rational form of the impedance $Y_{in}(s,L)$. Thus for times $t >> \tau_c = 1/\omega_c = 3.18$ x 10^{-6} s, the two differentiation operators, D(s) and s, have the same behavior.

■ ***Remark 2.2***

In the dynamics of linear systems, in the general case of a polynomial of order 2 having 1 pair of conjugate complex roots, the natural undamped pulsation ω_n and the resonance pulsation ω_r are linked by a relation of the form $\omega_r = \omega_n \sqrt{1-2\zeta^2}$ where ζ represents the associated damping factor. In acoustic instruments, and in particular in the particular case of wind instrument resonators, the damping factors ζ_{pi} are very small compared to unity (see table 2.1). This is the reason why the natural un-damped pulses ω_{pi} and the resonance pulses ω_{ri} associated with each of the i modes of the resonator are almost equal, which is to say that the

ratio $\omega_{ri}/\omega_{ni} = \sqrt{1-2\zeta_{pi}^2}$ *is close to unity. For more illustration, table 2.2 gives the numerical values of this ratio for the first 4 modes of the resonator considered in table 2.1.*

Table 2.2 – Numerical values of the ratio for the first 4 modes of the resonator considered

N	ζ_{pi}	ω_{ri}/ω_{ni}
1	$12.9\ 10^{-3}$	0.9998
2	$9.2\ 10^{-3}$	0.9999
3	$7.47\ 10^{-3}$	0.9999
4	$6.37\ 10^{-3}$	1

■

Figure 2.7 shows the parametric configuration chosen for the Simulink solver.

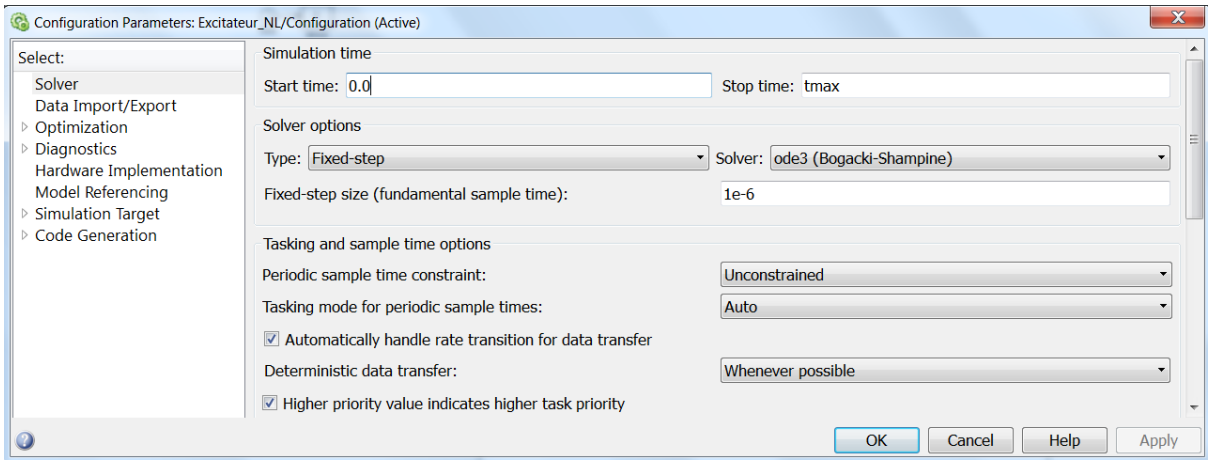

Figure 2.7 – Parametric configuration retained for the Simulink solver

The initial conditions of the various simulations carried out are:

$$\begin{cases} P_m\left(0^+\right) = P_m^e \Rightarrow U_j\left(0^+\right) = U_j^e \\ v_{ac}\left(0^+\right) = 0 \\ \eta\left(w,0^+\right) = 0 \\ \dot{\eta}\left(w,0^+\right) = 0 \Rightarrow \text{ thanks to the presence of } D(s) \\ \Delta p\left(0^+\right) = 0 \end{cases}, \qquad (2.16)$$

and this for 13 different values of the pressure P_m^e between 400 Pa and 1000 Pa, with a step of 50 Pa. For each of its simulations, three phases appear:

- ***phase 1:*** start-up with a convergent transient system;
- ***phase 2:*** divergent transient system;
- ***phase 3:*** stationary periodic system.

Among these 13 tests, two (corresponding to the limits of the membership interval of P_m^e) are presented and analyzed by way of illustration:

- ***example 1:*** $P_m^e = 400$ Pa , $U_j^e = 26$ m/s and $\tau = 0.409$ ms ;

- ***example 2:*** $P_m^e = 1000$ Pa , $U_j^e = 41$ m/s and $\tau = 0.259$ ms.

For each of these two examples, three families of time responses are proposed for:
- the total duration of the simulation from t_0 to t_{max}, with $t_0 = 0$ s and $t_{max} = 1$ s;
- phase 1 from t_0 to t_1;
- phase 3 from t_2 to $t_{max} = 1$ s.

Figure 2.8, for a pressure $P_m^e = 400$ Pa (on the left) and $P_m^e = 1000$ Pa (on the right), shows the time responses of the pressure $\Delta p(t)$ at the input of the resonator ((a) and (b)), the acoustic velocity $v_{ac}(t)$ ((c) and (d)) and the transverse displacement $\eta(w,t)$ of the jet ((e) and (f)). Observing the results allows us to make the following remarks:

- the duration of ***phase 1*** depends on the value of the delay τ and therefore on the value of P_m^e. Thus, the lower the delay τ (that is, the greater the P_m^e pressure), the shorter ***phase 1***. Focusing on $P_m^e = 400$ Pa (left), the convergent transient system of ***phase 1*** is not visible for $P_m^e = 1000$ Pa (right) because the divergent transient system of ***phase 2*** quickly overlaps;

- The shorter the duration of ***phase 2*** is the greater the pressure P_m^e, thus leading to the onset of the steady-state periodic system of ***phase 3*** more quickly.

Taking into account these remarks, Figure 2.9 presents, only for a pressure $P_m^e = 400$ Pa, the time responses obtained during ***phase 1*** of the pressure $\Delta p(t)$ at the input of the resonator (a), of the acoustic speed $v_{ac}(t)$ (b) and the transverse displacement $\eta(w,t)$ of the jet (c). A detailed analysis of this ***phase 1*** is proposed in paragraph **2.4 - Linearized model**.

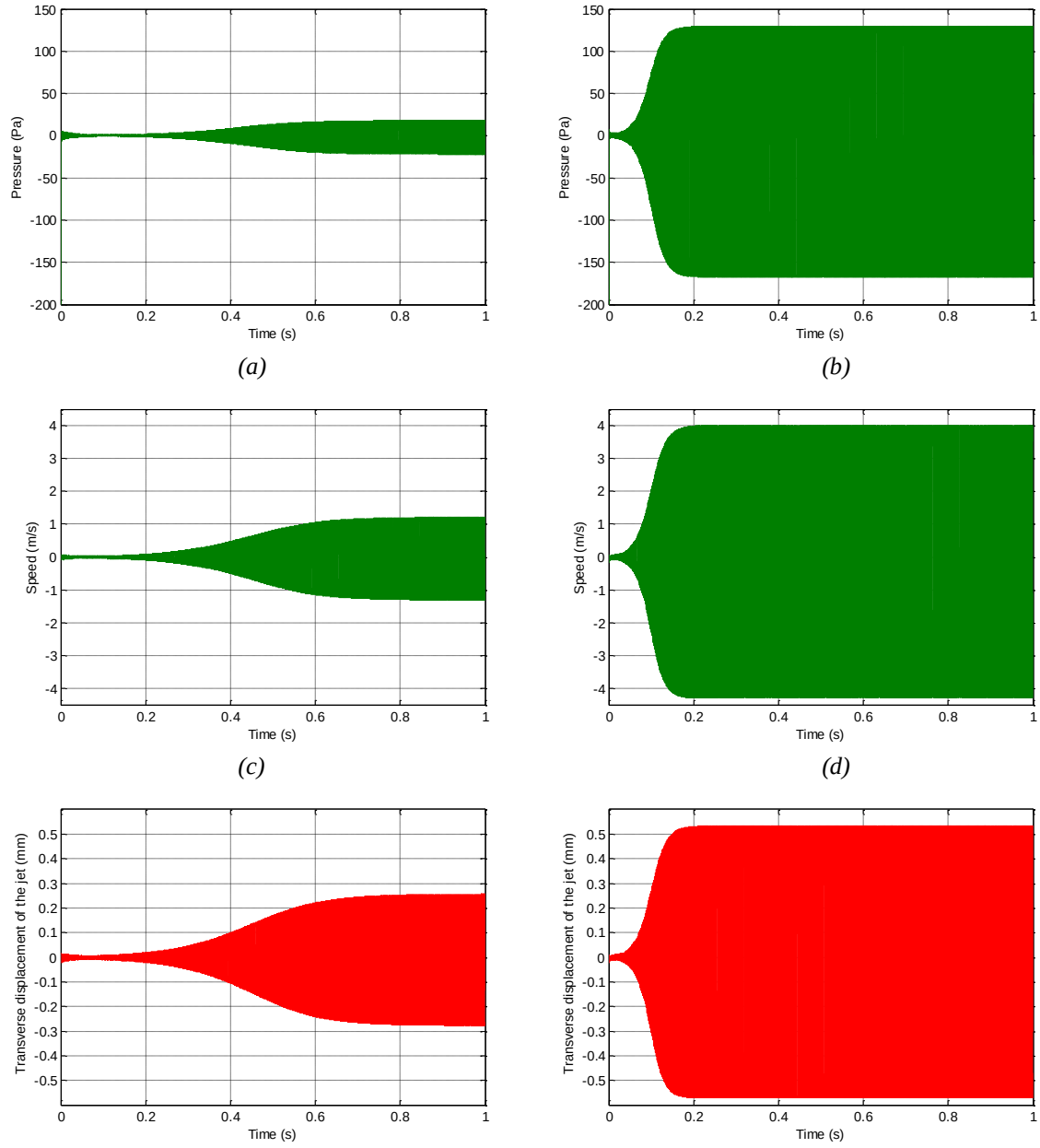

Figure 2.8 – Time responses obtained for a pressure = 400 Pa (on the left) and = 1000 Pa (on the right) concerning: - the pressure $\Delta p(t)$ at the input of the resonator (a) and (b); - the acoustic speed $v_{ac}(t)$ (c) and (d); - the transverse displacement $\eta(w, t)$ of the jet (e) and (f)

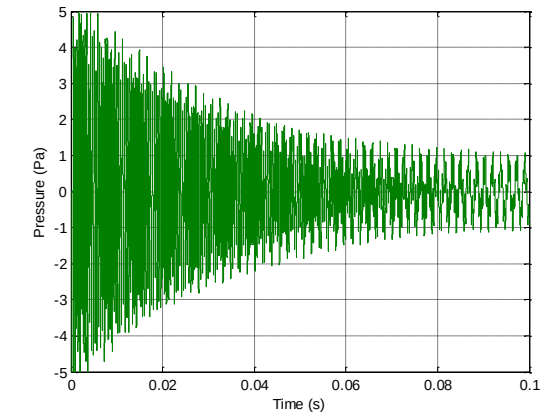

(a)

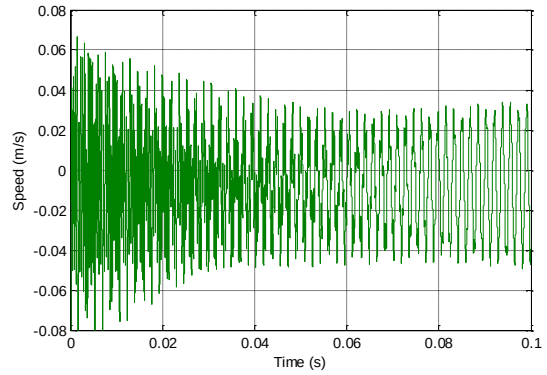

(b)

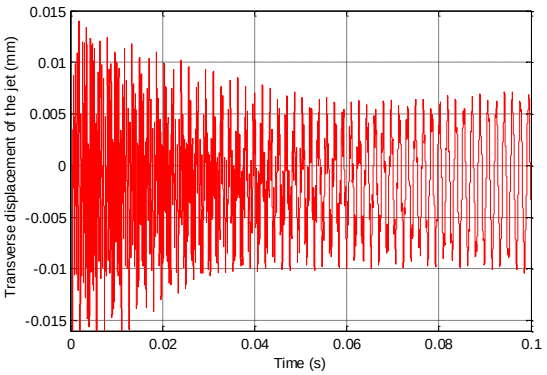

(c)

Figure 2.9 – Time responses obtained in phase 1 for a pressure = 400 Pa concerning: - the pressure *Δp(t)* at the input of the resonator (a); - the acoustic speed $v_{ac}(t)$ (b); - the transverse displacement *η (w, t)* of the jet (c)

Figure 2.10, for Example 1, and Figure 2.11, for Example 2, show the time responses obtained during phase 3:

- *(a)* the pressure P_m^e (in blue) and the pressure *Δp(t)* at the input of the resonator (in green);

- *(b)* speed U_j^e (in blue) and acoustic speed $v_{ac}(t)$ (in green);

- *(c)* transverse displacements $\eta_0(t)$ (in blue), $\eta_0(t-\tau)$ (in green) and $\eta(w,t)$ (in red);
- *(d)* pressures *Δp(t)* (**in black**), $\Delta p_{src}(t)$ (in red) and $\Delta p_{los}(t)$ (in blue).

The observation of these responses leads to the following remarks:

- Figures 2.10.a and 2.11.a: the pressure $\Delta p(t)$ (in green) at the input of the resonator (relation (2.11)), which oscillates around 0, has a low amplitude compared to the pressure P_m^e (in blue);

- Figures 2.10.b and 2.11.b: at the level of the channel output at $x = 0$, same remark for the acoustic speed $v_{ac}(t)$ (in green) which oscillates around 0 and has a low amplitude compared to flow velocity U_j^e (in blue);

- Figures 2.10.c and 2.11.c: the instability of the jet (which results in an amplification of its transverse displacement $\eta(x,t)$ (relation (2.4)) appears clearly by comparing the amplitudes of $\eta(x=w,t)$ (in red) and $\eta(x=0,t-\tau) = \eta_0(t-\tau)$ (in green);

- Figures 2.10.d and 2.11.d: the pressure $\Delta p_{los}(t)$ (in blue) linked to the loss of energy at the level of the bevel (relation (2.10)) remains low compared to the pressure $\Delta p(t)$ (**in black**) at the input of the resonator (relation (2.11)).

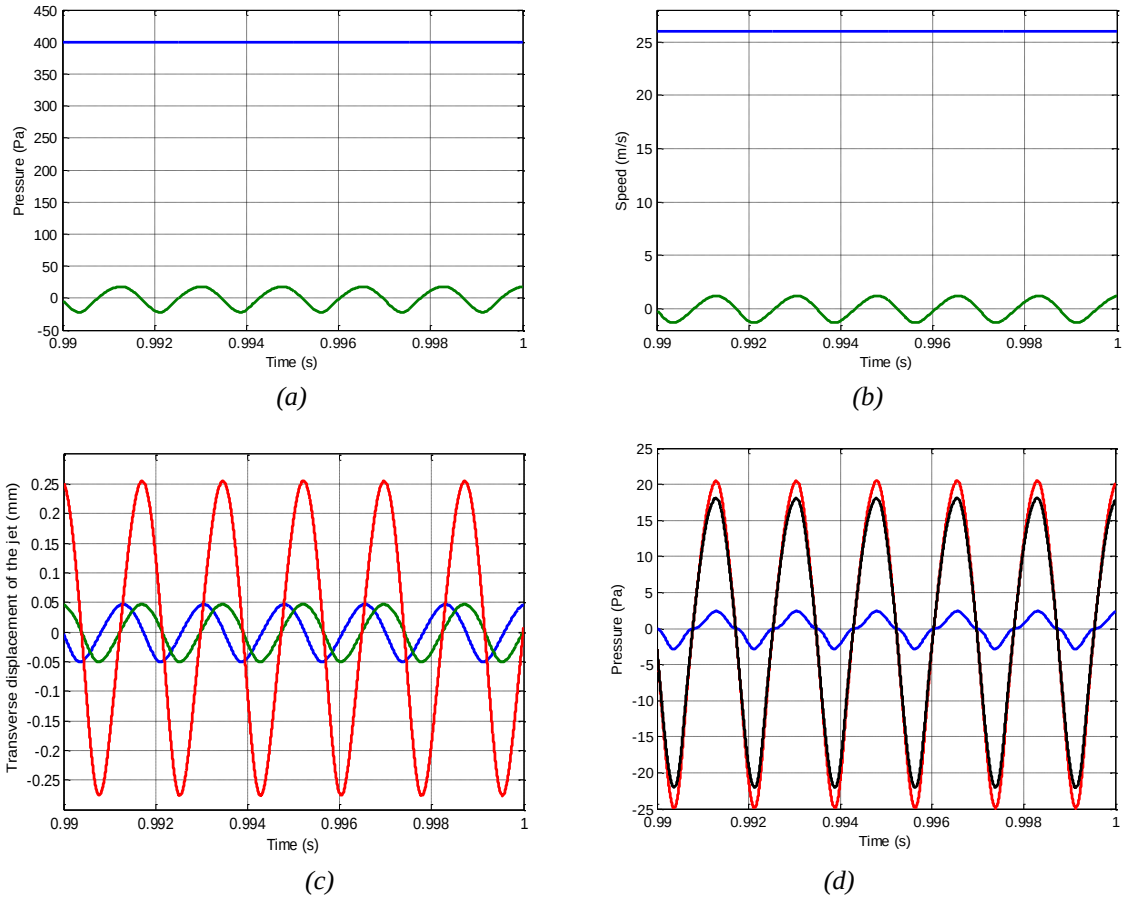

Figure 2.10 – Time responses obtained for a pressure = 400 Pa: (a) pressure (in blue) and pressure $\Delta p(t)$ at the input of the resonator (in green); (b) speed (in blue) and acoustic speed $v_{ac}(t)$ (in green); (c)

transverse displacements $\eta_0(t)$ (in blue), $\eta_0(t-\tau)$ (in green) and $\eta(w,t)$ (in red) (d) pressures $\Delta p(t)$ (in black), $\Delta p_{src}(t)$ (in red) and $\Delta p_{los}(t)$ (in blue)

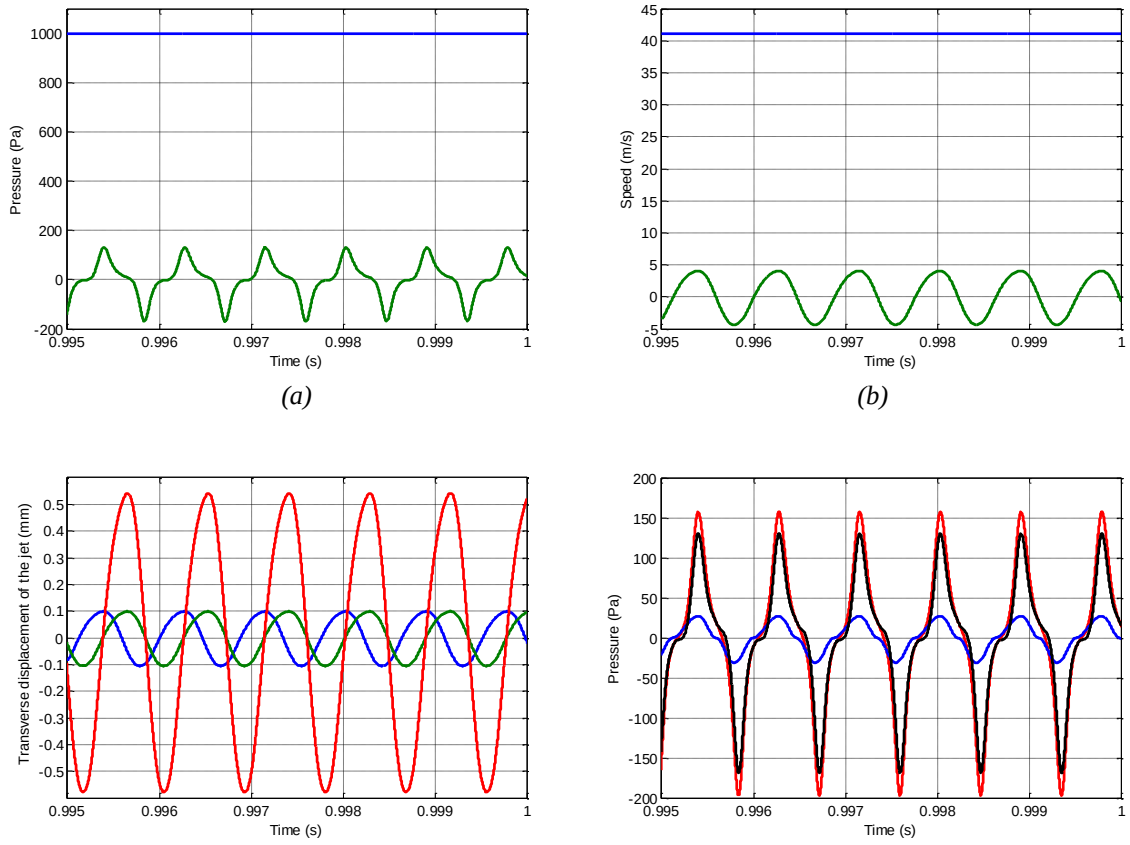

Figure 2.11 – Time responses obtained for a pressure = 1000 Pa
(a) pressure (in blue) and pressure $\Delta p(t)$ at the input of the resonator (in green);
(b) speed (in blue) and acoustic speed $v_{ac}(t)$ (in green);
(c) transverse displacements $\eta_0(t)$ (in blue), $\eta_0(t-\tau)$ (in green) and $\eta(w,t)$ (in red)
(d) pressures $\Delta p(t)$ (in black), $\Delta p_{src}(t)$ (in red) and $\Delta p_{los}(t)$ (in blue)

2.4 – Linearized Models

In order to facilitate the analysis of ***phase 1*** (start of the simulation) and ***phase 3*** (self-oscillation conditions), a linearization is developed leading to two linearized models, one for the analysis of the ***phase 1***, the other for that of ***phase 3***. Note that in ***phase 3***, that is to say for time $t >> \tau_c = 1/\omega_c = 3.18 \times 10^{-6}$ *s* (time constant of the low pass filter, see ***Remark 2.1***) the two linearized models exhibit the same behavior.

Thus, the observation of the simulations presented in the previous paragraph allows us to affirm that the variations of $\eta(w,t)$, $v_{ac}(t)$ and $\Delta p(t)$ are indeed around zero. This is the reason why the linearization of the system of equations (2.12) is done around this value.

More precisely, a first non-linearity appears in expression (2.8) of $\Delta p_{src}(t)$ with the function *tanh(.)* and a second non-linearity appears in expression (2.10) of $\Delta p_{los}(t)$ with the acoustic

speed $v_{ac}(t)$ squared. The expansion limited to the first order of the function *tanh(.)* around $\eta = 0$ leads to:

$$\tanh\left(\frac{\eta(w,t)-x_0}{b}\right)\Bigg|_{\eta=0} \approx \tanh\left(-\frac{x_0}{b}\right)+\left(\frac{1-\left(\tanh\left(-\frac{x_0}{b}\right)\right)^2}{b}\right)\eta(w,t)\ , \qquad (2.17)$$

form relation

$$\tanh\left(\frac{\eta(w,t)-x_0}{b}\right)\Bigg|_{\eta=0} \approx c_0 + c_1\,\eta(w,t)\ , \qquad (2.18)$$

taking

$$\begin{cases} c_0 = \tanh\left(-\frac{x_0}{b}\right) \\ c_1 = \dfrac{1-\left(\tanh\left(-\frac{x_0}{b}\right)\right)^2}{b} \end{cases}, \qquad (2.19)$$

c_0 and c_1 being constants.

As for the first-order limited expansion of $[v_{ac}(t)]^2$ around 0, its expression is given by:

$$\left[v_{ac}(t)\right]^2\Big|_{v_{ac}=0} \approx 0 + 2\times 0\times v_{ac}(t) \approx 0\ . \qquad (2.20)$$

From these developments limited to the first order, two linear models are proposed:

- a consideration in the time domain of the derivation operator *d/dt*, called the ***theoretical linearized model;***
- the other considering in the operational field the derivative operator *D(s)*, called the ***programmed linearized model.***

2.4.1 – Theoretical Linearized Model

The derivative with respect to time of relation (2.17) gives:

$$\frac{d}{dt}\left[\tanh\left(\frac{\eta(w,t)-x_0}{b}\right)\right] \approx \left(\frac{1-\left(\tanh\left(-\frac{x_0}{b}\right)\right)^2}{b}\right)\frac{d}{dt}\eta(w,t)\ . \qquad (2.21)$$

Thus, the expression (2.8) of $\Delta p_{src}(t)$ linearized around 0 is given by:

$$\Delta p_{src}(t) \approx \left(\frac{\rho\ \delta_d\ b\, U_j^e}{w} \right) \left(\frac{1 - \left(\tanh\left(-\frac{x_0}{b} \right) \right)^2}{b} \right) \frac{d}{dt}\eta(w,t)\ , \tag{2.22}$$

or again, after simplification by *b*,

$$\Delta p_{src}(t) \approx K_1\ \frac{d}{dt}\eta(w,t)\ , \tag{2.23}$$

taking,

$$K_1 = \frac{\delta_d}{w}\rho \left(1 - \left(\tanh\left(-\frac{x_0}{b} \right) \right)^2 \right) U_j^e\ , \tag{2.24}$$

K_1 being a constant.

Finally, the linearization of the system of equations (2.12) around 0 leads to:

$$\begin{cases} \eta(w,t) = K_0\ \ v_{ac}(t-\tau) \\ \Delta p(t) \approx K_1\ \ \frac{d}{dt}\eta(w,t) \\ v_{ac}(t) = \frac{1}{S}\ \ \mathrm{TL}^{-1}\left\{ Y_{in}(s,L)\ \ \Delta P(s) \right\} \end{cases}, \tag{2.25}$$

where $K_0 = h \exp(\alpha_i\ w) / U_j^e$ is a constant. The Laplace transform of the system (2.25), under the assumption of zero initial conditions, is then given by:

$$\begin{cases} \bar{\eta}(w,s) = K_0\ e^{-\tau s}\ V_{ac}(s) \\ \Delta P(s) = K_1\ s\ \bar{\eta}(w,s) \\ V_{ac}(s) = \frac{1}{S}\ \ Y_{in}(s,L)\ \ \Delta P(s) \end{cases}, \tag{2.26}$$

where $\bar{\eta}(w,s) = \mathrm{TL}\left\{ \eta(w,t) \right\}$.

This ***theoretical linearized model*** is used in section 2.5 for the analysis of the auto-oscillation conditions (***phase 3***).

2.4.2 Programmed Linearized Model

As specified in paragraph **2.3.1 - Numerical conditioning problem**, the solution adopted to solve the causality problem lies in the use of a derivation operator *D(s)* as defined by the relation (2.14) with n_h = 2 and $\omega_c = 2\pi$ 50 000 rad/s. Thus, the application in the symbolic domain of this derivation operator *D(s)* to relation (2.17) leads to an expression of the pressure *ΔP(s)*of the form:

$$\Delta P(s) = K_1^* \, D(s) \left(\frac{c_0}{s} + c_1 \, \bar{\eta}(w,s) \right) , \tag{2.27}$$

where $K_1^* = \dfrac{\rho \, \delta_d \, b}{w} U_j^e$ is a constant.

By distributing the operator *D(s)*, we show that the pressure *ΔP(s)* (relation (2.27)) is composed of the sum of two terms, *ΔP₀(s)* and *ΔP₁(s)*, that is:

$$\Delta P(s) = \Delta P_0(s) + \Delta P_1(s) , \tag{2.28}$$

taking,

$$\begin{cases} \Delta P_0(s) = D(s) \dfrac{C_0}{s} \\ \Delta P_1(s) = C_1 \, D(s) \, \bar{\eta}(w,s) \end{cases} , \tag{2.29}$$

with,

$$\begin{cases} C_0 = c_0 \, K_1^* = \left(c_0 \dfrac{\rho \, \delta_d \, b}{w} \right) U_j^e \\ C_1 = c_1 \, K_1^* = \left(c_1 \dfrac{\rho \, \delta_d \, b}{w} \right) U_j^e \end{cases} , \tag{2.30}$$

where it is important to note that the two constants C_0 and C_1 are proportional to the value of the stationary speed U_j^e and therefore (taking into account the relation (2.2)) to the value of the pressure P_m^e. Thus, $\Delta p_0(t) = TL^{-1}\{\Delta P_0(s)\}$ represents the step response of the operator *D(s)* to a step of amplitude C_0 (proportional to P_m^e), or again, to the extent that

$$\frac{D(s)}{s} = \frac{1}{\left(1 + \dfrac{s}{\omega_c} \right)^{n_h}} , \tag{2.31}$$

Δp₀(t) also represents the impulse response of the low-pass filter of order $n_h = 2$ multiplied by the constant C_0, that is

$$\Delta p_0(t) = C_0 \, TL^{-1} \left\{ \frac{1}{\left(1 + \dfrac{s}{\omega_c} \right)^{n_h}} \right\} = C_0 \, \frac{\omega_c^{n_h}}{(n_h - 1)!} \, t^{(n_h - 1)} \, e^{-\omega_c t} . \tag{2.32}$$

For a pressure P_m^e = 400 Pa and for the first moments of ***phase 1***, Figure 2.12 presents the time responses of the pressure *Δp₀(t)* obtained with the relation (2.32) (curve 1 in green), the nonlinear model (curve 2 in red) and the linearized model (curve 3 in blue).

Thus, in the first moments of ***phase 1*** where the variations are of low amplitude, the responses of the linearized model (curve 3 in blue) are identical to those of the nonlinear model (curve 2 in red). These answers clearly illustrate the legitimacy of the analysis made in the first

moments using the linearized model which leads to the analytical expression (2.32) of the pressure pulse (curve 1 in green).

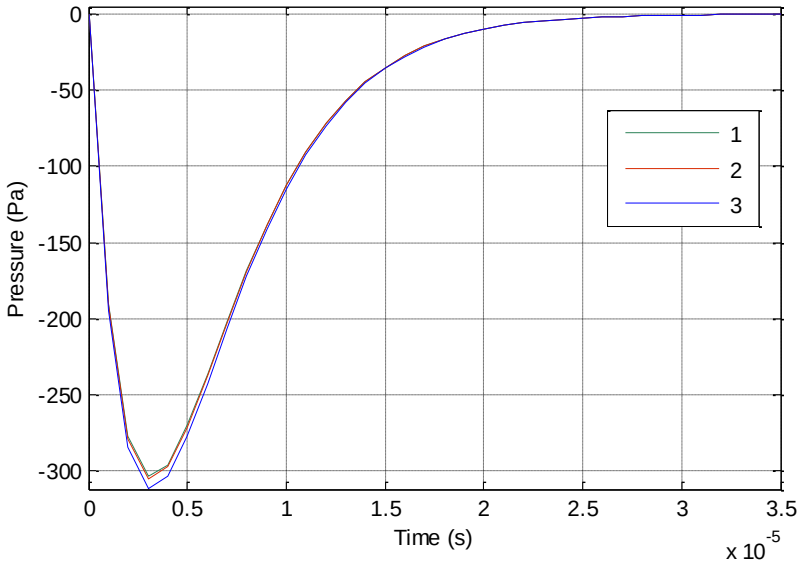

Figure 2.12 – For a pressure equal to 400 Pa and for the first moments of phase 1, time responses of the pressure $\Delta p_0(t)$ obtained with:
- relation (2.30) (curve 1 in green);
- the nonlinear model (curve 2 in red);
- the linearized model (curve 3 in blue)

Figure 2.13 presents the time responses obtained for a pressure $P_m^e = 400$ Pa with the linearized model (in blue) and the nonlinear model (in red) during the first instants of ***phase 1*** (start-up) over a time interval [0 ; 5] x10^{-5} s (left) and [0 ; 5] x 10^{-4} s (right), time responses of the pressure $\Delta p(t)$ at the input of the resonator ((a) and (b)), of the acoustic speed $v_{ac}(t)$ ((c) and (d)) and the transverse displacement $\eta(w,t)$ ((c) and (d)) at the level of the bevel at $x = w$.

Observation of these responses allows us to make the following remarks:

- the pressure pulse $\Delta p_0(t)$ as defined by relation (2.32) clearly appears from $t = 0$ s to $t = 3\text{x}10^{-5}$ s with a maximum amplitude of 310 Pa (Figure 2.13.a). This pressure pulse at the input of the resonator is at the origin of the appearance of the response of the acoustic speed $v_{ac}(t)$ (Figure 2.13.c) and of the transverse displacement $\eta(w,t)$ of the jet in $x = w$ (Figure 2.13.e);

- from $t = 3\text{x}10^{-5}$ s to $t = 4\text{x}10^{-4}$ s, the pressure $\Delta p_0(t)$ is zero (the pressure pulse is over, Figure 2.13.b), while the transient system of the acoustic speed $v_{ac}(t)$ (Figure 2.13.d) and the transverse displacement $\eta(w,t)$ is not finished (Figure 2.13.f);

- from $t = 4\text{x}10^{-4}$ s (value of the order of the delay $\tau = 0.4$ ms), under the effect of the looping of the system, a transient system associated with the pressure $\Delta p_0(t)$ appears (Figure 2.13 .b) leading to an additional transient system for the acoustic speed $v_{ac}(t)$ (Figure 2.13.d) and the

transverse displacement $\eta(w,t)$ (Figure 2.13.f), transient system which is superimposed on that still in course resulting from the initial pressure pulse.

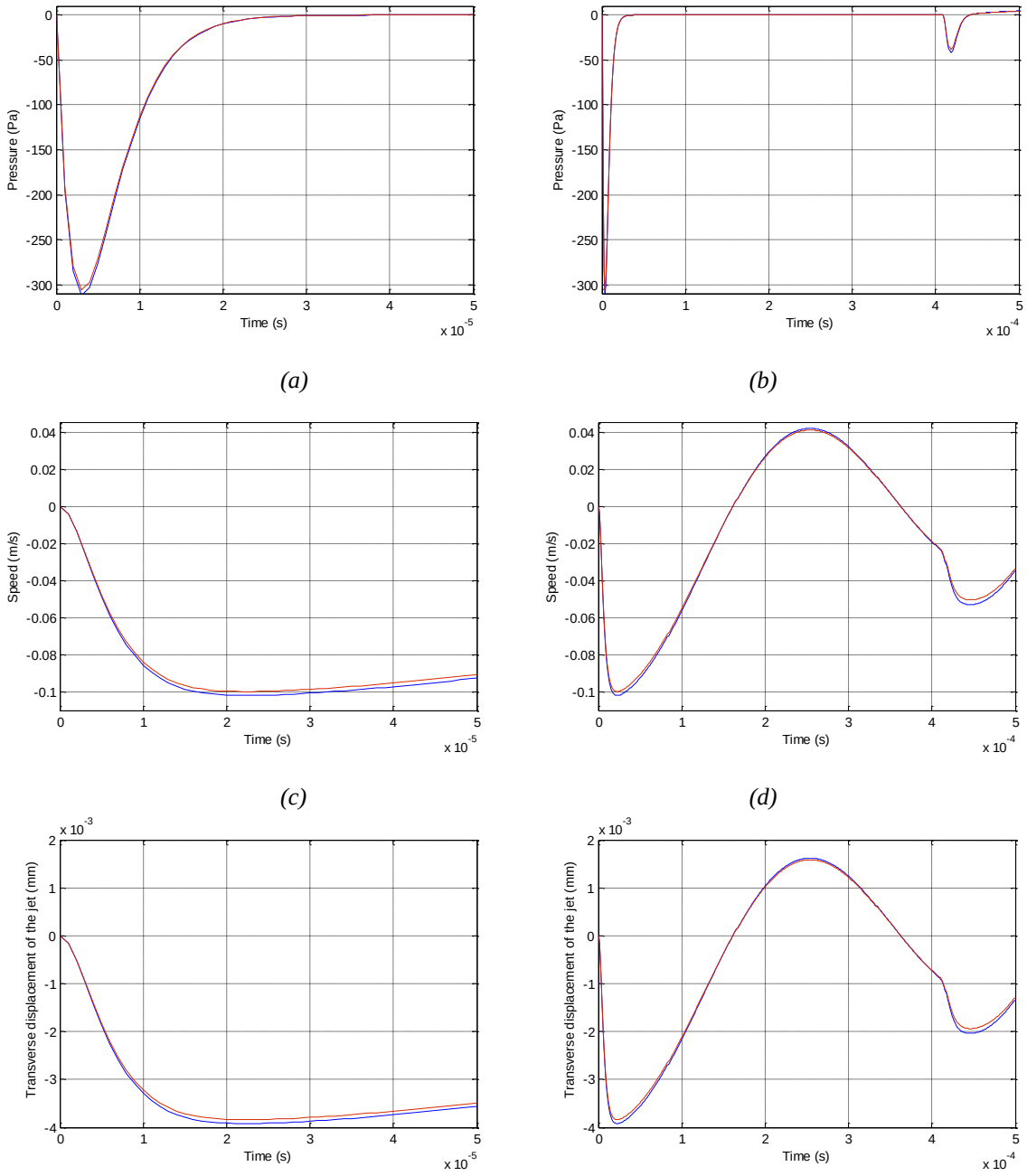

Figure 2.13- Time responses obtained for a pressure = 400 Pa with the linearized model (in blue) and the non-linear model (in red) during the first moments of phase 1 (start-up) over a time interval [0; 5]x10^{-5} sec (left) and [0; 5]x10^{-4} s (right):
- pressure $\Delta p(t)$ at the input of the resonator ((a) and (b));
- acoustic speed $v_{ac}(t)$ ((c) and (d));
- transverse displacement $\eta(w,t)$ ((c) and (d))

2.5 – Analysis of Auto-Oscillation Conditions

Figure 2.14 shows the variation in flow velocity U_j^e and the variation in frequency f_0 (in Hz) of ***phase 3*** self-oscillations as a function of pressure P_m^e. For constant pressures P_m^e included:

- between 400 Pa and 550 Pa, the average frequency f_0 of the self-oscillations is 569.6 Hz, lower value and close to the resonance frequency f_{r1} of the 1st mode of the resonator (Figure 2.6);
- between 600 Pa and 1000 Pa, the average frequency f_0 of the self-oscillations is 1130 Hz, a value also lower and close to the resonance frequency f_{r2} of the 2nd mode of the resonator (Figure 2.6).

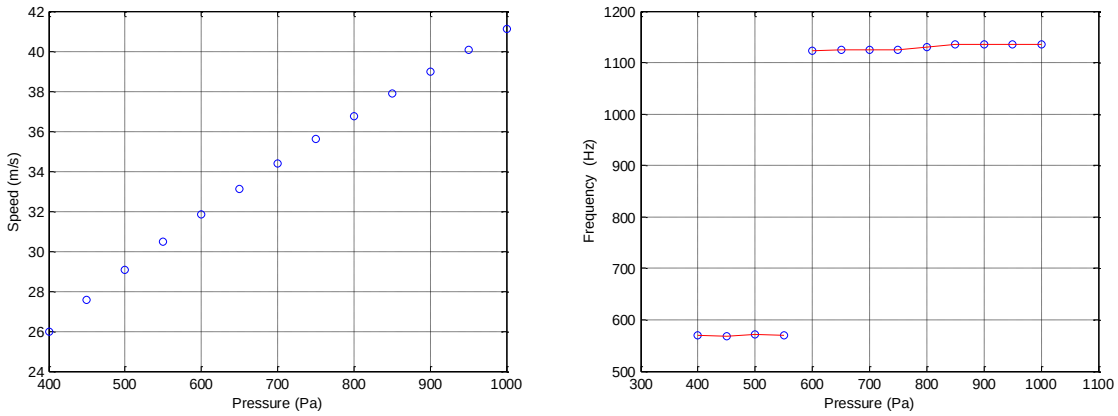

(a) *(b)*

Figure 2.14 - Variations in the flow speed of the jet at the outlet of the channel (a) and the frequency f_0 of the self-oscillations (b) as a function of the pressure

The remainder of this paragraph is devoted to the detailed analysis of the stationary periodic system present during ***phase 3***.

2.5.1 – Hydrodynamic Modes of the Jet and Acoustic Modes of the Resonator

The sound production mechanism is intricately tied to the interaction between the jet and the acoustic resonator (Terrien, 2015). Various playing modes arise depending on the hydrodynamic *k* and acoustic *i* modes at play. Just as the acoustic resonator exhibits multiple resonance modes, the jet can oscillate across different hydrodynamic modes, as illustrated in Figure 2.15.

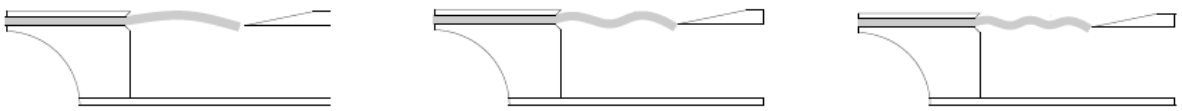

(a) *(b)* *(c)*

Figure 2.15 - Schematic representation of the different hydrodynamic modes of the jet: the first hydrodynamic mode k = 1 (a) corresponds to the case where one observes 1/2 wavelength between the outlet of the channel and the bevel; for the second k = 2 (b) and third k = 3 (c) hydrodynamic modes, we observe respectively 3/2 and 5/2 wavelengths over this same distance (see (Terrien, 2015))

The ***normal*** functioning of the instrument aligned with the coupling of an acoustic mode *i* with the first hydrodynamic mode k = 1 of the jet (M P Verge B. F., 1997). In this scenario, we observe we observe approximately half a hydrodynamic wavelength between the channel output and the bevel. The coupling of this hydrodynamic mode with each acoustic mode of the

resonator results in the various registers of the instrument. Therefore, the i^{th} register corresponds to the pairing of the hydrodynamic mode $k = 1$ of the jet with the i^{th} acoustic mode of the resonator. The manifestation of a particular register is tied to the selection of parameters under the control of the musician and configured by the instrument maker.

In specific instances, the coupling of an acoustic mode with a hydrodynamic mode of order k greater than 1 can be observed, resulting in the formation of a wind system (Kergomard & Chaigne, 2013) (Meissner, 2001) (Terrien, Vergez, & Fabre, 2013). For a wind system linked to the k^{th} hydrodynamic mode of the jet (with $k > 1$), $(2k - 1) / 2$ wavelength is observed along the jet (Figure 2.10). For the k^{th} hydrodynamic mode, this condition on the wavelength is defined as follows:

$$w = \frac{2k-1}{2}\lambda \ , \tag{2.33}$$

where λ represents the wavelength whose expression is generated by $\lambda = C_v^e \ T_0$, with $T_0 = 1/f_0$ the period of the self-oscillations. Considering the expression for the delay $\tau = w/C_v^e$ (relation 2.6), one can get:

$$C_v^e \ \tau = \frac{2k-1}{2} C_v^e \ T_0 \ , \tag{2.34}$$

or, simplifying by C_v^e,

$$\tau = \frac{2k-1}{2} T_0 \ . \tag{2.35}$$

Thus, for wind systems ($k > 1$), the delay τ is greater than the oscillation period T_0, while in ***normal*** operation ($k = 1$) $\tau < T_0$. In the musical context, wind systems are obtained for small values of the pressure $P_m(t)$.

2.5.2 – Self-Oscillation Conditions

The examination of the self-oscillation conditions within the looped system (Figure 2.5) provides insights into the mechanisms underlying the emergence of different types of systems (additional details can be found in (Terrien, Vergez, & Fabre, 2013)). Such a looped system can initiate self-oscillation if the frequency response $\beta(j\omega)$ of the open-loop transfer of the linearized system is equal to the unit. In other words, it should satisfy the two self-oscillation conditions outlined (Fletcher N. H., 1993):

- the modulus, $\beta_u = |\beta(j\omega_u)|$, is equal to 1, where ω_u being the pulsation at unity gain,
- the phase, $\phi_u = \arg[\beta(j\omega_u)]$, is zero or equal to a relative whole multiple n of 2π, $n \in Z$.

In steady harmonic system, the system of equations (2.26) becomes:

$$\begin{cases} \bar{\eta}(w, j\omega) = K_0\, e^{-\tau\, j\omega}\, V_{ac}(j\omega) \\ \Delta P(j\omega) \approx K_1\; j\omega\; \bar{\eta}(w, j\omega) \\ V_{ac}(j\omega) = \dfrac{1}{S}\; Y_{in}(j\omega, L)\; \Delta P(j\omega) \end{cases}, \tag{2.36}$$

from which we easily deduce the expression of $\beta(j\omega)$, that is:

$$\beta(j\omega) = \beta_0\; j\omega\; e^{-\tau j\omega}\, Y_{in}(j\omega, L)\;, \tag{2.37}$$

with β_0 a constant whose expression is given by:

$$\beta_0 = \frac{K_0\, K_1}{S} = \frac{h \exp(\alpha_i\, w)}{S\, U_j^e}\, \frac{\delta_d}{w}\, \rho \left(1 - \left(\tanh\left(-\frac{x_0}{b}\right)\right)^2\right) U_j^e\;, \tag{2.38}$$

or again, after simplification by U_j^e,

$$\beta_0 = \frac{h \exp(\alpha_i\, w)}{S}\, \frac{\delta_d}{w}\, \rho \left(1 - \left(\tanh\left(-\frac{x_0}{b}\right)\right)^2\right)\;. \tag{2.39}$$

The gain and the phase of $\beta(j\omega)$ therefore ultimately have the following expression:

$$\begin{cases} \beta(\omega) = \left|\beta(j\omega)\right| = \beta_0\; \omega \left|Y_{in}(j\omega, L)\right| \\ \phi(\omega) = \arg \beta(j\omega) = \dfrac{\pi}{2} - \tau\; \omega + \arg Y_{in}(j\omega, L) \end{cases}. \tag{2.40}$$

It is to highlight that:

- the gain $\beta(\omega)$ of the open loop does not depend on the flow speed U_j^e at the channel output and therefore on the pressure P_m^e at the mouthpiece input;
- the phase $\phi(\omega)$ of the open loop depends on the speed of flow U_j^e through the delay $\tau = \dfrac{w}{0.4\, U_j^e}$, the latter being as much greater as U_j^e is weak.

By illustration, Figure 2.16 shows the frequency responses of the gain $\beta(\omega)$ and of the phase $\phi(\omega)$ for Examples 1 (**in black**) and 2 (**in green**) defined in paragraph 2.3.

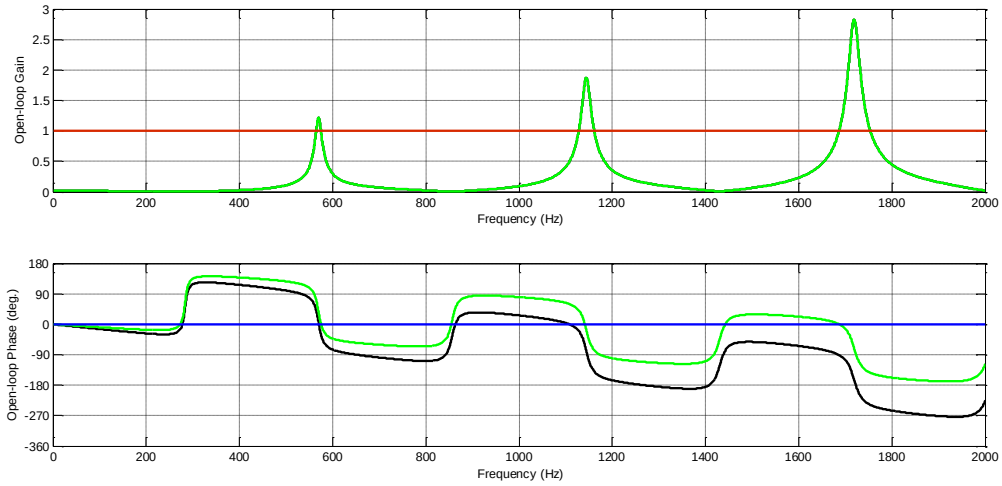

Figure 2.16 – Frequency responses of gain $\beta(\omega)$ and phase $\phi(\omega)$ for examples 1 (in black) and 2 (in green)

From a physical standpoint, the value of n is associated with the hydrodynamic mode of the jet. In fact, based on the relation concerning the phase $\phi(\omega)$ of the open loop as given in equation (2.40), we can verify retrospectively that for a given steady harmonic system, the self-oscillation threshold is situated at a frequency f_0 lower than the resonant frequency. Therefore, at $\omega_0 = 2\pi f_0$, it becomes possible to make the approximation. The self-oscillation condition on the phase of the open loop, namely $\arg Y_{in}\left(j\omega_0, L\right) \approx \pi/2$ then simplifies to:

$$\pi - \tau\,\omega_0 = n\,2\pi \ , \tag{2.41}$$

or again, knowing that $\omega_0 = 2\pi/T_0$,

$$1 - 2\frac{\tau}{T_0} = 2n \ , \tag{2.42}$$

finally:

$$\tau = \frac{1-2n}{2}\,T_0 \ . \tag{2.43}$$

By comparing Equations (2.35) and (2.43),

$$\frac{2k-1}{2}\,T_0 = \frac{1-2n}{2}\,T_0 \ , \tag{2.44}$$

Then,

$$n = 1 - k \ . \tag{2.45}$$

Hence, the value of n is directly linked to the hydrodynamic mode k of the jet. In typical operation ($n = 0$), the hydrodynamic mode is $k = 1$. All cases where $|n| > 1$ correspond to the wind systems necessarily obtained for low values of P_m^e and U_j^e, indicating large values of τ. Once the wind system can no longer be obtained, it becomes possible to examine the oscillation

conditions U_j^e for registers of higher orders (*i.e.*, for resonance modes of larger order). This progression moves from the first register to the second, then to the third, and so forth.

These findings align with experimental observations (Kergomard & Chaigne, 2013). In recorders, wind sounds were historically considered nonexistent, due to the low value of the *w/h* ratio (Kergomard & Chaigne, 2013). However, the development of an artificial mouth regulated in pressure (refer to Chapter 3) enables the demonstration of the emergence of these systems in recorders, particularly at low pressure P_m^e values not used by the musician in normal music playing conditions.

For the two examples of illustrations presented in this chapter, the observation of (Figure 2.16) makes it possible to affirm that the self-oscillation conditions in the two cases are obtained for $n = 0$ (normal operation), that is to say $\phi_u = 0$, which targets frequencies that satisfy the condition:

$$\arg Y_{in}\left(j\omega, L\right) + \frac{\pi}{2} = \tau\,\omega \ . \tag{2.46}$$

Graphically, the solution frequencies of this equality are located at the intersections between the phase of the input admittance $Y_{in}(j\omega,L)$ increased by $\pi/2$ and the phase lines $\tau\,\omega$ whose slopes τ depend on the speed flow U_j^e and therefore pressure P_m^e. Figure 2.17 shows the frequency responses of $\arg(Y_{in}(j\omega,L))+90°$ (in blue) and of $\tau\,\omega$ for examples 1 (P_m^e = 400 Pa, $U_j^e = 26$ m/s, **in black**) and 2 (P_m^e = 1000 Pa, $U_j^e = 41$ m/s, in green) defined in paragraph 2.3.

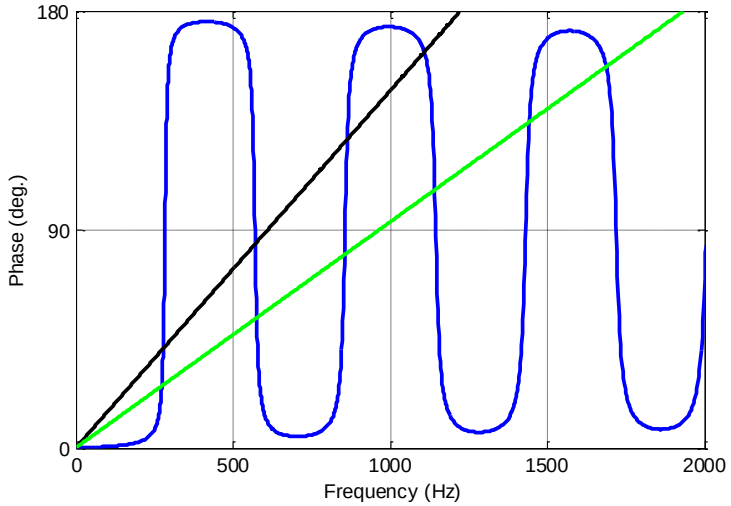

Figure 2.17 – Frequency responses of $arg Y_{in}\,(j\omega, L)$ + 90 ° (in blue) and of $\tau^*\omega$ for example 1 (P_m = 400 Pa, U_j = 26 m/s, in black) and example 2 (P_m = 1000 Pa, U_j = 41 m / s, in green) defined in paragraph 2.3

Taking into account the very low values of the damping factors of the input admittance $Y_{in}(j\omega,L)$ of the resonator (see Remark 2.2), the anti-resonance and resonance frequencies are easily identified in (Figure 2.17). They correspond to the intersection of the horizontal dotted line at 90°with the blue phase curve in the areas:
- positive slopes for the anti-resonance frequencies;
- negative slopes for the resonant frequencies.

Thus, still observing (Figure 2.17), it is interesting to note that the two intersections of the black line and the three intersections of the green line with the areas of positive slopes of the blue phase curve correspond to highly unstable operating points. (around anti-resonance frequencies) (Auvray R. , 2010). Conversely, the two intersections of the black line and the three intersections of the green line with the areas of negative slopes of the blue phase curve correspond to operating points where ranges of playing frequencies (registers) are accessible (around resonant frequencies).

This phase analysis must be completed by an analysis of the gain $\beta(\omega)$ of the open loop. If for a given playing frequency the latter is strictly greater than unity, then a perturbation $\eta(w,t)$ at the operational frequency is amplified. When this disturbance becomes too great, the non-linear phenomena (saturation of the *tanh(.)* function) provide the conditions for self-oscillation.

2.6 - Conclusion

The different elements of the sound production mechanism recalled in this chapter make it possible to capture the main phenomena observed, in particular, in recorder-type instruments. From the complete nonlinear model frequently used in the literature, a solution to improve its digital conditioning is proposed, allowing its programming using MatLab / Simulink. For the defined field of study, a detailed analysis of the simulated time responses highlights the presence of three phases during which the variations of the pressure at the inlet of the resonator, of the acoustic speed and of the lateral displacement of the air jet remain small around zero. The assumption of small variations being thus perfectly legitimate and realistic, two linearized models, one for the analysis of ***phase 1*** (start of the simulation), the other for that of ***phase 3*** (self-oscillations) are used to further understand the phenomena involved.

However, one should be aware of the limitations of this model when interpreting the results and comparing them with experimental data. This is the subject of Chapters 3 and 4.

Chapter 3- Design and Implementation of an Artificial Mouth for Wind Musical Instrument

3.1 – Introduction

Blowing machines, so-called artificial mouths, are used in musical acoustics when studying wind instruments, at least since 80 years (Ferrand & Vergez, 2008). As proposed in the literature review (Ferrand D. , Vergez, Fabre , & Blanc, 2010) (Takanishi, 2010) (Maki-Patola, 2004) (Hamilton, 2019) (Paine, 2013) (R. Saar, 2014) (V. Chatziioannou, 2008), the objective of controlling the pressure inside the artificial mouth is considered in many applications:

- to ensure quasi-static variation in order to analyze experimental bifurcation diagrams;
- to reproduce typical signals (Heaviside step function, sinus, ramps…) to compare the dynamics of the real instrument to the one obtained through numerical simulations;
- to mimic the time evolutions recorded on real musicians in order to analyse the strategies discovered over the years of practice.

The objective of this chapter is the study of visco-thermal losses in a wind musical instrument from a hardware-in-the-loop simulation platform. The hardware part of the platform is made up of an automatic blowing machine connected to the mouthpiece of a wind instrument (Abou Haidar, Abi Zeid Daou, & Moreau, 2019).

The software part of the platform is composed of resonator numerical model of the wind instrument including visco-thermal losses based on fractional model and the Control System (CS) used for regulating the pressure inside the artificial mouth. The first part of the project was the Computer Aided Design (CAD) of the platform. Thus, a digital simulator was developed with MatLab/Simulink software based on wind instruments artificial mouths found in several publications (Ferrand & Vergez, 2008) (Ferrand D. , Vergez, Fabre , & Blanc, 2010). The second part, presented in this chapter, is based on the realization of the test bench from the first part. The objective is to adjust the dynamic behavior of the numerical simulator to the real dynamic behaviour of test bench. The third and last part consists in modelling and analysing the visco-thermal losses present in the resonator of the wind instrument from fractional models (Andréa & Matignon , 1995).

3.2 – System Description

The test bench is presented in Figure 3.1. A servo-valve is connected to an air compressor through a pressure reducer. The maximum pressure available is around 6 bars, and the pressure reducer (with its manometer) is used to adjust the pressure P_1 upstream the servo-valve. The servo-valve is connected at the entrance of the artificial mouth itself whose internal volume V = 343 cm^3 is the place where the air pressure P_m must be controlled. The artificial mouth blows into the mouthpiece of a recorder flute. A MatLab/Simulink/LabVIEW program is used in order to control the air pressure P_m. Added to that, a flow meter, a temperature and a pressure transducers are used in order to characterize the behavior of the different parts of this system.

■ ***Remark***

For the rest of the chapter, the following notation is adopted for a variable X(t):

$$X(t) = X^e + x(t)\,, \tag{3.1}$$

where X^e is a constant value fixed by a given operating point and x(t) the fluctuation around X^e. Moreover, $\tilde{X}(t)$ represents a measurement of X(t) and $\hat{X}(t)$ an estimate of X(t).

Figure 3.2 presents the scheme of the experimental setup and Figure 3.3 the block diagram associated.

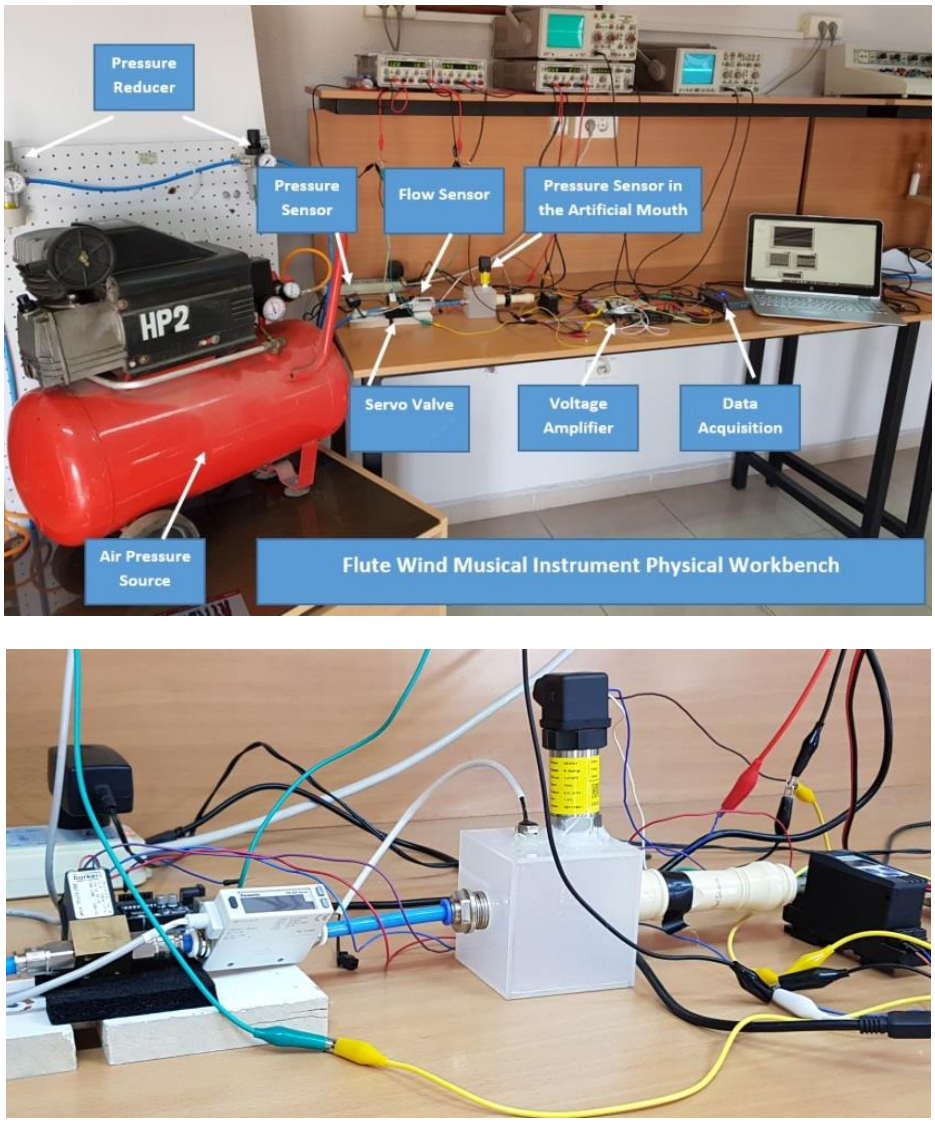

Figure 3.1 – Test bench photos

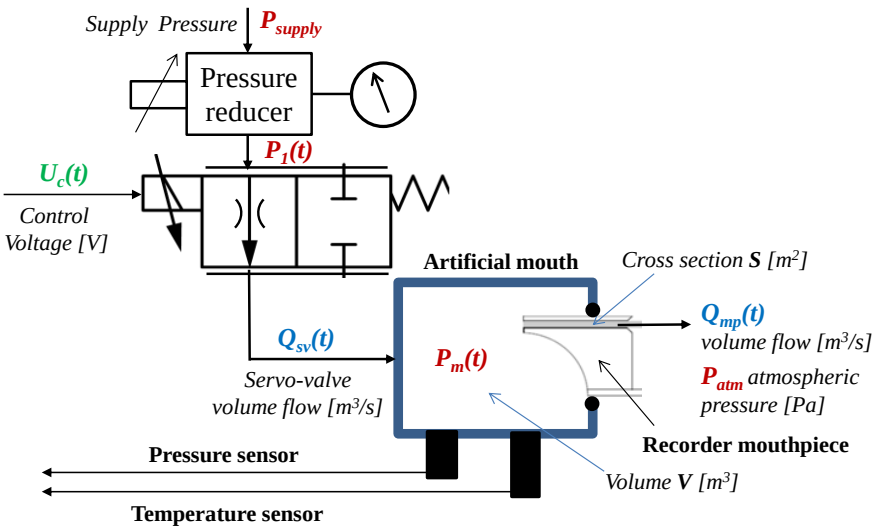

Figure 3.2 – Scheme of the experimental setup

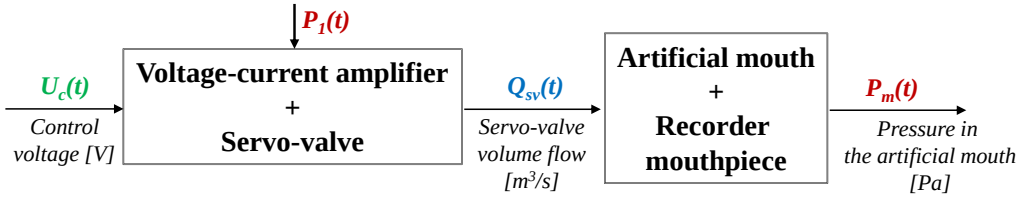

Figure 3.3 – Block diagram of the experimental setup

3.3 – Specifications for the Control

In the classical use of an artificial mouth, the pressure $P_m(t) = P_m^e + p_m(t)$ upstream the mouthpiece of the recorder flute (inside the artificial mouth) is tuned by hand through the pressure reducer and its manometer. When the compressed air is produced by a compressor such as that presented in Figure 3.1, the pressure $P_1(t) = P_1^e + p_1(t)$ upstream the servo-valve, fluctuates because the compressor tank being in need to be recharged once its pressure becomes below a certain level. This is the reason why it is difficult to manually control the pressure. Thus, the purpose of automatic pressure control inside the artificial mouth is to increase the accuracy by rejecting the pressure fluctuation $p_1(t)$ considered as a disturbance, while satisfying robust tracking of the reference pressure $P_{ref}(t)$ (Ferrand & Vergez, 2008). To recall, the final objective of this work project is the study of visco-thermal losses in a wind instrument based on fractional model. In order to facilitate the analysis of this complex problem, the reference pressure is chosen such as:

$$P_{ref}(t) = P_{ref}^e + p_{ref}(t) = P_{ref}^e + P_{ref}^0 \cos(2\pi f_0 t). \quad (3.2)$$

For all these reasons, the architecture of the control system presented in Figure 3.4 consists of a $P_{ref}(t)$ reference generator, a $U_{ff}(t)$ feedforward control and a $U_{fb}(t)$ feedback control, the robust controller of which is designed with the CRONE methodology (Oustaloup A. , 1995) (Oustaloup A. , 1991) (P. Lanusse, 2013) (Lanusse P. , 1994) (Lanusse P. , 2010).

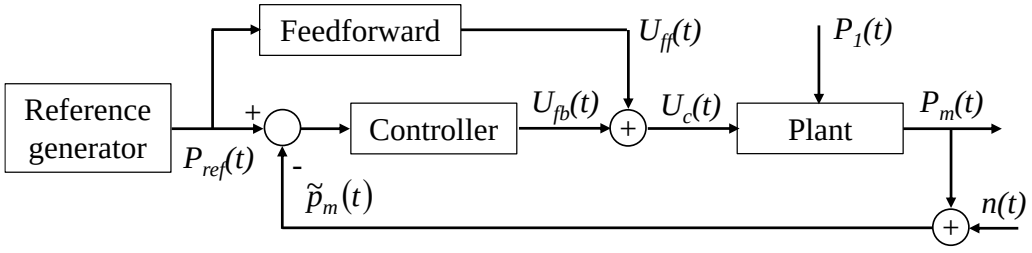

Figure 3.4 – Architecture of the Control System (CS)

3.4 – System Modelling and Validation

As presented in Figure 3.3, the experimental setup is divided into two parts:

- the first one consists of a voltage-current amplifier, a servo-valve connected to an air compressor via a pressure reducer. The inputs of this part are $P_1(t)$ the pressure upstream the servo-valve and $U_c(t) = U_{ff}(t) + U_{fb}(t)$ the control signal generated from MatLab/ Simulink/ LabVIEW, whereas the output is $Q_{sv}(t)$ the flow rate delivered by the servo-valve. This last device presents a nonlinear behavior;
- the second part is the artificial mouth and the mouthpiece of the recorder flute. The input of this part is $Q_{sv}(t)$ the flow rate from the servo-valve, whereas the output is $\tilde{P}_m(t)$ the pressure measured within the artificial mouth, $\tilde{P}_m(t) = P_m(t) + n(t)$ where $n(t)$ is the measurement noise.

3.4.1 – Modelling and Validation of the Servo-Valve

The servo-valve is designed by Bürkert firm (ref. Bürkert 2871). Based on previous works (Ferrand & Vergez, 2008) (Ferrand D. , Vergez, Fabre , & Blanc, 2010) (Abou Haidar., Abi Zeid Daou, & Moreau, 2018) (G. Abou Haidar, 2019), it has been shown that the servo-valve's behavior can be divided in two parts: a nonlinear static part and a linear dynamic part.

Figure 3.5 shows the block diagram of the servo-valve. In order to express the output of the nonlinear part, a static flow Q_{stat} is introduced.

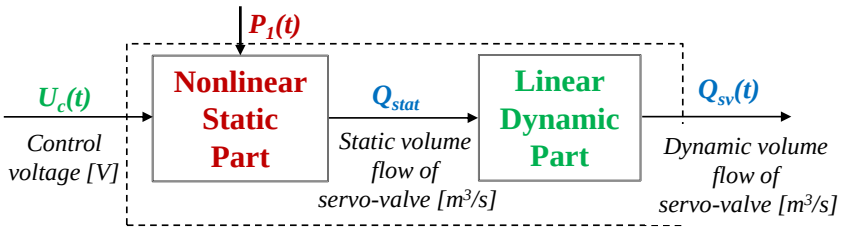

Figure 3.5 – Block diagram of the servo-valve

The linear dynamic part between Q_{stat} and $Q_{sv}(t)$ is represented by a second order transfer function $H_{sv}(s)$ with a unit static gain (Ferrand & Vergez, 2008) (Ferrand D. , Vergez, Fabre , & Blanc, 2010) (Abou Haidar., Abi Zeid Daou, & Moreau, 2018) (Abou Haidar, Abi Zeid Daou, & Moreau, 2019):

$$H_{sv}(s) = \frac{1}{1 + 2\zeta\, s/\omega_0 + (s/\omega_0)^2}\ , \tag{3.3}$$

where $\zeta = 0.3$ and $\omega_0 = 2\pi\ 240$ rad/s.

As already mentioned, the output flow rate $Q_{sv} = f(U_c, P_1)$ depends on the control voltage signal U_c (that may vary between 0 and 10V) and the pressure P_1 upstream the servo- (max[P_1] = 6 bar).

Figure 3.6 shows the static operating domain obtained from measurements for $U_c \in [0\,;10]\,\mathrm{V}$ and $P_1 \in [1\,;6]\,\mathrm{bar}$.

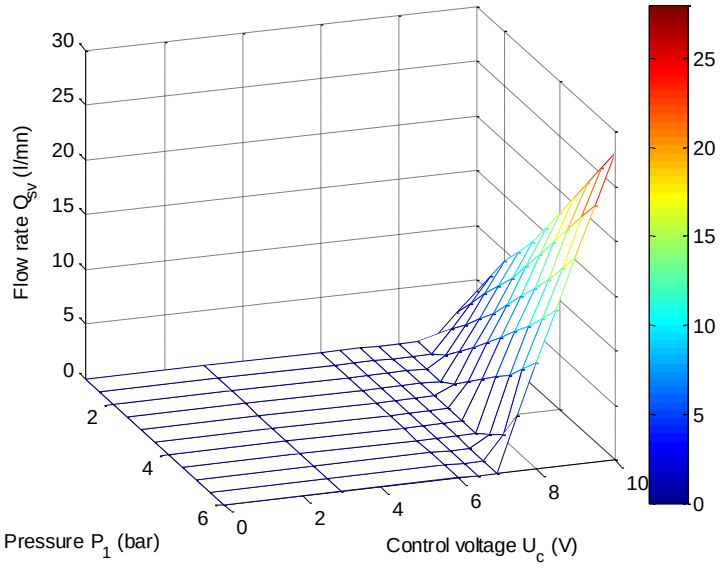

Figure 3.6 – Static operating domain obtained from measurements

We can see a dead zone where $Q_{sv} = 0$ whatever the value of $U_c \in [0\,;U_{\min}(P_1)]$, and a variation zone of Q_{sv} where the saturation, max[Q_{sv}], depends on max[U_c] = 10 V and max[P_1] = 6 bar. In the variation zone, for a given operating point O defined by $O \equiv (U_c^e\,;P_1^e)$, the flow rate $Q_{sv}(t, U_c, P_1)$ can be written as follow:

$$Q_{sv}(t,U_c,P_1) = Q_{sv}^e(U_c^e,P_1^e) + q_{sv}(t,U_c,P_1), \tag{3.4}$$

where

$$q_{sv}(t,U_c,P_1) = K_{qu}(U_c^e,P_1^e)\;u_c(t) + K_{qp}(U_c^e,P_1^e)\;p_1(t)\;, \tag{3.5}$$

and

$$K_{qu}(U_c^e,P_1^e) = \left.\frac{\partial Q_{sv}}{\partial u_c}\right|_{\substack{U_c^e \\ P_1^e}},\quad K_{qp}(U_c^e,P_1^e) = \left.\frac{\partial Q_{sv}}{\partial p_1}\right|_{\substack{U_c^e \\ P_1^e}}. \tag{3.6}$$

The estimated value $\hat{K}_{qu}$ of the static gain K_{qu} is obtained from:

$$\underset{[\mathrm{l.mn^{-1}.V^{-1}}]}{\hat{K}_{qu}(P_1)} = \frac{\Delta\tilde{Q}_{sv}}{\Delta U_c(P_1)} = \frac{\max[\tilde{Q}_{sv}(U_{\max},P_1)]-0}{\max[U_c]-U_{\min}(P_1)}, \tag{3.7}$$

with U_{max} = max[U_c] = 10 V.

Figure 3.7 shows the variation of $\hat{K}_{qu}$ versus $P_1 \in [1;6]$ bar that can be considered as linear and modelled by:

$$\underset{[\text{l.mn}^{-1}.\text{V}^{-1}]}{\hat{K}_{qu}(P_1)} = A \underset{[\text{bar}]}{P_1} + B\,, \tag{3.8}$$

with

$$\begin{cases} A = 0.99 \ \text{l.mn}^{-1}.\text{V}^{-1}.\text{bar}^{-1} \\ B = 3.4 \ \text{l.mn}^{-1}.\text{V}^{-1} \end{cases}. \tag{3.9}$$

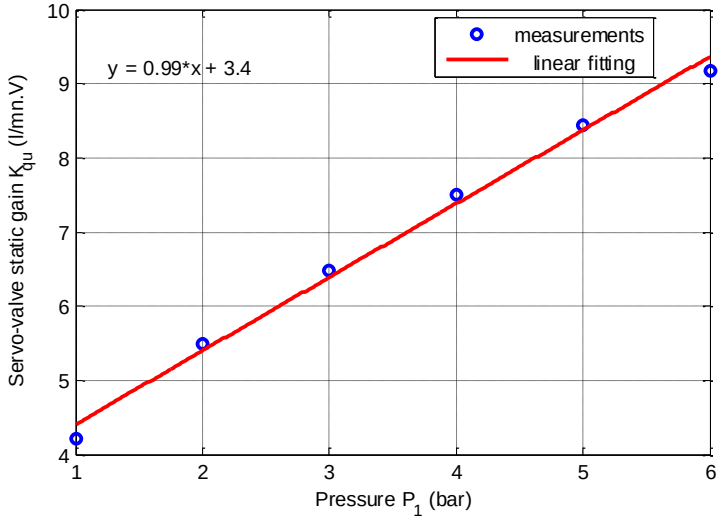

Figure 3.7 – Variation of $\hat{K}_{qu}$ versus $P_1 \in [1;6]bar$

The non-linear static part and the linear dynamic part of the servo-valve are integrated in a digital simulator programmed with MATLAB / Simulink.

3.4.2 – Choosing an Operating Point

The limits of the servo-valve operating domain being estimated, the choice of an operating point $O \equiv (U_c^e\,;\,P_1^e)$ and the amplitude of the variations around this point is essential in order to avoid the risks of saturation of the flow rate $Q_{sv}(t)$.

After observing the pressure $P_1(t)$ during numerous tests, the fluctuations $p_1(t)$ are considered to be limited between -1 and + 1bar. This is the reason why we chose $P_1^e = 5$ bar, and so $P_1 \in [4;6]$ bar. For this variation range of P_1, the variation range of U_c without saturation of Q_{sv} has as limits $U_{\min}(P_{1\min} = 4\text{bar}) = 7.55$ V and U_{max} = 10 V, so:

$$7.55 \text{ V} \le U_c(t) = U_{ff}(t) + U_{fb}(t) \le 10 \text{ V}\,, \tag{3.10}$$

with

$$U_{ff}(t) = U_c^e + U_c^0 \cos(2\pi\ f_0). \tag{3.11}$$

By choosing $U_c^e = 8.5$ V and $U_c^0 = 0.5$ V, the variation range of the feed-forward control signal U_{ff} is given by:

$$\begin{cases} \max\left[U_{ff}(t)\right] = U_c^e + U_c^0 = 9\ \text{V} \le U_{\max} = 10\ \text{V} \\ \min\left[U_{ff}(t)\right] = U_c^e - U_c^0 = 8\ \text{V} \ge U_{\min} = 7.55\ \text{V} \end{cases}, \tag{3.12}$$

and the variation range of the feedback control signal U_{fb} is given by:

$$\begin{cases} \max\left[U_{fb}(t)\right] = U_{\max} - \max\left[U_{ff}(t)\right] = +1\ \text{V} \\ \min\left[U_{fb}(t)\right] = U_{\min} - \min\left[U_{ff}(t)\right] = -0.45\ \text{V} \end{cases}. \tag{3.13}$$

Figure 3.8 shows the chosen operating point $O \equiv \left(U_c^e = 8.5\ \text{V}\ ;\ P_1^e = 5\ \text{bar}\right)$ and the linear static operating domain defined by $U_c \in [7.55\,;10]\,\text{V}$ and $P_1 \in [4\,;6]\,\text{bar}$.

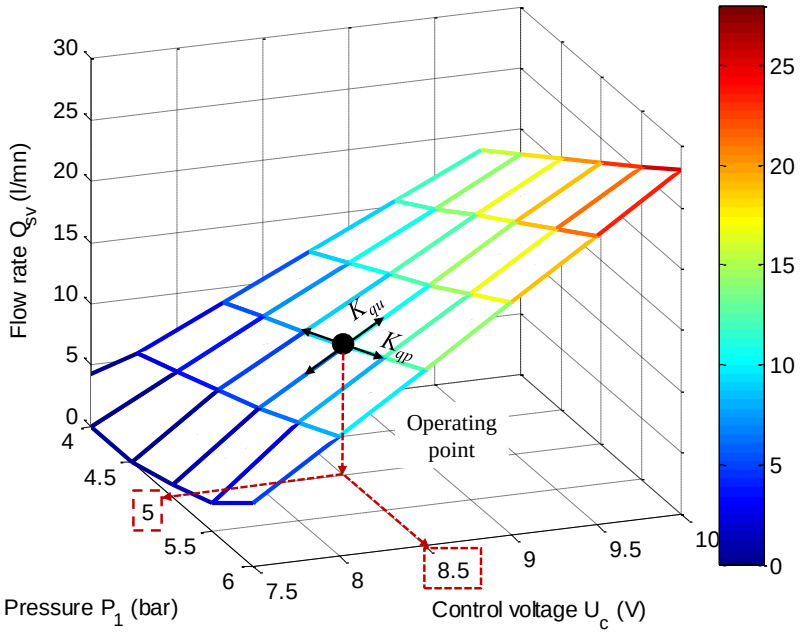

Figure 3.8 – Operating point *O* and linear static operating domain

3.4.3 – Modelling and Validation of the Artificial Mouth

The artificial mouth is implemented using a cubic box whose input is the flow rate $Q_{sv}(t)$ coming from the servo-valve and the output is the pressure $P_m(t)$ inside the box. The expression of the pressure $P_m(t)$ is given by the state equation of perfect gases:

$$P_m(t) = \frac{r\,T}{V}\,M(t), \tag{3.14}$$

where

- r = 287 J.kg^{-1}.K^{-1}, the thermodynamic constant of air;
- T =293.5°K, the temperature of air inside the box;
- $M(t)$ is the mass of the air inside the box of volume V. This value depends on the variation of the flow between the input (represented by $Q_{sv}(t)$) and the output (represented by $Q_{mp}(t)$). As small variations are considered, the air density ρ is considered to be constant. Thus, the expression of $M(t)$ is given by:

$$M(t) = \rho \int_0^t \left(Q_{sv}(\tau) - Q_{mp}(\tau)\right) d\tau + M(0), \tag{3.15}$$

where the expression of $Q_{mp}(t)$ is given by Bernoulli law (Ferrand D. , Vergez, Fabre , & Blanc, 2010):

$$Q_{mp}(t) = \alpha \sqrt{\Delta P_{mp}(t)} \ , \tag{3.16}$$

where α is a coefficient estimated from measurements and $\Delta P_{mp}(t) = P_m(t) - P_{atm}$ (P_{atm} is the relative atmospheric pressure which is zero by definition, so $\Delta P_{mp}(t) = P_m(t)$). By introducing in relation (3.15) the pressure $P_m(t)$ from relation (3.14), namely:

$$P_m(t) = \frac{\rho\, r\, T}{V} \int_0^t \left(Q_{sv}(\tau) - Q_{mp}(\tau)\right) d\tau + \frac{r\, T}{V} M(0), \tag{3.17}$$

we obtain

$$P_m(t) = \frac{1}{C_{am}} \int_0^t \left(Q_{sv}(\tau) - Q_{mp}(\tau)\right) d\tau + P_m(0), \tag{3.18}$$

where C_{am} is the pneumatic capacity associated with the volume V of the artificial mouth given by:

$$C_{am} = \frac{V}{\rho\, r\, T} \ , \tag{3.19}$$

and $P_m(0)$ the initial value of the pressure $P_m(t)$ given by

$$P_m(0) = \frac{r\, T}{V} M(0) \ . \tag{3.20}$$

It is important to note that in static $Q_{mp}^e = Q_{sv}^e$, and for a quasi-static variation $Q_{mp}(t) \approx Q_{sv}(t)$.

Figure 3.9 shows the plot of $Q_{sv}(t)$ versus $P_m(t)^{0.5}$ for a quasi-static variation. The linear fitting (in red) of the measurements (x) leads to an estimate $\hat{\alpha}$ given by:

$$\hat{\alpha} = 1.1 \ \text{l.mn}^{-1}.\text{Pa}^{-0.5} = 18.3310^{-6} \ \text{m}^3.\text{s}^{-1}.\text{Pa}^{-0.5}. \tag{3.21}$$

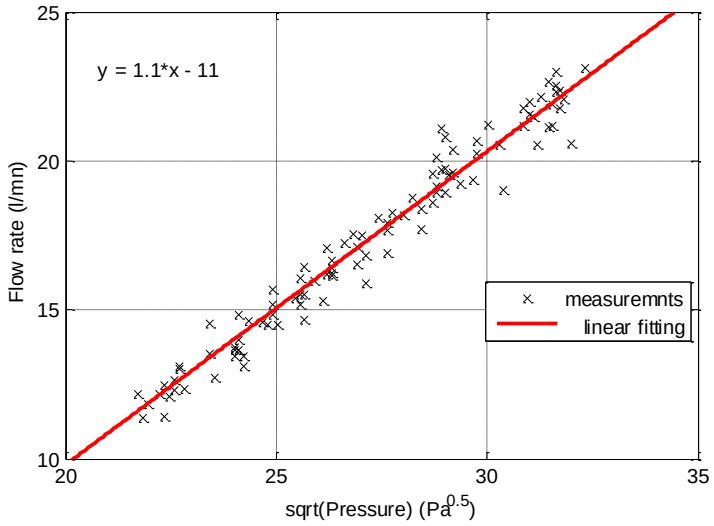

Figure 3.9 - Plot of $Q_{sv}(t)$ vs $sqrt(P_m(t))$ for a quasi-static variation

From relations (3.16), (3.17) and (3.20), the behavior of the artificial mouth is integrated in the digital simulator programmed with MATLAB / Simulink.

3.4.4 – Linearized Model of the Plant

In order to design the CRONE controller in frequency domain, a linearized model of the plant is derived around the operating point *O*. Thus, the pressure $P_m(t)$ and the flow rate $Q_{mp}(t)$ can be expressed as follows:

$$\begin{cases} P_m(t) = P_m^e + p_m(t) \\ Q_{mp}(t) = Q_{mp}^e + q_{mp}(t) \end{cases}, \tag{3.22}$$

where
$$Q_{mp}^e = \alpha \sqrt{P_m^e} \quad \text{and} \quad q_{mp}(t) = \frac{1}{R_{mp}}\, p_m(t), \tag{3.23}$$

with
$$\frac{1}{R_{mp}} = \left.\frac{\partial Q_{mp}}{\partial P_m}\right|_{P_m = P_m^e} = \frac{\alpha}{2\sqrt{P_m^e}}\ . \tag{3.24}$$

Figure 3.10 shows the block diagram of the artificial mouth linearized model.

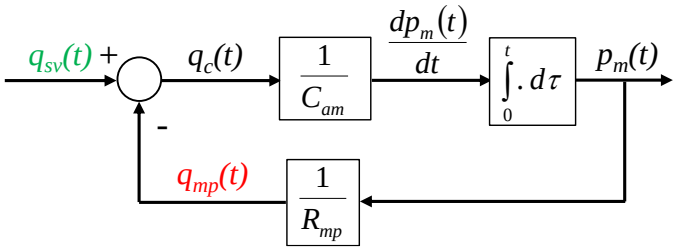

Figure 3.10 – Block diagram of the artificial mouth linearized model

The transfer function $H_1(s)$ between $\overline{P}_m(s) = \mathrm{LT}\{p_m(t)\}$ and $\overline{Q}_{sv}(s) = \mathrm{LT}\{q_{sv}(t)\}$, where LT represents Laplace Transform, is given by:

$$H_1(s) = \frac{\overline{P}_m(s)}{\overline{Q}_{sv}(s)} = \frac{R_{mp}}{1 + R_{mp}\, C_{am}\, s} = \frac{H_0}{1 + s/\omega_1}, \tag{3.25}$$

where $$H_0 = R_{mp}\ ,\ \tau_1 = R_{mp}\, C_{am} \ \text{ and } \ \omega_1 = 1/\tau_1 . \tag{3.26}$$

Finally, the complete linearized model used for the design of the control law is represented by the transfer function $G(s,P_1)$ between $\overline{P}_m(s)$ and $\overline{U}_c(s)$ as follow:

$$G(s, P_1) = \frac{G_0(P_1)}{\left(1 + 2\zeta\ s/\omega_0 + (s/\omega_0)^2\right)(1 + s/\omega_1)}\ , \tag{3.27}$$

where

$$G_0(P_1) = K_{qu}(P_1)\, H_0. \tag{3.28}$$

For the design of the robust control law, the main parameter's values used are:

$$\begin{cases} P_1 \in [4\,;6]\,\text{bar}\,;\, P_m^e = 750\ \text{Pa} \\ K_{qu} \in [12.27\,;15.57]\,10^{-5}\,\text{m}^3\text{s}^{-1}\text{V}^{-1} \\ \hat{R}_{bec} = 2.65\,10^6\ \text{Pa s m}^{-3}\,;\, C_{am} = 3.38\,10^{-9}\ \text{Pa m}^{-3} \\ G_0 \in [325\,;412.5]\,\text{Pa V}^{-1}\,;\, \omega_1 = 2\pi\ 17.8\ \text{rad/s} \end{cases}\ , \tag{3.29}$$

and three transfer functions are defined for the minimum (4 bar), the nominal (5 bar) and the maximum (6 bar) cases:

$$G_{min}(s, 4\,\text{bar})\ ,\ G_{nom}(s, 5\,\text{bar})\ ,\ G_{max}(s, 6\,\text{bar})\ . \tag{3.30}$$

Figure 3.11 presents the Bode plots of $G(j\omega)$ for three values of the pressure: P_1 = 4 bar (in blue), P_1 = 5 bar (in black) and P_1 = 6 bar (in red).

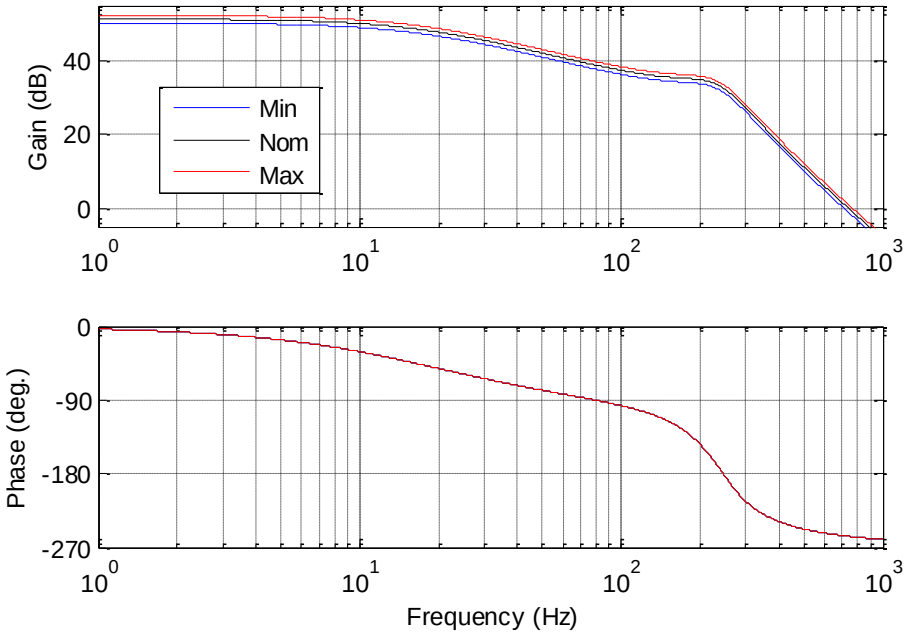

Figure 3.11 – Bode plots of $G(j\omega)$ for three values of the pressure: P_1= 4 bar (in blue), P_1 =5 bar (in black), P_1 =6 bar (in red)

3.5 – Controller Design

The feedforward part is based on the nominal inverse static gain of the linearized model ($G_{0\_nom} = G_0$(5 bar)) used for the design of the feedback control law, namely:

$$U_{ff}(t) = G_{0\_nom}^{-1}\, P_{ref}(t) \quad . \tag{3.31}$$

3.5.1 – User Specifications

The user specifications of the control system defined from a preliminary work (Ferrand & Vergez, 2008) (Lanusse P. , 1994) are the following:

- a phase margin $M_{Ø} > 40°$;
- an open-loop gain crossover frequency $\omega_u \geq 2\pi$ 10 rad/s;
- a steady-state error equal to 0;
- a variation range of U_{fb} given by $-0.45\ \text{V} \leq U_{fb} \leq 1\ \text{V}$.

3.5.2 – CRONE Control-System Design (CSD) Methodology

The CRONE CSD methodology is a frequency-domain approach developed since the eighties (Oustaloup A. , 1995) (Oustaloup A. , 1991) (Lanusse P. , 1994). It is based on the common unity-feedback configuration presented in Figure 4. Three CRONE CSD methods have been developed, each one of them denotes a generation of CRONE design. The general form of the nominal open-loop transfer function β_{nom}(s) of the second generation CRONE control is defined by:

$$\beta_{nom}(s) = \beta_0 \left(\frac{1 + s/\omega_l}{s/\omega_l} \right)^{n_l} \left(\frac{1 + s/\omega_h}{1 + s/\omega_l} \right)^{n} (1 + s/\omega_h)^{-n_h} \ . \tag{3.32}$$

The first part of the above equation (3.32) represents the behavior at low frequencies with an integer order n_l, the second represents the behavior at middle frequencies with non-integer order n varying between 1 and 2 around ω_u, and the last represents the behavior at high frequencies with an integer order n_h. As for the gain β_0, it is defined by (Lanusse P. , 1994):

$$\beta_0 = (\omega_u/\omega_l)^{n_l} \left(1 + (\omega_u/\omega_l)^2\right)^{(n-n_l)/2} \left(1 + (\omega_u/\omega_h)^2\right)^{(n_h-n)/2} . \tag{3.33}$$

With $M_{Ø}$ = 45°, ω_u = 2π10 rad/s, $G_0 \in [325; 412.5]$ Pa/V and in accordance with the methodology described in (Oustaloup A. , 1991), the parameter's values of the open-loop transfer function are:

$$\begin{cases} n_l = 2 \, , \, n = 1.5 \, , \, n_h = 2 \\ \omega_l = 5.79 \text{ rad/s} \, , \, \omega_h = 20\,444 \text{ rad/s} \, , \, \beta_0 = 32.92 \text{ SI} \end{cases} . \tag{3.34}$$

When the nominal open-loop transfer is determined, the fractional controller $C_F(s)$ is defined by its frequency response:

$$C_F(j\omega) = \beta_{nom}(j\omega) / G_{nom}(j\omega) \, . \tag{3.35}$$

The synthesis of the ideal frequency response $C_F(j\omega)$ consists of identifying a rational frequency response $C_R(j\omega)$ given by:

$$C_R(j\omega) = B(j\omega) / A(j\omega) \, , \tag{3.36}$$

where $B(j\omega)$ and $A(j\omega)$ are polynomials of specified integer degrees n_B and n_A. All the frequency-domain system identification techniques can be used (Oustaloup A. , 1991). Figure 3.12 presents the Bode plot of the controller $C_R(j\omega)$.

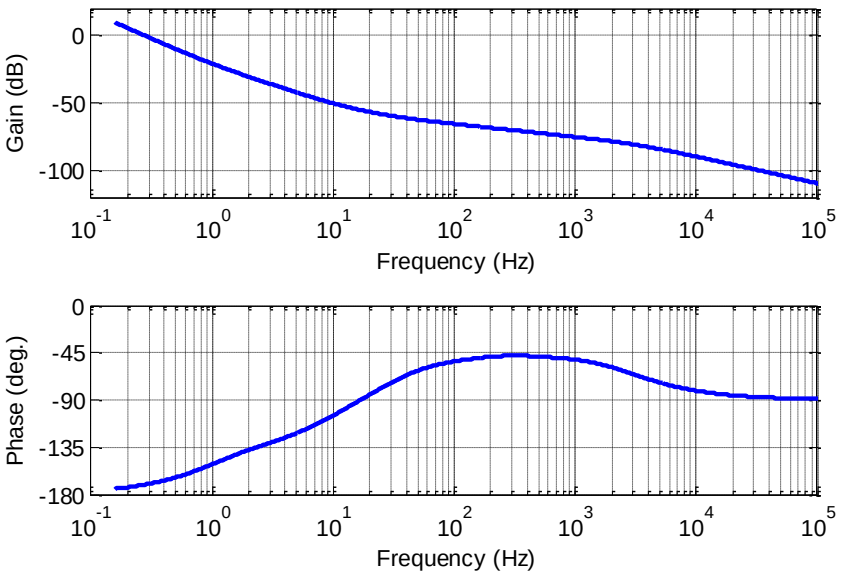

Figure 3.12 – Bode plot of $C_R(j\omega)$

3.6 – System Performance

3.6.1 – Frequency Domain

Figure 3.13 presents the Bode plots (a) and the Nichols loci (b) of the open-loop transfer function $\beta(j\omega)$ and Figure 3.14 the Bode plots of complementary sensitivity function $T(j\omega)$ (a), of sensitivity function $S(j\omega)$ (b), of control effort sensitivity function $CS(j\omega)$ (c) and of plant input sensitivity function $GS(j\omega)$ (d) obtained with the CRONE controller for the three cases (min, nom, max).

As one can observe, the phase margin $M_\emptyset$ (Figure 3.13.b) and the resonant peaks Q_T of $T(j\omega)$ (Figure 3.14.a) and Q_S of $S(j\omega)$ (Figure 3.14.b) remain constant for all the cases thus showing the robustness of stability degree (Oustaloup A. , 1991).

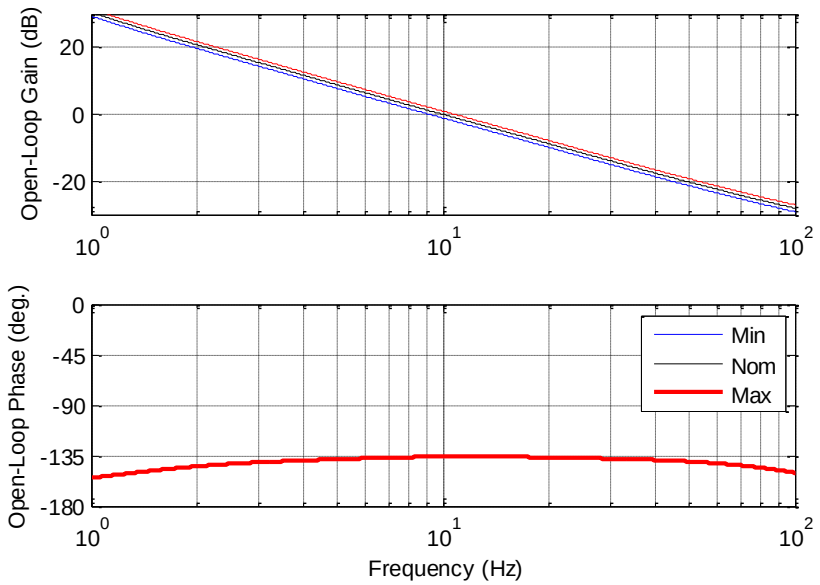

(a)

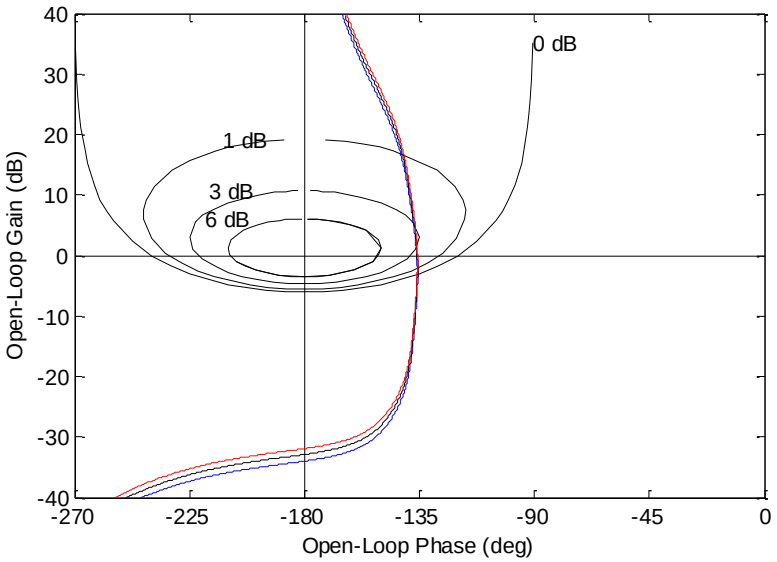

(b)

Figure 3.13 – Bode plots (a) and Nichols loci (b) of $\beta(j\omega)$ obtained with the CRONE controller for the three cases: min (4 bar in blue), nom (5 bar in black) and max (6 bar in red)

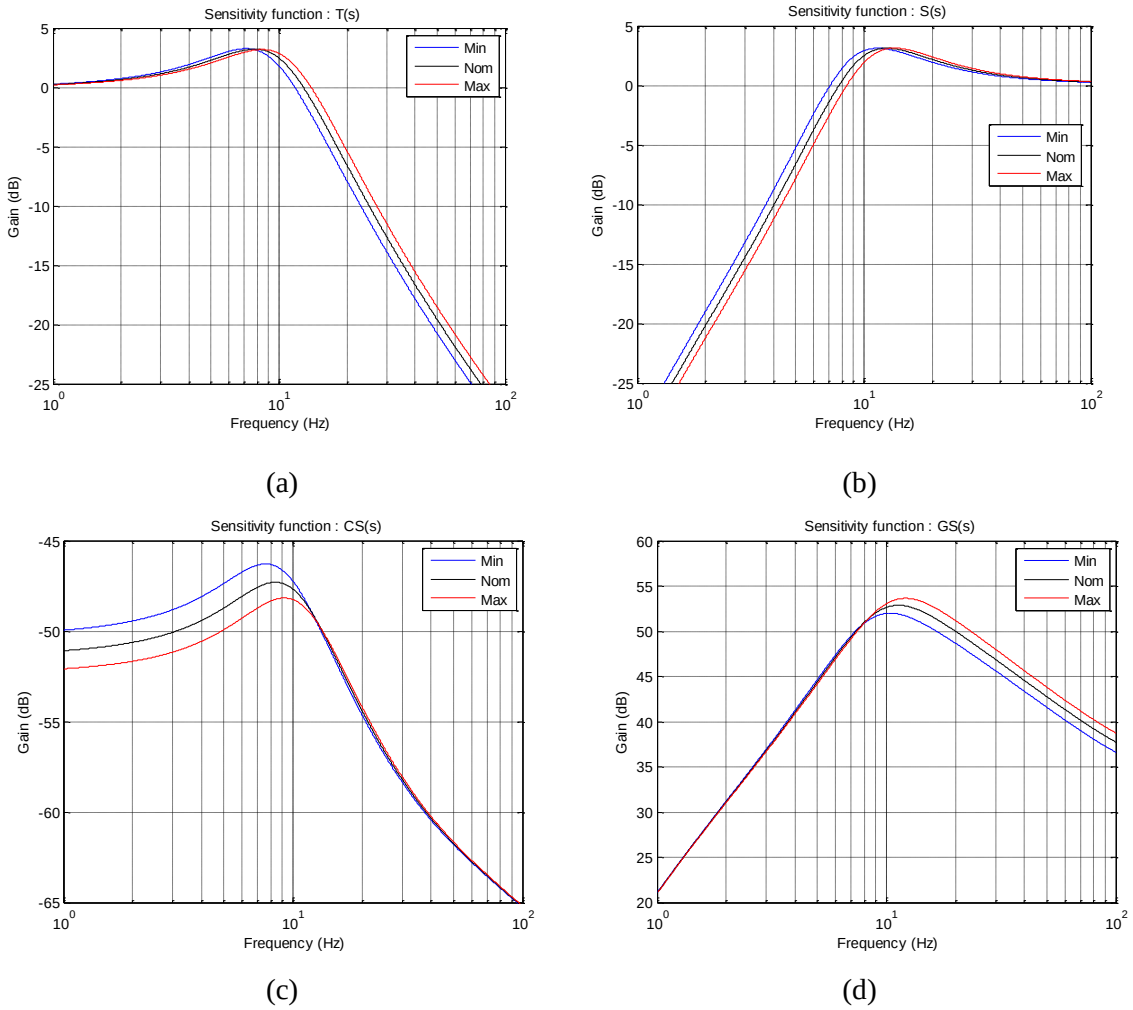

Figure 3.14 – Bode plots of *T(jω)* (a), of *S(jω)* (b), of *CS(jω)* (c) and *GS(jω)* (d) obtained with the CRONE controller for the three cases: min (4 bar in blue), nom (5 bar in black) and max (6 bar in red)

3.6.2 – Time Domain

The reference pressure $P_{ref}(t)$ is chosen such as:

$$\text{for} \begin{cases} t = 0 \text{ to } t_0,\ P_{ref}(t) = P_{ref}^e \\ t = t_0 \text{ to } t_1 = t_0 + T_0,\ P_{ref}(t) = P_{ref}^e + P_{ref}^0 \cos(2\pi\ t / T_0) \\ t = t_1 \text{ to } t_2 = 2t_0 + T_0,\ P_{ref}(t) = P_{ref}^e \end{cases}, \tag{3.37}$$

with $t_0 = 0.1$ s, $T_0 = 1$ s, $P_{ref}^e = 750$ Pa and $P_{ref}^0 = 185$ Pa .

It is important to note that the gain of the feedforward part is calculated only for the nominal case $P_1 = 5$ bar and that it is not adjusted when P_1 varies upstream the servo-valve.

Figure 3.15 presents time responses of $P_{ref}(t)$ and $P_m(t)$ (a) (b), of error signal $\varepsilon(t) = P_{ref}(t) - P_m(t)$ (c) (d), and of control signal $U_c(t)$ (e) (f) obtained without feedback (a) (c) (e) and with feedback (b) (d) (f) for the three cases (min, nom, max).

We observe that the robust feedback and feedforward control system ensures a good pressure tracking (b) (d), not only for the nominal case (P_1 = 5 bar), but also for the minimal (P_1 = 4 bar) and maximal (P_1 = 6 bar) cases. Without the robust feedback control system (a) (c), pressure tracking is less effective. In all cases, the control signal $U_c(t)$ (e) (f) remains within the variation range defined by U_{min} and U_{max}.

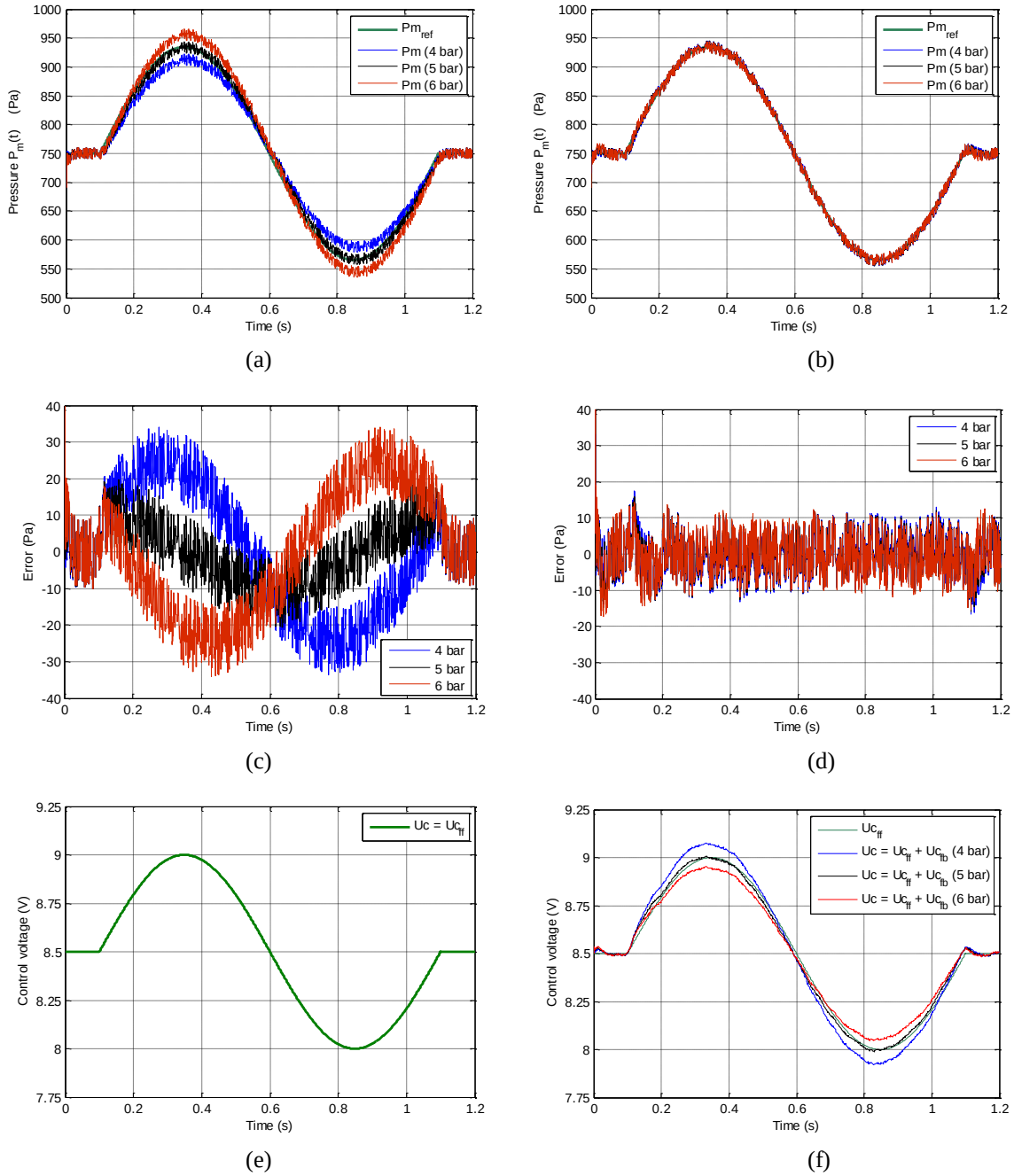

Figure 3.15 – Time responses of $P_{ref}(t)$ and $P_m(t)$ (a) (b), of error signal $\varepsilon(t)$ (c) (d), and of control signal $U_c(t)$ (e) (f) obtained without feedback (a) (c) (e) and with feedback (b) (d) (f) for the three cases: min (4 bar in blue), nom (5 bar in black) and max (6 bar in red)

3.7 – Conclusion

The first important work of this chapter was to mathematically describe, model, and simulate the linear and nonlinear parts of the servo valve and the artificial mouth and try to linearize their modeled equations. Moreover, understanding the influence of pressure P_1 on the limits of the servo-valve operating range is essential in order to be then able to define a strategy for automatic pressure P_m control inside the artificial mouth. The second important step is the design of the control architecture for a robust control of the pressure P_m. The application of the CRONE system design methodology was able to achieve the target set with very good dynamic performance and respecting the linear operating range of the servo valve.

Chapter 4- Analysis of the Influence of Fractional Order on the Stationary Periodic System

4.1 – Introduction

This chapter 4 uses the developments of chapters 1, 2 and 3 in order to analyze the influence of the fractional order *m* on the stationary periodic system. As a reminder, Figure 4.1 illustrates the progression and sequencing of the chapters of this thesis.

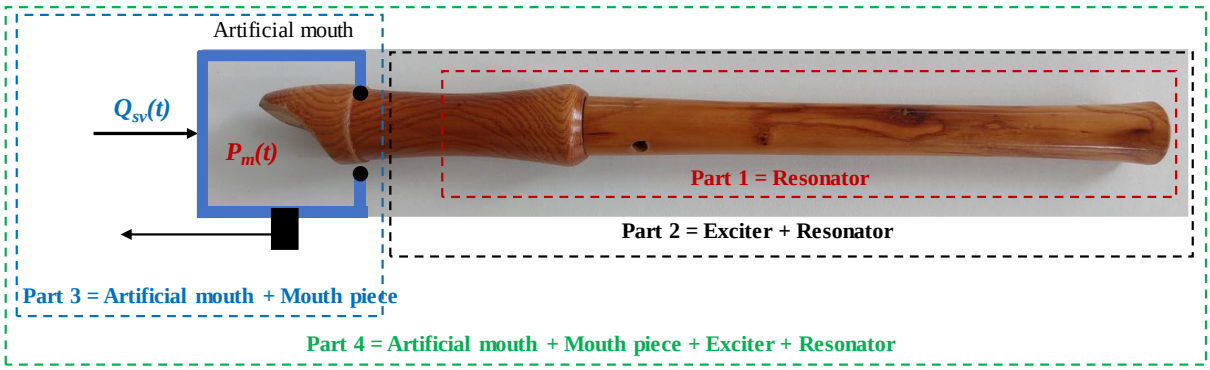

Figure 4.1 - Illustration of the progression and sequencing of the chapters of the thesis dissertation

Thus, from the extension of the fractional model proposed in chapter 2, it is possible with a single high-level parameter, the order *m* in this case, to easily vary in numerical simulation, the visco-thermal losses, while from an experimental point of view, it would be necessary to manufacture and test a large number of resonators with dimensions (length *L* and radius *r*), roughness (or surface condition) and different materials (wood, plastic, etc.).

This chapter therefore begins by recalling the organization of the global simulator developed under MatLab / Simulink from the work presented in the first three chapters. Then, an analysis in the frequency domain of the influence of the order *m* is developed, first in the case of the impedance of the resonator established in Chapter 2, then in the case of the defined open-loop transfer function in Chapter 3. This analysis continues in the time domain with the responses from the global simulator by using the scenarios of the two examples of Chapter 3. Finally, the main contributions of this chapter are recalled in the conclusion.

4.2 – Simulator of the Artificial Mouth – Recorder Set: Reminder

Figure 4.2 shows the block diagram of the global simulator used in this chapter. It consists of:

- the artificial mouth simulator (Chapter 3);
- the exciter simulator (Chapter 2).

The artificial mouth simulator has undergone a readjustment with respect to the test bench developed specifically for this study. The regulation loop makes it possible, in particular, to limit the sensitivity of the pressure $P_m(t)$ within the pneumatic capacity to variations in the supply pressure $P_1(t)$ of the servo valve. As part of the analysis of the influence of fractional order on the stationary periodic system, the reference pressure $P_{ref}(t)$ is a constant equal to 400 Pa (example 1) and 1000 Pa (example 2).

The exciter simulator, on the other hand, is the one developed in Chapter 2. The fractional order is present in the acoustic tube model studied in Chapter 1 as a resonator.

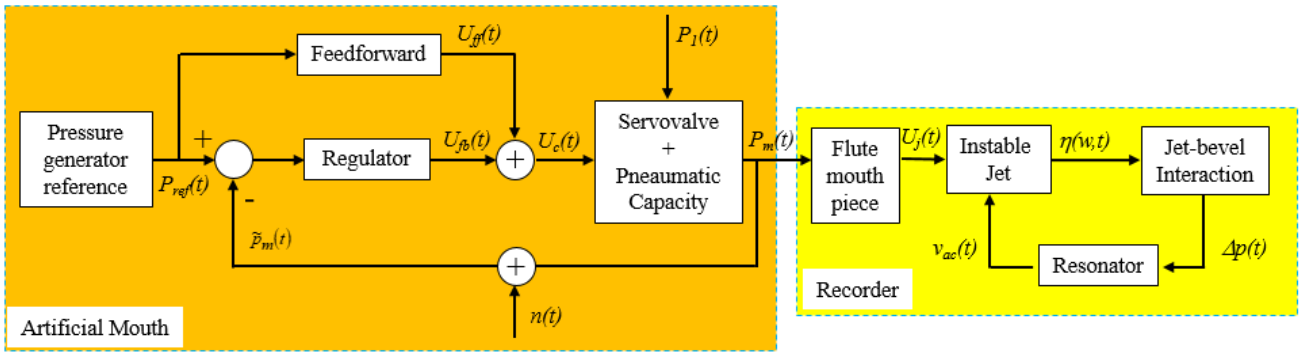

Figure 4.2 - Functional diagram of the entire simulator

4.3 – Frequency domain analysis of the influence of fractional order

4.3.1 – Case of the Resonator Impedance

As a reminder (refer to Chapter 2) and for the field of study defined within the framework of this thesis work, the input admittance $Y_{in}(s)$ of the acoustic tube (resonator) of length L and radius r has the expression:

$$Y_{in}(s) = \frac{S}{Z_{ac}} I_m(s) \frac{1}{\tanh(z(s))} \quad , \tag{4.1}$$

with

$$I_m(s) = \sqrt{\frac{1+\left(\frac{s}{\omega_{r,m}}\right)^m}{\left(\frac{s}{\omega_{r,m}}\right)^m}} \tag{4.2}$$

and

$$z(s) = \left(\frac{s}{\omega_L}\right)\sqrt{\frac{1+\left(\frac{s}{\omega_{r,m}}\right)^m}{\left(\frac{s}{\omega_{r,m}}\right)^m}}\ , \tag{4.3}$$

where $Z_{ac} = \rho_a c_a$ represents the characteristic acoustic impedance, S the section of the acoustic tube, and where the transitional frequencies $\omega_{r,m}$, and ω_L have the expression:

$$\omega_{r,m} = c_a \left(\frac{4\ m\ K_0}{r}\right)^{1/m} \quad \text{and} \quad \omega_L = \frac{c_a}{L}. \tag{4.4}$$

Still as a reminder, the numerical values retained for the study are $r = 5\text{x}10^{-3}$m, $L = 0.3$ m, with a temperature of 25°C where $\rho_a = 1.184$ kg/m^3 and $c_a = 346.3$ m/s, $K_0 = 2.98\text{x}10^{-4}$. In this case, $\omega_L = 1\ 154$ rad/s (184 Hz). As for $\omega_{r,m}$, Figure 4.3 shows its plot as a function of the order m and Table 4.1 gives precisely the values corresponding to the 5 orders retained thereafter.

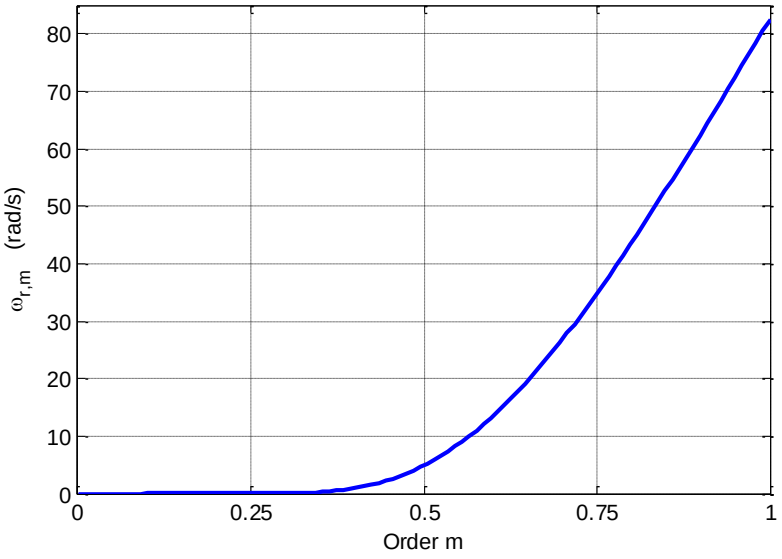

Figure 4.3 – Plot of $\omega_{r,m}$ as a function of the order m

Table 4.1 – Values of $\omega_{r,m}$ as a function of the order m

m		0	0.25	0.5	0.75	1
$\omega_{r,m}$	rad/s	0	$4.4\ 10^{-3}$	4.92	34.88	82.55
	Hz	0	$7\ 10^{-4}$	0.783	5.55	13.14

In addition, the expression (4.1) of $Y_{in}(s)$ can be put in a form $Y_N(s)$ composed of an integrator of order 1 in cascade with N fractional cells of order 2, namely:

$$Y_{in}(s) = \lim_{N\to\infty} Y_N(s) \quad , \tag{4.5}$$

with

$$Y_N(s) = \frac{Y_0}{s} \prod_{i=1}^{N} \left(\frac{1 + 2\zeta_{zi} \left(\frac{s}{\omega_{zi}} \right)^{2-m} + \left(\frac{s}{\omega_{zi}} \right)^2}{1 + 2\zeta_{pi} \left(\frac{s}{\omega_{pi}} \right)^{2-m} + \left(\frac{s}{\omega_{pi}} \right)^2} \right) \quad , \tag{4.6}$$

where

$$Y_0 = \frac{S}{\rho_a L} \tag{4.7}$$

and

$$\begin{cases} \omega_{zi} = c_{zi}\, \omega_L \quad ; \quad \zeta_{zi}(m) = \dfrac{2\,K_0}{r} \left(\dfrac{L}{c_{zi}} \right)^m m \\ \omega_{pi} = c_{pi}\, \omega_L \quad ; \quad \zeta_{pi}(m) = \dfrac{2\,K_0}{r} \left(\dfrac{L}{c_{pi}} \right)^m m \end{cases} , \tag{4.8}$$

where c_{zi} and c_{pi} are constants resulting from the procedure allowing to pass from $Y_{in}(s)$ to $Y_N(s)$. This procedure, presented in appendix A, is composed of 4 steps:

- **Step 1:** finite expansion of the function *tanh(z)* into a continuous fraction in *z*;

- **Step 2:** reduction of the continuous fraction to a ratio of two polynomials in *z*;

- **Step 3:** factorization of each polynomial in *z*;

- **Step 4**: rewriting $Y_{in}(s)$ in the form $Y_N(s)$, namely an integrator of order 1 in cascade with a product of N fractional cells of order 2.

From a numerical point of view, there is no limitation on the choice of the number of cells N, the precision being the better the number N is high. Theoretically, N must be infinite. Thus, any finite value of N causes an edge effect on the last cell linked to the truncation. This is the reason why we must choose an expansion of order $N + 1$ to have good precision with N cells.

From an analytical point of view, the search for the roots of the polynomials obtained in step 2 (research necessary for factorization at the level of step 3) limits N to 2. Taking into

account the edge effects, the analytical developments do not can only be used for the first cell which corresponds to the first mode of the resonator.

Figure 4.4 shows on the range [100; 2000] Hz for $m = 0.5$ the frequency responses of $Y_{in}(s)$ (in black) and of $Y_N(s)$ (in red) for $N = 2$. The integrative behavior of order 1 present at low frequencies is perfectly reproduced by the equation (4.6), as well as the behavior associated with anti-resonance and resonance of the first mode. Beyond that, the side effect linked to the truncation ($N = 2$) appears clearly.

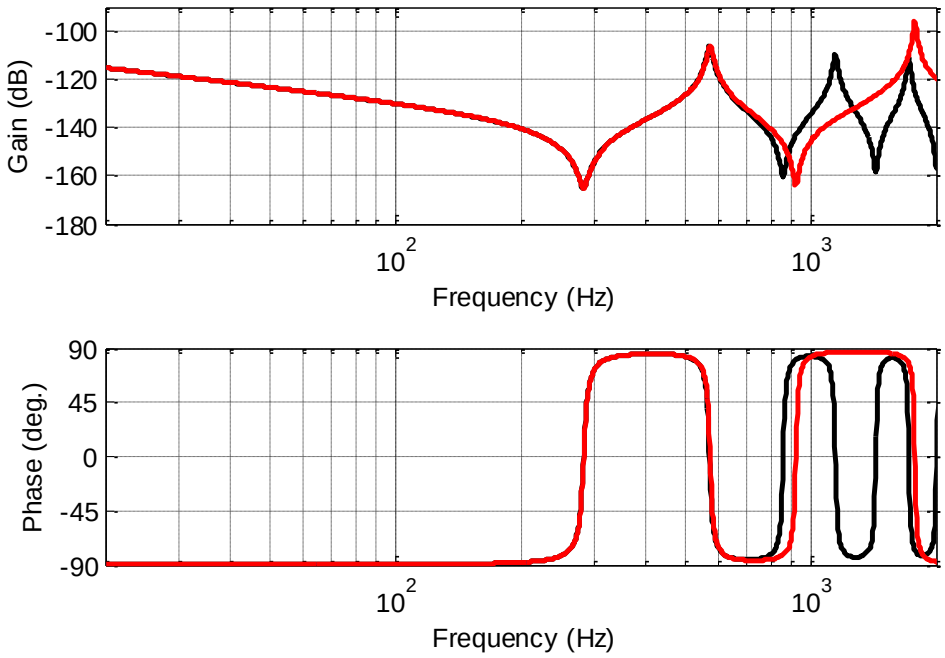

Figure 4.4 – In the range [100; 2000] Hz and for $m = 0.5$, frequency responses of $Y_{in}(s)$ (in black) and of $Y_N(s)$ (in red) for $N = 2$

However, the analysis of expressions (4.6) and (4.8) shows that each cell of rank i is completely defined as soon as the two constants c_{zi} and c_{pi} are known. Based on this observation, a specific method is proposed in 3 steps.

Step 1 consists of determining the pulsations ω_{zi} and ω_{pi} solutions of the equation:

$$\arg Y_{in}(j\omega) = 0 \quad , \tag{4.9}$$

knowing that the phase curve alternates between -90 ° and + 90 ° (Figure 4.4), and that the ω_{zi} correspond to solutions for which the slope of the phase curve of $Y_{in}(j\omega)$ is positive (anti-resonance), i.e.:

$$\frac{d}{d\omega}\arg Y_{in}(j\omega)\Big|_{\omega=\omega_{zi}} > 0 \tag{4.10}$$

and the ω_{pi} to the solutions for which the slope of the phase curve of $Y_{in}(j\omega)$ is negative (resonance), namely:

$$\left.\frac{d}{d\omega}\arg Y_{in}\left(j\omega\right)\right|_{\omega=\omega_{pi}} < 0\,. \tag{4.11}$$

Given the complexity of the expression of $Y_{in}(j\omega)$, the search for the roots is done numerically at the scale of each cell of rank i.

Then, for a given pulse ω_L, the constants c_{zi} and c_{pi} are calculated in step 2 in accordance with relations (4.8), namely:

and

$$\begin{cases} c_{zi} = \dfrac{\omega_{zi}}{\omega_L} \\ \\ c_{pi} = \dfrac{\omega_{pi}}{\omega_L} \end{cases}. \tag{4.12}$$

Finally, for a given order m, step 3 makes it possible to calculate the damping factors ζ_{zi} and ζ_{pi} of $Y_N(s)$ in accordance with relations (4.8), namely:

$$\begin{cases} \zeta_{zi}\left(m\right) = \dfrac{2\,K_0}{r}\left(\dfrac{L}{c_{zi}}\right)^m m \\ \\ \zeta_{pi}\left(m\right) = \dfrac{2\,K_0}{r}\left(\dfrac{L}{c_{pi}}\right)^m m \end{cases}. \tag{4.13}$$

Figure 4.5 shows on the range [100; 4000] Hz for $m = 0.75$ the frequency responses of $Y_{in}(s)$ (in black) and of $Y_N(s)$ (in red) for $N = 4$, minimum value to cover the field of study defined within the framework of this thesis work. Comparing the responses in Figure 4.4 allows us to appreciate the effectiveness of the proposed method. Indeed, the behavior associated with the anti-resonance and the resonance of the first three modes is perfectly reproduced. Beyond that, the side effect linked to the truncation ($N = 4$) appears clearly.

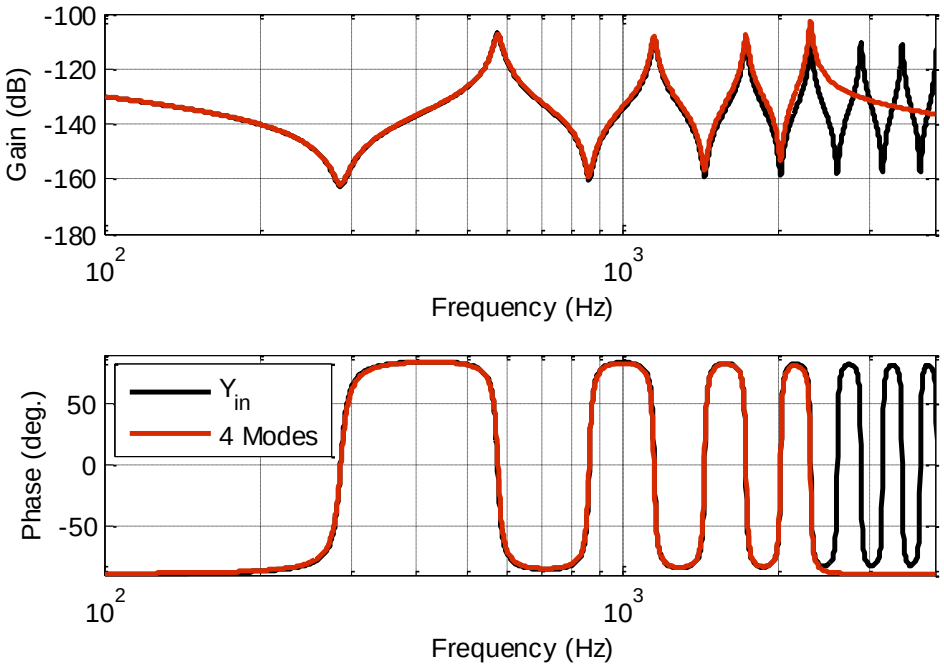

Figure 4.5 – In the range[100; 4000] Hz and for m = 0.75, frequency responses of $Y_{in}(s)$ (in black) and of $Y_N(s)$ (in red) for N = 4

■ Remark

The denominator Den(s) of $Y_N(s)$ is defined by:

$$Den(s) = s\prod_{i=1}^{N} Den_i(s) \quad , \tag{4.14}$$

with

$$Den_i(s) = 1 + 2\zeta_{pi}\left(\frac{s}{\omega_{pi}}\right)^{2-m} + \left(\frac{s}{\omega_{pi}}\right)^{2} \quad . \tag{4.15}$$

The roots of Den(s) are solution of Den(s) = 0. Apart from the obvious root s = 0, the search for the roots is done by solving

$$\prod_{i=1}^{N} Den_i(s) = 0 \quad , \tag{4.16}$$

which amounts to looking for the roots of each $Den_i(s)$ polynomial.

The interested reader will find in the thesis (Ivanova, 2017) *developments concerning, in particular, the search for the roots of a polynomial of the form of $Den_i(s)$.* ■

Note that the ratio ω_{pi}/ω_{zi} only depends on c_{pi} and c_{zi} namely:

$$\begin{cases} \dfrac{\omega_{pi}}{\omega_{zi}} = \dfrac{c_{pi}}{c_{zi}} \end{cases} , \tag{4.17}$$

and that the ratio ζ_{pi}/ζ_{zi} depends on c_{pi}, c_{zi} and m, that is to say:

$$\frac{\zeta_{p_i}}{\zeta_{z_i}} = \left(\frac{c_{z_i}}{c_{p_i}} \right)^m . \tag{4.18}$$

Like the recursive factors α and η used by Oustaloup (Oustaloup A. , 1995) to establish the link between non-integer derivation and frequency recursion, ratios α_i and η_i (whose values depend here on rank i) are introduced:

$$\begin{cases} \alpha_i = \dfrac{\omega_{pi}}{\omega_{zi}} = \dfrac{c_{pi}}{c_{zi}} > 1 \\ \\ \eta_i = \dfrac{\omega_{z_{i+1}}}{\omega_{p_i}} = \dfrac{c_{z_{i+1}}}{c_{p_i}} > 1 \end{cases} . \tag{4.19}$$

Taking into account relations (4.18) and (4.19), the ratio of the damping factors ζ_{zi} and ζ_{pi} of the same cell of rank i is then written only as a function of α_i and of the order m, that is to say:

$$\frac{\zeta_{p_i}}{\zeta_{z_i}} = \frac{1}{\alpha_i^m} < 1 , \tag{4.20}$$

and the passage relations of the parameters of the cell of rank i and those of the cell of rank $i + 1$, are given by

$$\begin{cases} \dfrac{\omega_{z_{i+1}}}{\omega_{z_i}} = \alpha_i \, \eta_i > 1 \quad ; \quad \dfrac{\zeta_{z_{i+1}}}{\zeta_{z_i}} = \dfrac{1}{(\alpha_i \, \eta_i)^m} < 1 \\ \dfrac{\omega_{p_{i+1}}}{\omega_{p_i}} = \alpha_i \, \eta_i > 1 \quad ; \quad \dfrac{\zeta_{p_{i+1}}}{\zeta_{p_i}} = \dfrac{1}{(\alpha_i \, \eta_i)^m} < 1 \end{cases} . \tag{4.21}$$

Relations (4.21) show that:

- the resonance frequencies ω_{pi} and anti-resonance ω_{zi} are independent of the order m and increase with rank i;

- the damping factors depend on the order m and decrease with rank i for a fixed m.

Table 4.2 specifies the different parametric values which characterize the cells of ranks 1 to 4 within the framework of the work of this thesis.

Table 4.2 – Parametric values which characterize the cells of ranks 1 to 4 in the framework of the work of this thesis

Rank *i*	**1**	**2**	**3**	**4**
ω_{zi} (rad/s)	1814	5412	9030	12660
ω_{pi} (rad/s)	3639	7218	10860	14460
c_{zi}	1.572	4.688	7.823	10.967
c_{pi}	3.153	6.253	9.408	12.527
α_i	2	1.334	1.203	1.142
η_i	1.487	1.251	1.166	
$\alpha_i \eta_i$	2.983	1.668	1.402	

Figure 4.6 presents the variation of the damping factors ζ_{z1} and ζ_{p1} of rank 1 (1st mode of the resonator) according to the order *m* ranging between 0 and 1. These plots are obtained from the analytical relations (4.13).

These plots show two zones:

- Zone 1, where the damping factors increase with the order *m*, with $m = 0$ (conservative case) up to a maximum value, that is to say: max $[\zeta_{z1}] = 0.0265$ for $m = 0.6$ and max $[\zeta_{p1}] = 0.0186$ for $m = 0.43$;

- Zone 2, where, on the contrary the damping factors decrease until a value of $\zeta_{z1} = 0.0228$ and $\zeta_{p1} = 0.0113$ for $m = 1$.

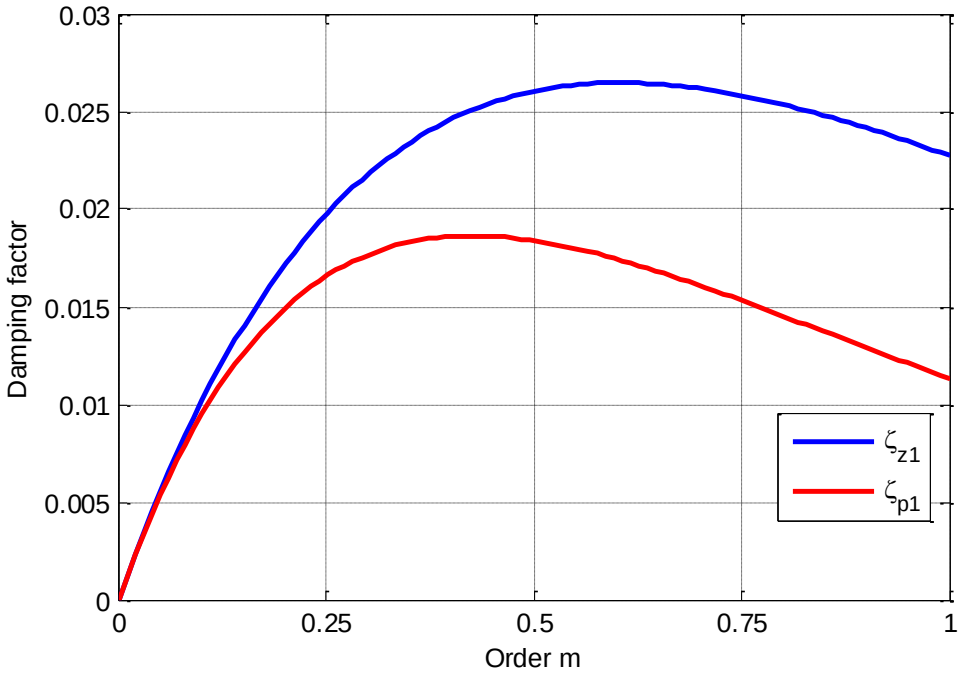

Figure 4.6 – Variation of the damping factors ζ_{z1} and ζ_{p1} of the first mode of the resonator as a function of the order *m* between 0 and 1

Moreover, the expressions (4.13) of ζ_{z1} and ζ_{p1} clearly show that for a given rank *i* and an order *m*, the damping factors are all the greater (and therefore the visco-thermal losses) as the length *L* of the acoustic tube is large and its radius *r* is small.

Figures 4.7 and 4.8 show the frequency responses of the input admittance $Y_{in}(s)$ of the resonator for different values of the fractional order *m* between 0 and 1, with the frequency axis scaled:

- logarithmic over the range [100; 2000] Hz (Figure 4.7);

- linear over the range [100; 1400] Hz (Figure 4.8).

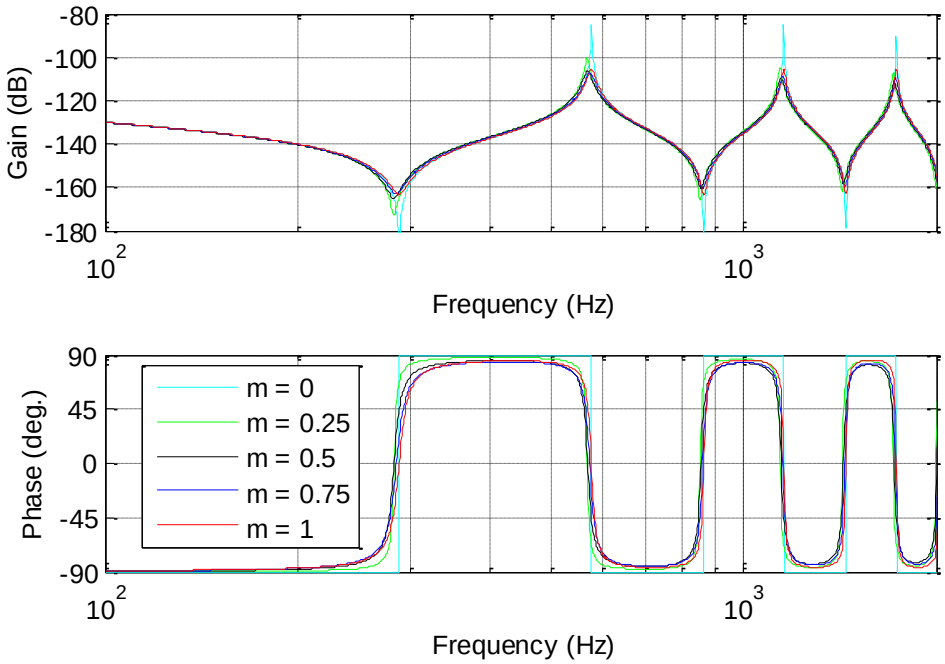

Figure 4.7 – Bode plots of the admittance $Y_{in}(s)$ of the resonator for different values of the fractional order *m* over the range [100; 2000] Hz

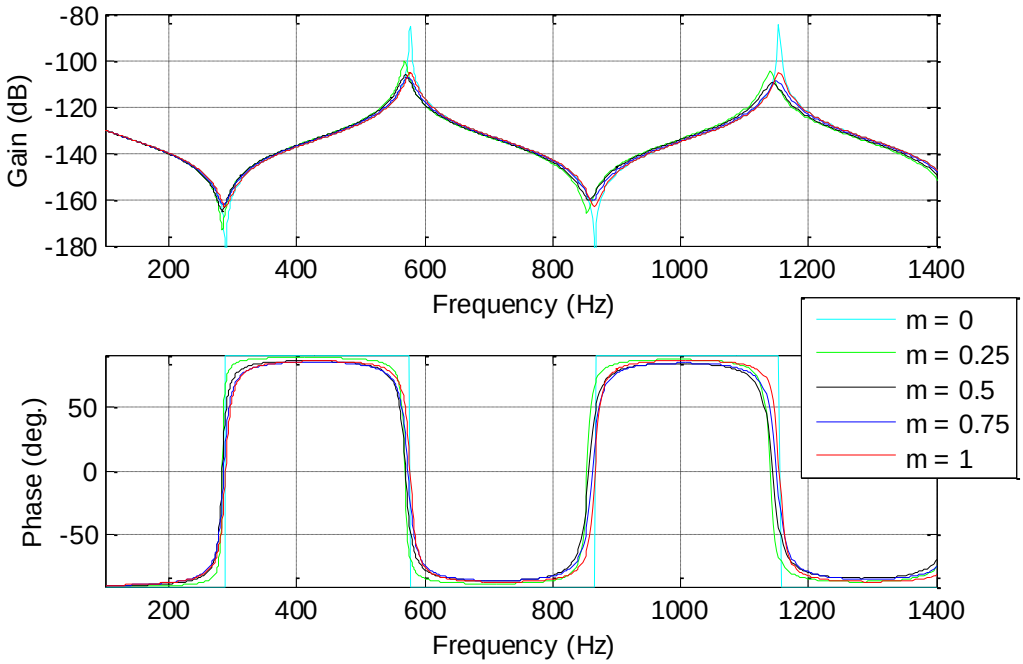

Figure 4.8 – Frequency responses $Y_{in}(j\omega)$ of the resonator admittance for different values of the fractional order *m* with the linear scale frequency axis in the range [100; 1400] Hz

In addition to Figures 4.7 and 4.8, Figures 4.9 to 4.11 present the distributions:

- anti-resonance ω_{zi}(o) and ω_{pi}(x) resonance frequencies (Figure 4.9),

- damping factors ζ_{zi} (Figure 4.10.a) and ζ_{pi} (Figure 4.10.b),

- constants c_{zi} and c_{pi} (Figure 4.11.a), as well as factors α_i, η_i and $\alpha_i * \eta_i$ (Figure 4.10.b),

according to the first 4 modes admittance of the $Y_{in}(s)$ of the resonator.

All its figures clearly illustrate the remarks already made concerning the different parameters of $Y_N(s)$ as a function of rank i.

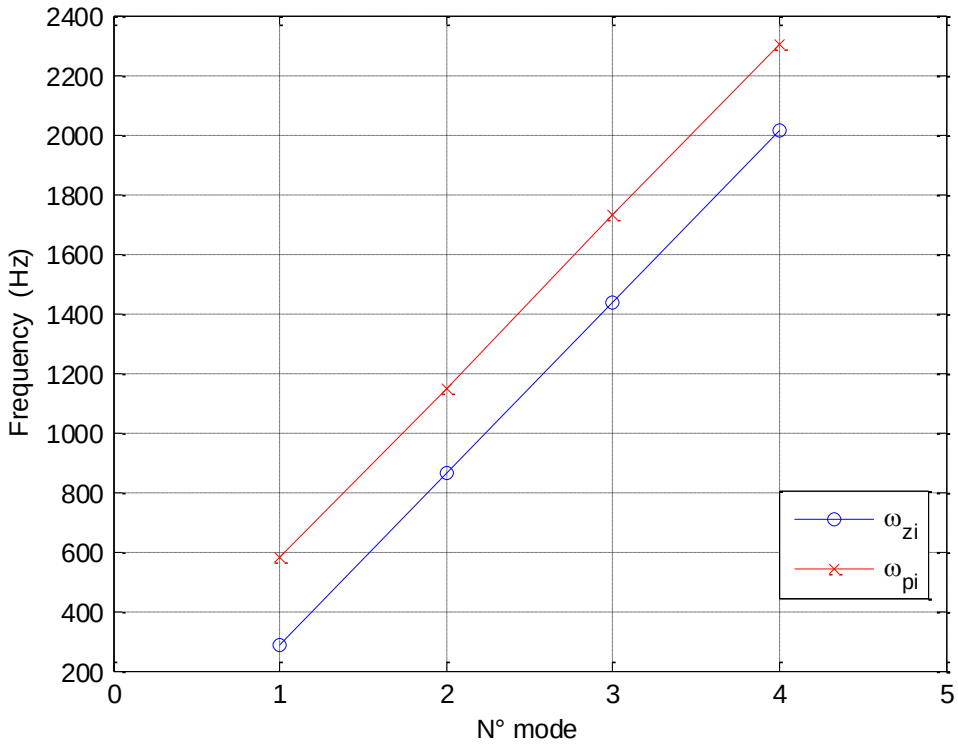

Figure 4.9 – Distribution of anti-resonance ω_{zi} (o) and resonance ω_{pi} (x) frequencies according to the first 4 modes of the admittance *Yin(s)* of the resonator

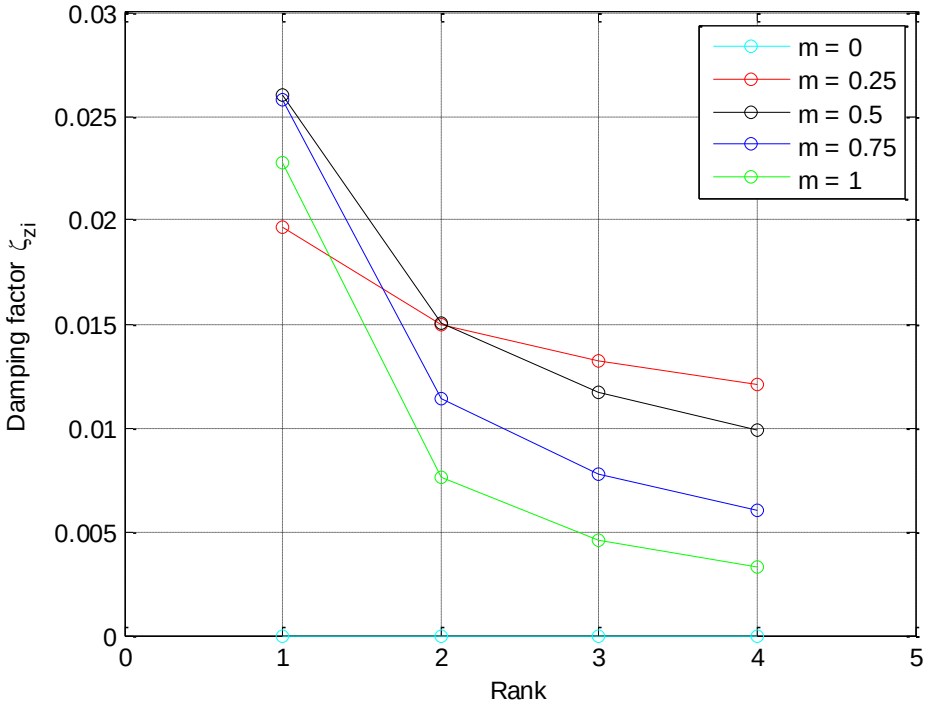

(a)

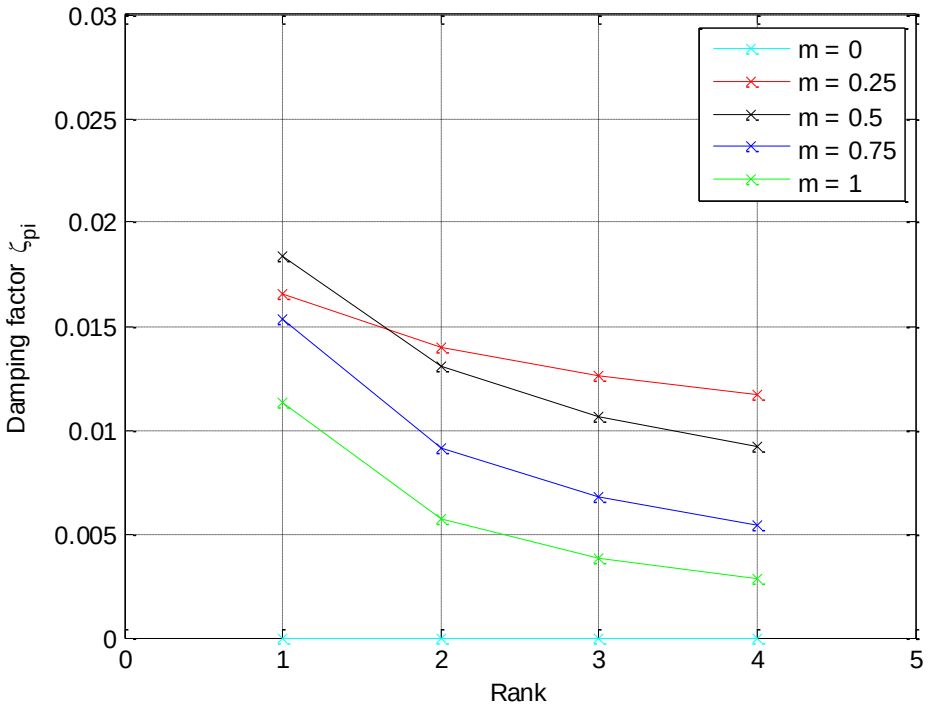

(b)

Figure 4.10 – Distribution of damping factors ω_{zi} (a) and ω_{pi} (b)according to the first 4 ranks of the $Y_N(s)$ admittance of the resonator for 5 values of the order *m* (0; 0.25; 0.5; 0.75; 1)

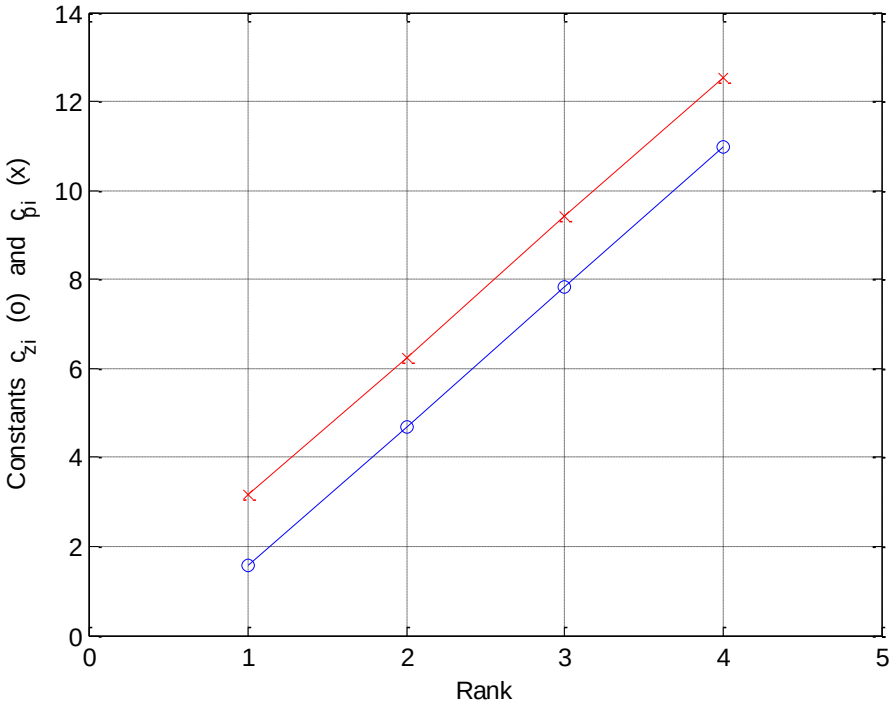

(a)

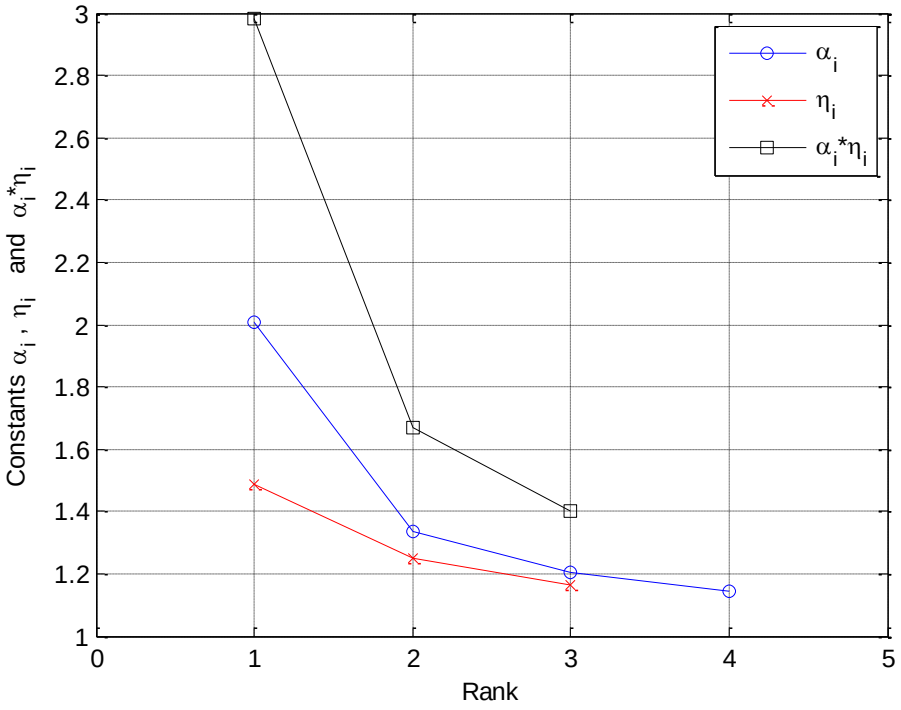

(b)

Figure 4.11 – Distribution of the constants $c_{zi}(o)$ and $c_{pi}(x)$ (a); α_i (o), $\eta_i(x)$ and $\alpha_i(o)*\eta_i(x)$ (b) according to the first 4 ranks of the admittance $Y_N(s)$ of the resonator

4.3.2 - Case of the Open Loop Transfer Function

The frequency domain analysis of the influence of the fractional order *m* continues in this section with the open-loop transfer function, $\beta(s)$, established in Chapter 3.

As a reminder, its frequency response $\beta(j\omega)$ in steady harmonic system resulting from the linearization carried out in Chapter 3 has the expression:

$$\beta(j\omega) = \beta_0 \; j\omega \; e^{-\tau j\omega} \, Y_{in}(j\omega) \; , \tag{4.22}$$

with β_0 a constant whose expression is given by:

$$\beta_0 = \frac{h \exp(\alpha_i \, w)}{S} \, \frac{\delta_d}{w} \, \rho \left(1 - \left(\tanh\left(-\frac{x_0}{b} \right) \right)^2 \right) \; , \tag{4.23}$$

the gain and the phase of $\beta(j\omega)$ expressed as:

$$\begin{cases} \beta(\omega) = \left| \beta(j\omega) \right| = \beta_0 \, \omega \left| Y_{in}(j\omega) \right| \\ \phi(\omega) = \arg \beta(j\omega) = \dfrac{\pi}{2} - \tau \, \omega + \arg Y_{in}(j\omega) \end{cases} . \tag{4.24}$$

Always as a reminder:

- the gain $\beta(\omega)$ of the open loop does not depend on the flow speed U_j^e at the output of the channel and therefore on the pressure P_m = cst at the input of the mouthpiece;

- on the other hand, the phase $\phi(\omega)$ of the open loop depends on the speed of flow U_j^e through the delay $\tau = \dfrac{w}{0.4 \, U_j^e}$, the latter being as much greater as U_j^e is weak.

In addition, for this linearized loop system within the scope of study of this thesis work, the two auto-oscillation conditions are:

and

$$\begin{cases} \beta_u = \left| \beta(j\omega_u) \right| = \beta_0 \, \omega_u \left| Y_{in}(j\omega_u) \right| = 1 \\ \\ \phi_u = \arg \beta(j\omega_u) = \dfrac{\pi}{2} - \tau \, \omega_u + \arg Y_{in}(j\omega_u) = 0 \end{cases} , \tag{4.25}$$

ω_u being the pulsation at unity gain.

In fact, as already specified in Chapter 3, the stationary periodic system observed in the time domain (see following paragraph), in particular in example 1 (P_m = 400 Pa) and example 2 (P_m = 1000 Pa), does not result from these self-oscillation conditions. This system is the result of an unstable behavior (in closed loop) which associated with the nonlinear phenomenon of saturation of the *tanh(.)* function leads to this steady periodic system.

These conditions of stationary periodic system (in closed loop) result in open loop by a gain $\beta(\omega_0)$ strictly greater than the unit with the pulsation ω_0 for which the phase $\phi(\omega_0)$ is zero, that is to say:

If at $\omega = \omega_0$,

$$\begin{cases} \phi(\omega_0) = \arg\beta(j\omega_0) = \dfrac{\pi}{2} - \tau\,\omega_0 + \arg Y_{in}(j\omega_0) = 0 \\ \beta(\omega_0) = \left|\beta(j\omega_0)\right| = \beta_0\,\omega_0\left|Y_{in}(j\omega_0)\right| > 1 \end{cases}, \qquad (4.26)$$

then the system is unstable (closed loop).

For the five values of the order *m* (0; 0.25; 0.5; 0.75; 1), Figures 4.12 and 4.13 show the frequency responses $\beta(j\omega)$ of the open-loop transfer function in the planes:

- from Bode (Figure 4.12);

- from Black-Nichols (Figure 4.13),

for

- P_m = 400 Pa (Figures 4.12.a and 4.13.a);

- P_m = 1000 Pa (Figure 4.12.b and 4.13.b).

Figure 4.14 is a zoom of Figure 4.13 in the Black-Nichols plane around the point (0°, 0 dB), or (0°, 1), thus allowing to better visualize the conditions (4.26).

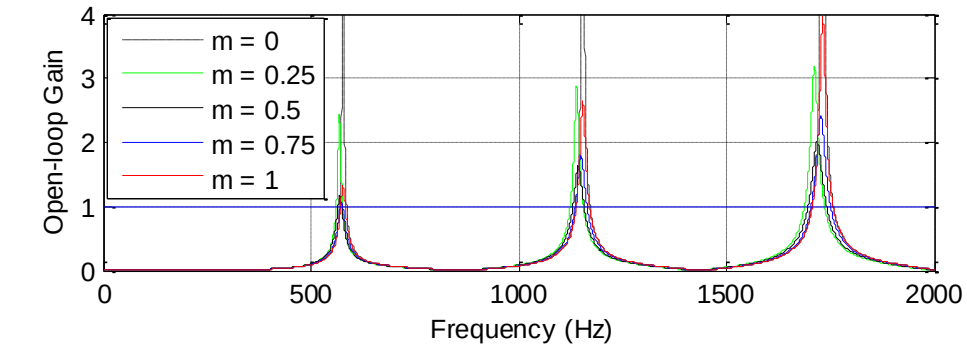

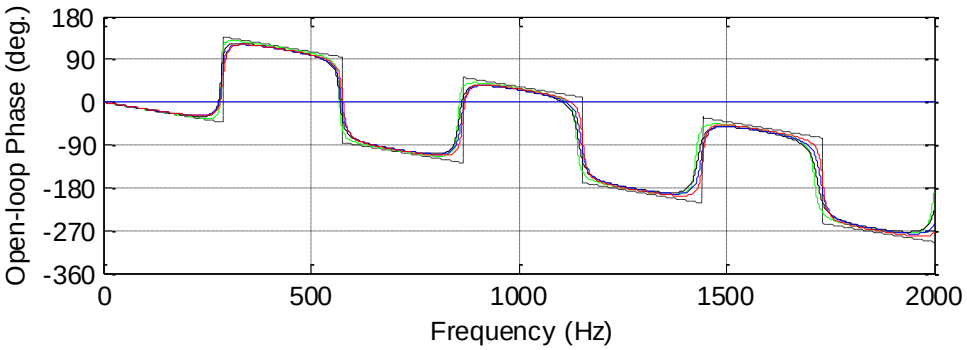

(a)

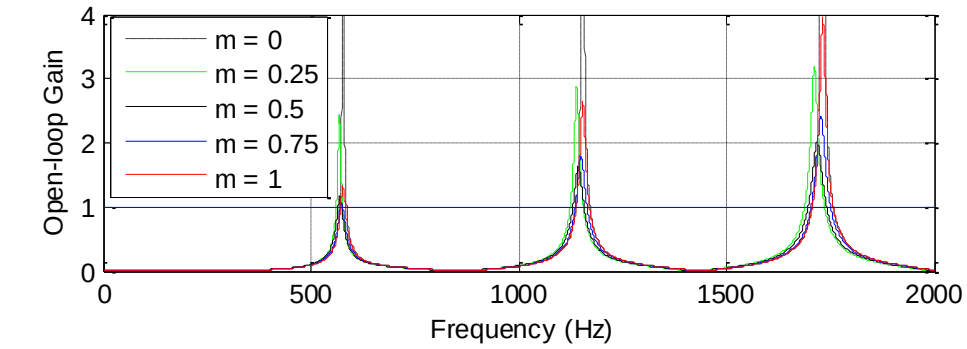

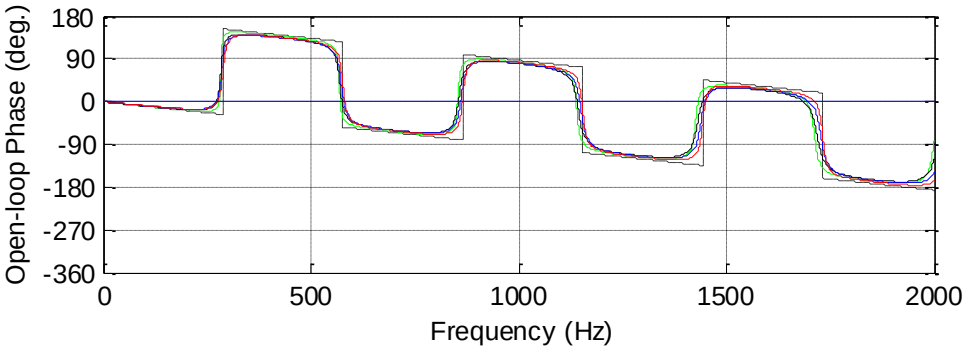

(b)

Figure 4.12 – Bode diagrams of the frequency response $\beta(j\omega)$ in open loop for P_m = 400 Pa (a) and for P_m = 1000 Pa (b), for 5 values of the order m (0; 0.25; 0.5; 0.75; 1)

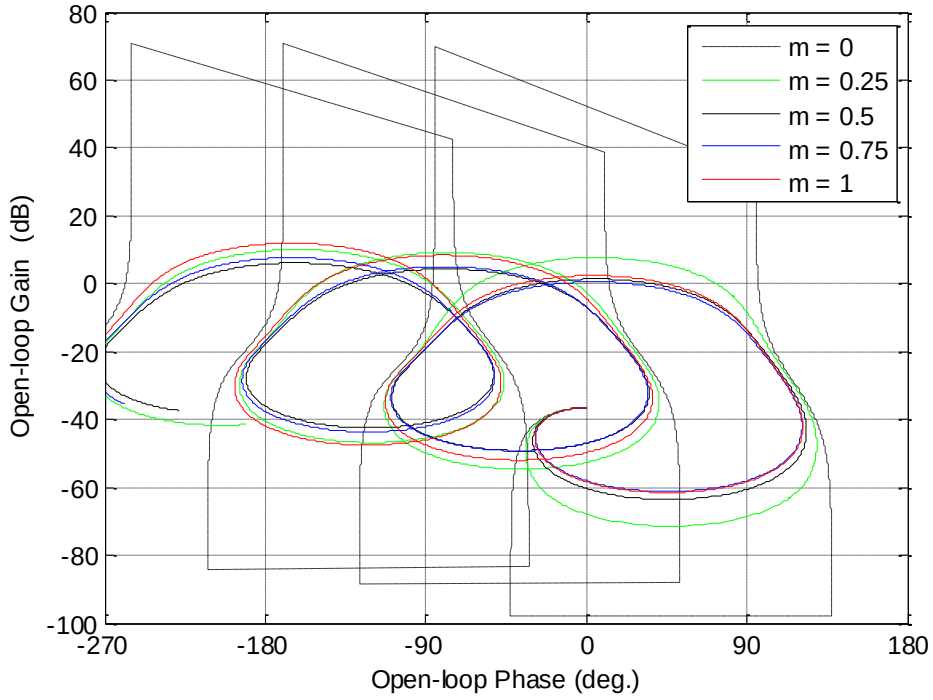

(a)

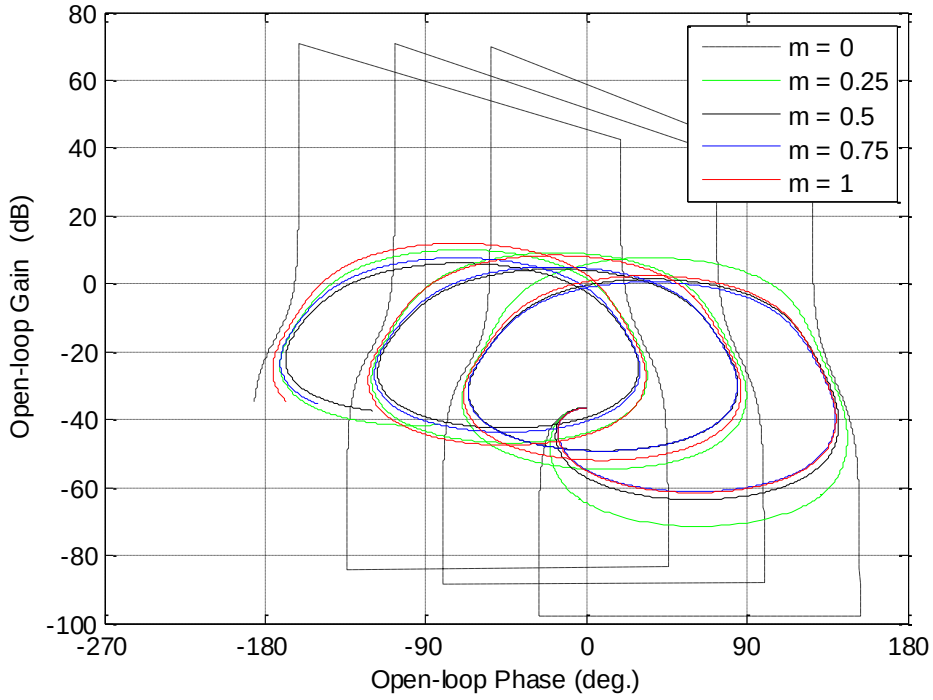

(b)

Figure 4.13 – Frequency responses $\beta(j\omega)$ in open loop in the Black-Nichols plane for P_m = 400 Pa (a) and for P_m = 1000 Pa (b), for 5 values of the order m (0; 0.25; 0.5; 0.75; 1)

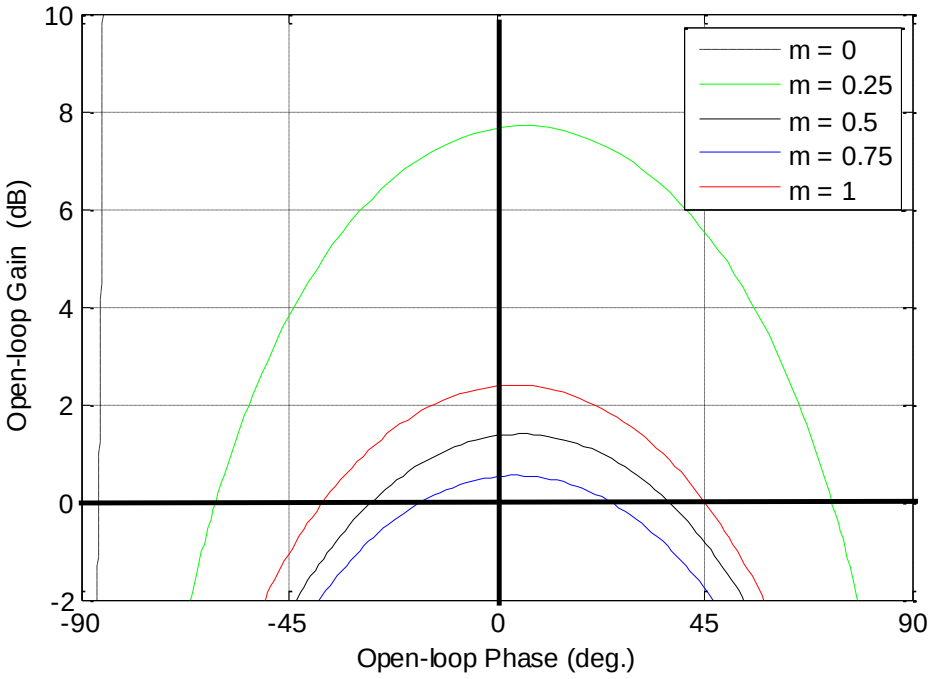

(a)

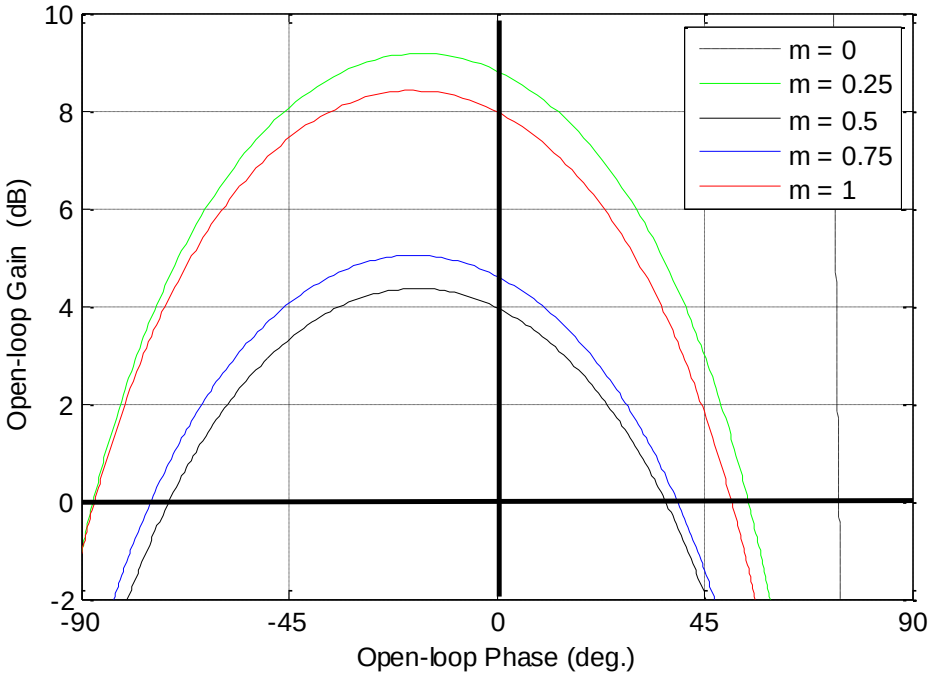

(b)

Figure 4.14 – Zoom of the frequency responses $\beta(j\omega)$ in open loop in the Black-Nichols plane around the point (0°; 0 dB) for P_m = 400 Pa (a) and for P_m = 1000 Pa (b), for 5 values of the order m (0; 0.25; 0.5; 0.75; 1)

The observation of the frequency responses $\beta(j\omega)$ of the open loop, in particular in the Black-Nichols plane with Figure 4.13, makes it possible to affirm that for the two values of the pressure P_m = 400 Pa and 1000 Pa, and whatever the value of m between 0 and 1, at the pulse ω_0 for which the phase of the open loop is equal to 0° (horizontal line in blue on the phase diagrams of Figures 4.12.a and 4.12. b), the open loop gain value is greater than 1 (i.e. 0 dB).

As a reminder, the analysis of the stationary periodic system presented in Chapter 3 shows that for a constant pressure P_m at the entrance of the mouthpiece (that is to say at the level of the artificial mouth) belonging to a very precise interval, the pulsation ω_0 (for which the phase $\phi(\omega_0)$ is zero) is very close to the pulsation ω_{pi} of the mode i concerned. To illustrate graphically the search for the value of ω_0, the condition $\phi(\omega_0) = 0$ is rewritten in the form:

$$\phi(\omega_0) = 0 \quad \Rightarrow \quad \frac{\pi}{2} + \arg Y_{in}(j\omega_0) = \tau\,\omega_0 \ , \tag{4.27}$$

the solution ω_0 resulting from the intersection of the plots associated with the expressions located to the right and to the left of the equal sign of relation (4.27).

Thus, Figure 4.15 presents the frequency responses of $\pi/2 + \arg(Y_{in}(j\omega))$ for five values of the order m, as well as the line associated with the expression $\tau\,\omega$ for:

- **example 1** where P_m = 400 Pa (right in blue Figure 4.15.a) and where mode 1 is concerned (ω_{p1} = 3 639 rad/s, is 579.5 Hz), the solution being ω_0 = 3 577 rad/s (570 Hz);

- **example 2** where P_m = 1000 Pa (right in purple Figure 4.15.b) and where mode 2 is concerned (ω_{p2} = 7 218 rad/s, is 1 149 Hz), the solution being ω_0 = 7 096.4 rad/s (1 130 Hz).

Finally, Figure 4.16 shows for the two examples P_m = 400 Pa (___) and P_m = 1 000 Pa (___), the variation of the open loop gain $\beta(\omega_0)$ in dB scale (Figure 4.16.a) and in linear scale (Figure 4.16.b) as a function of the fractional order m between 0 and 1 on a linear scale.

Observation of these plots leads to two remarks:

- for a given order m, the value of the open loop gain $\beta(\omega_0)$ greater than unity increases with the pressure P_m;

- for a given pressure P_m, the curves of $\beta(\omega_0)$ as a function of the order m show a different local minimum depending on the value of P_m.

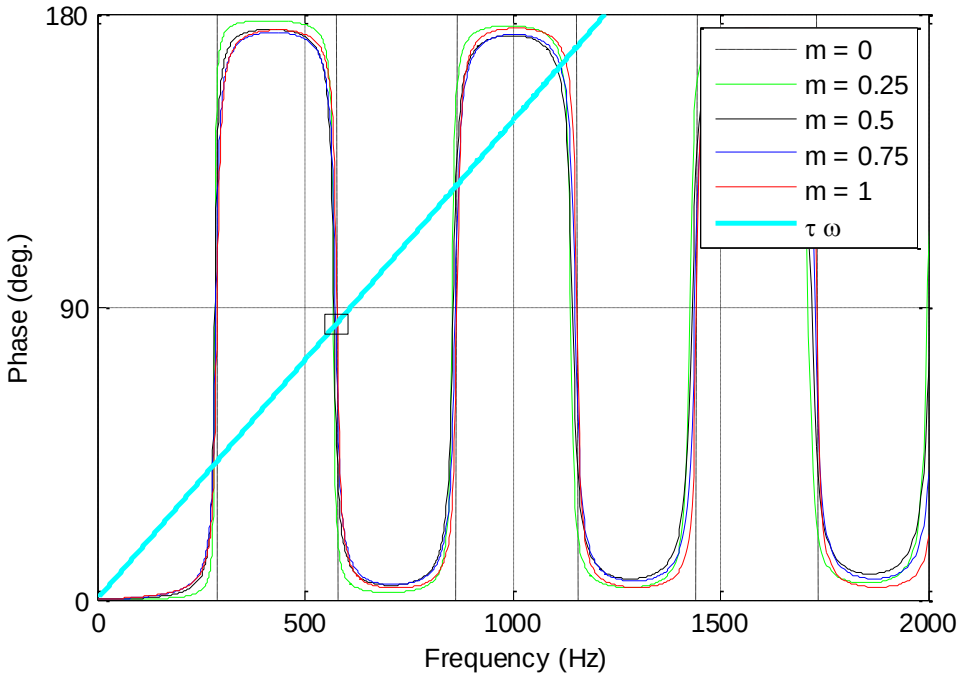

(a)

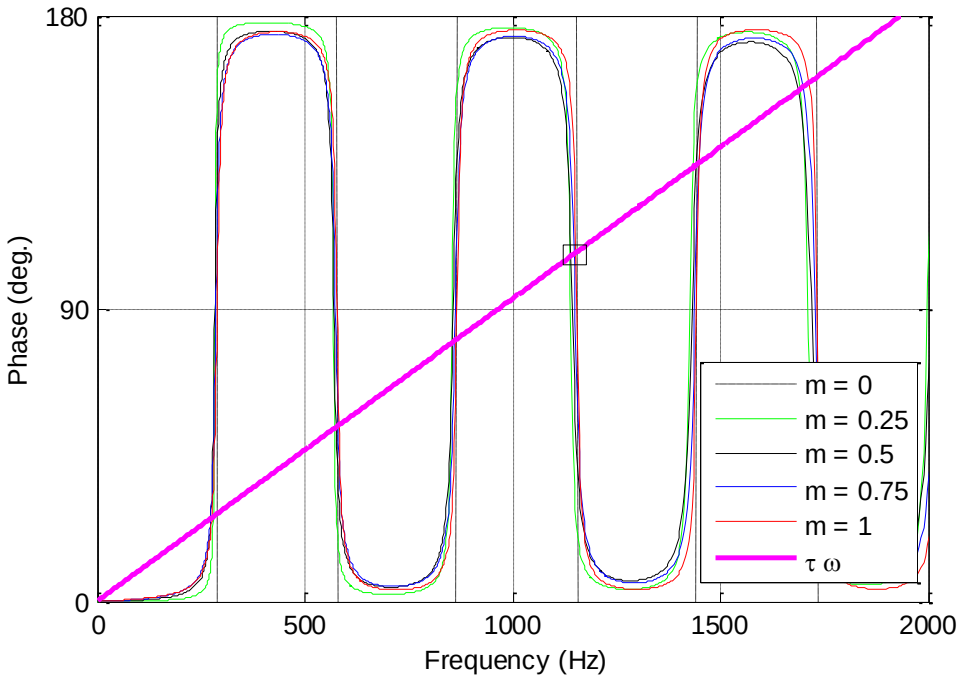

(b)

Figure 4.15 – For P_m = 400 Pa (a) and for P_m = 1000 Pa (b), plots of the line $\tau\ \omega$ and the frequency responses $\pi/2 + arg(Y_{in}(j\omega))$ for 5 values of the order m (0; 0.25; 0.5; 0.75; 1). The solution ω_0 results from the intersection of these two paths which is marked in the figure by a small rectangle

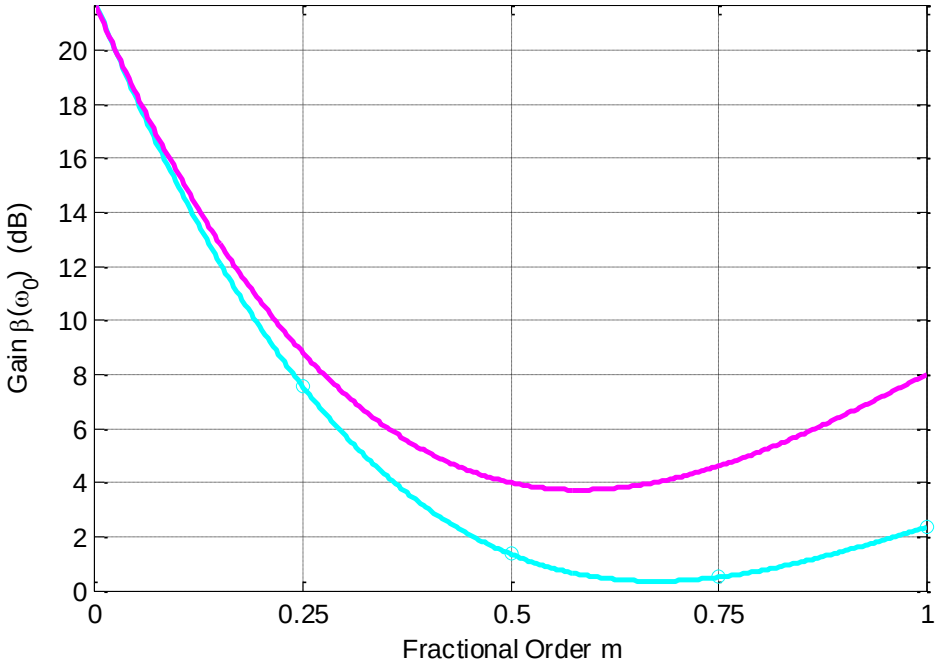

(a)

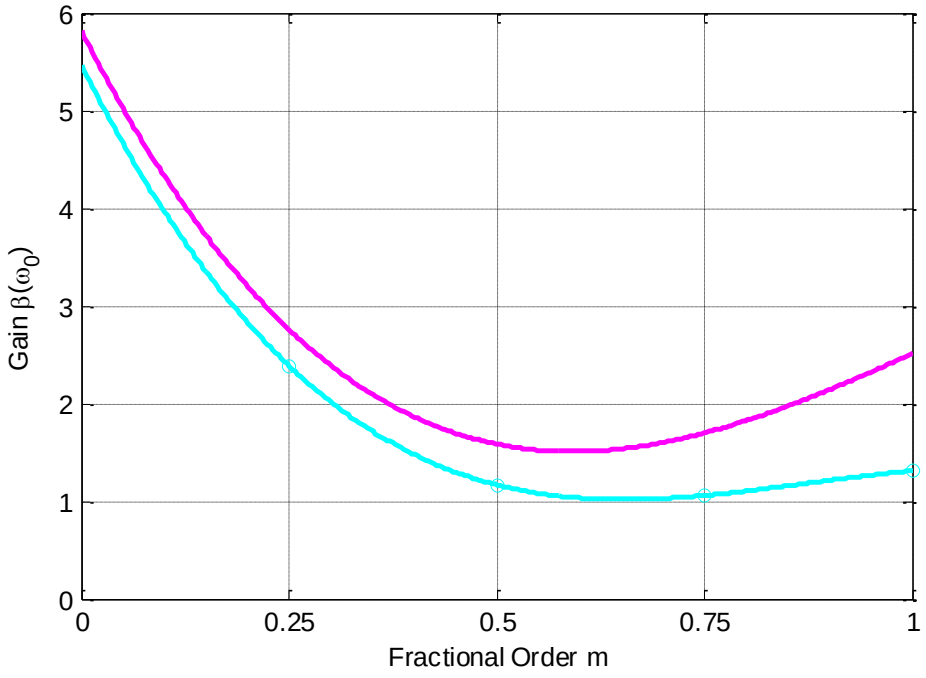

(b)

Figure 4.16 – For P_m = 400 Pa (——) and for P_m = 1000 Pa (——), variation of the open loop gain $\beta(\omega_0)$ in dB scale (a) and in linear scale (b) as a function of the order m

4.4 - Time Domain Illustration of the Influence of Fractional Order

As a reminder (see Chapter 3), the time simulations carried out at P_m = cst reveal three phases:

- ***phase 1:*** start-up with a convergent transient system;

- ***phase 2:*** divergent transient system;

- ***phase 3:*** stationary periodic system.

The objective of this paragraph is to illustrate through time simulation the influence of order *m* on the periodic system of phase 3.

Thus, for this periodic system of phase 3, Figures 4.17 to 4.19 show for:

- the two pressures P_m = 400 Pa (example 1) and P_m = 1000 Pa (example 2)

- and the five values of the order *m* (0; 0.25; 0.5; 0.75; 1),

time responses:

- transverse displacement $\eta(w, t)$ of the jet (Figure 4.17),

- the pressure $\Delta p(t)$ at the input of the resonator (Figure 4.18),

- the acoustic speed $v_{ac}(t)$ (Figure 4.19).

To help the reader to identify the variables $\eta(w,t)$, $\Delta p(t)$ and $v_{ac}(t)$, the functional diagram of the recorder is recalled at the beginning of each of these figures with the concerned variable in red.

Observation of all of these time responses leads to the following remarks.

For a given pressure P_m and for the five values of the order *m* (0; 0.25; 0.5; 0.75; 1), the amplitudes of the time responses are all maximum for *m* = 0 (conservative case) and minimum for an order *m* included between 0.5 and 0.75.

Although one cannot analytically establish a link between open-loop behavior and that observed in closed-loop due to the non-linear character, a trend emerges regarding the influence of the order *m* on the amplitudes of the time responses. Indeed, we observe in the time domain a similarity with the influence of the order *m* on the open loop gain $\beta(\omega_0)$ (Figure 4.16). An analysis based on the method of the first harmonic or a decomposition in series of Volterra, for example, is a prospect which should make it possible to confirm this tendency.

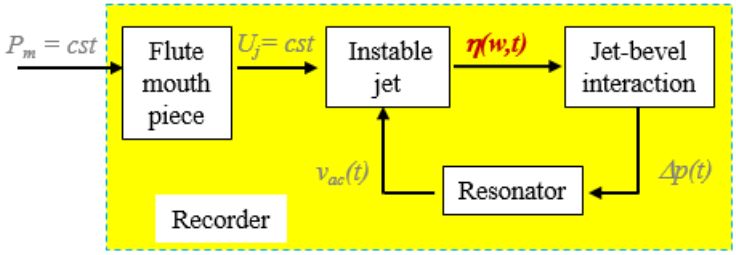

(a)

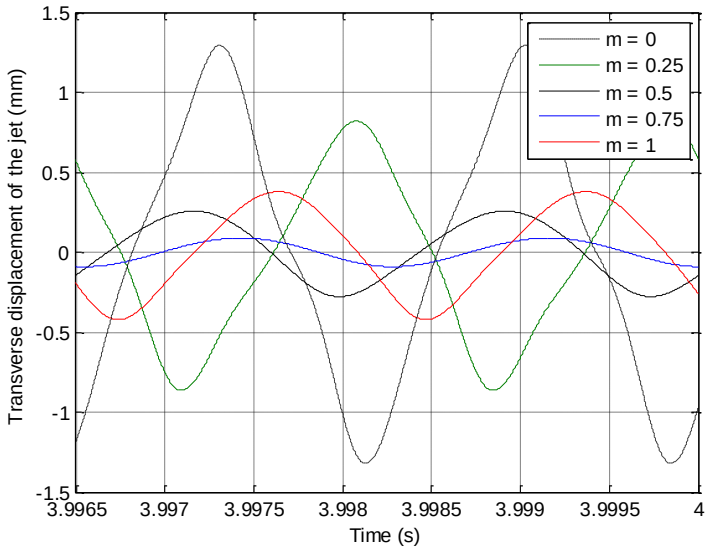

(b)

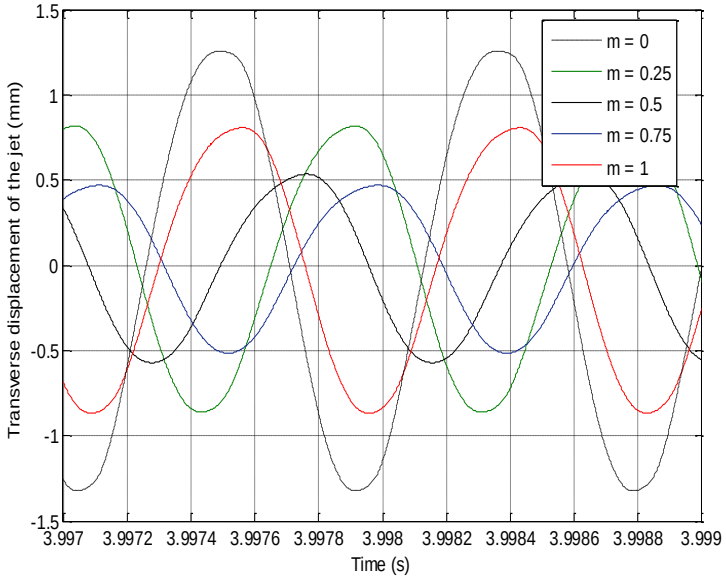

(c)

Figure 4.17 – Time responses of the transverse displacement *η(w, t)* of the jet (a) for 5 values of the order *m* (0; 0.25; 0.5; 0.75; 1), for a pressure P_m = 400 Pa (b) and P_m = 1000 Pa (c)

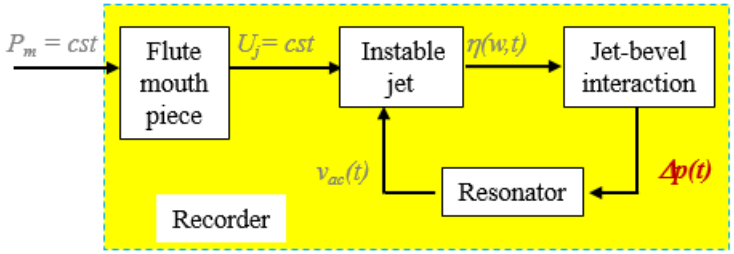

(a)

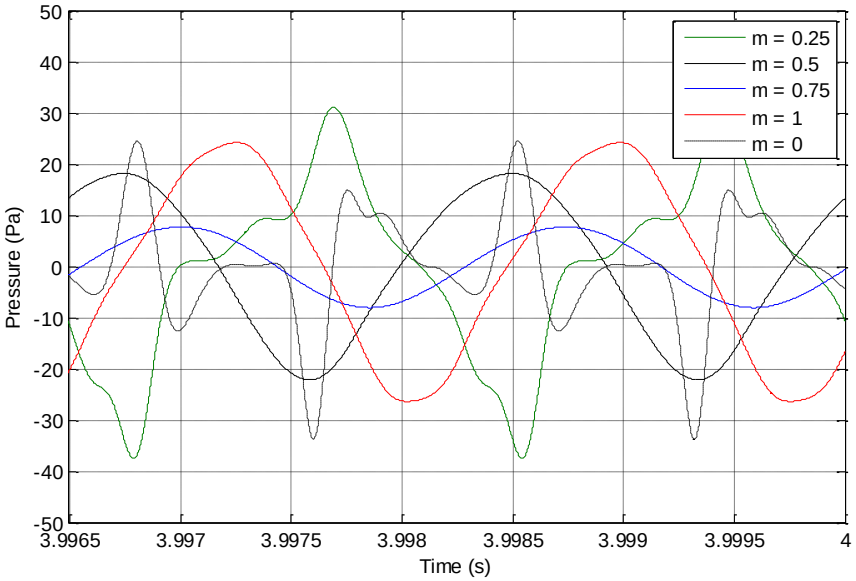

(b)

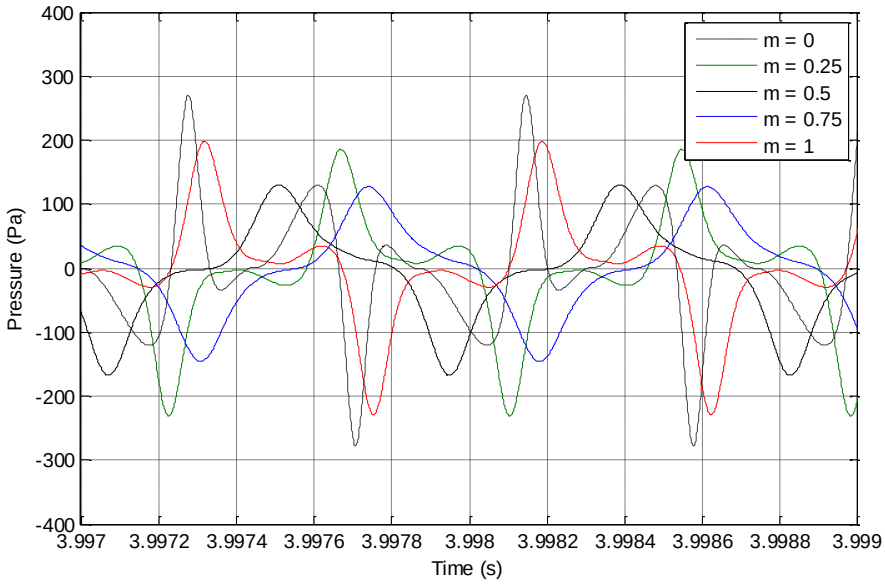

(c)

Figure 4.18 – Time responses of the pressure $\Delta p(t)$ at the input of the resonator (a) for 5 values of the order m (0; 0.25; 0.5; 0.75; 1), for a pressure P_m = 400 Pa (b) and P_m = 1000 Pa (c)

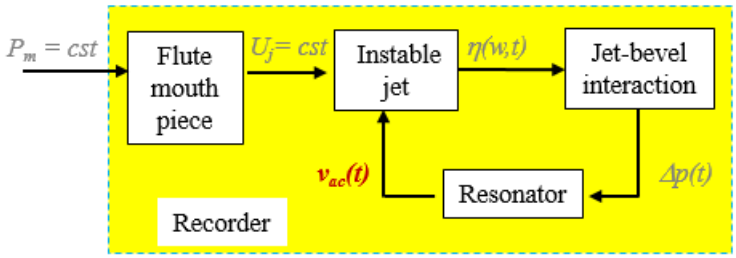

(a)

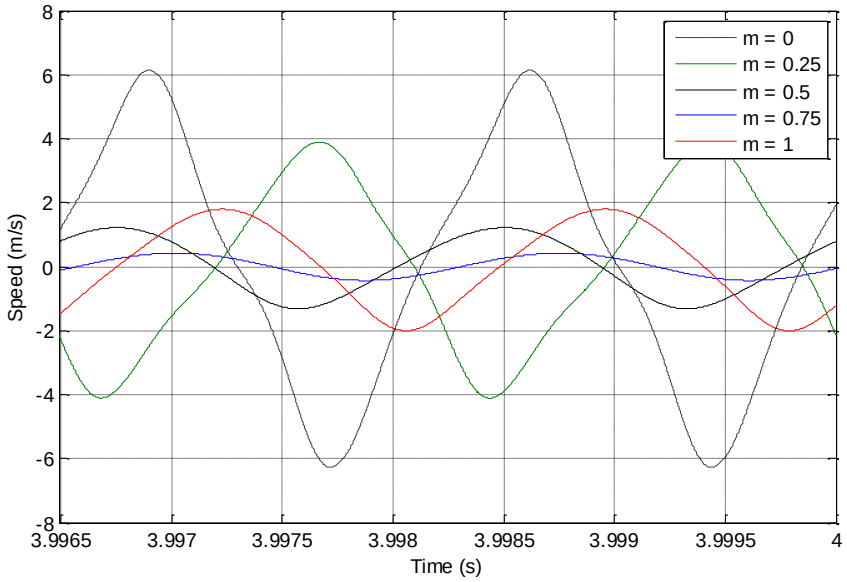

(b)

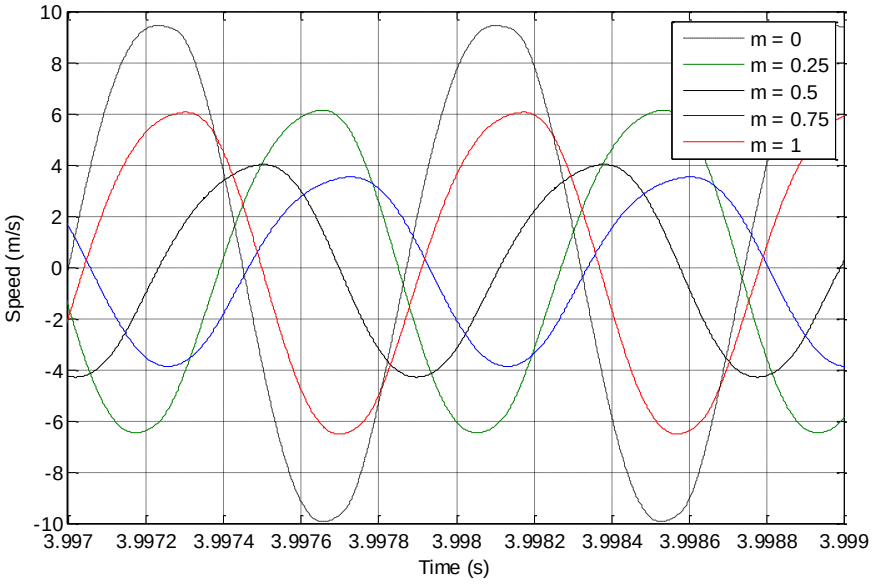

(c)

Figure 4.19 – Time responses of the acoustic velocity $v_{ac}(t)$ (a) for 5 values of the order m (0; 0.25; 0.5; 0.75; 1), for a pressure P_m = 400 Pa (b) and P_m = 1000 Pa (c)

4.5 – Conclusion

One of the most important contributions of this chapter is related to the impedance of the resonator with the development of a method in several stages allowing to pass from the form $Y_{in}(s)$ (relation (4.1)) from Chapter 2 to the form $Y_N(s)$ (relation (4.5)).

Indeed, even if the form $Y_{in}(s)$ remains the reference for the plot of the frequency responses, the form $Y_N(s)$ makes it possible to reveal in an explicit way the parameters ω_{zi}, ζ_{zi}, ω_{pi}, ζ_{pi} which characterize the resonator modes.

The step of determining the constants c_{zi} and c_{pi} (relations (4.12)) makes it possible to define each cell of rank i from the 4 parameters ω_{z1}, ζ_{z1}, ω_{p1}, ζ_{p1} of the cell of rank 1 (obtained using an analytical development: Appendix A) and the 2 factors α_i and η_i (relations (4.19)) of the cell of rank i (obtained numerically).

This method, allowing to switch from the form $Y_{in}(s)$ to the form $Y_N(s)$, facilitates the analysis of the influence of the order m. Thus, it is demonstrated that the order m:

- has no influence on the pulsations ω_{zi} and ω_{pi},

- has an influence on the damping factors ζ_{zi} and ζ_{pi}.

More precisely, for a given rank i and for a variation of the order of m from 0 to 1, the damping factors are zero for $m = 0$ (conservative case), go through a maximum, then decrease. In addition, for a fixed order m, the damping factors decrease with rank i.

Note that the expressions (4.8) of ζ_{zi} and ζ_{pi} clearly show that for a given rank i and an order m, the damping factors are all the greater (and therefore the visco-thermal losses) as the length L of the acoustic tube is large and its radius r is small.

Finally, the analysis of the influence of the order m on the conditions of existence of the stationary periodic system observed in the time domain is an important contribution which completes the first analysis presented in Chapter 3. Indeed, these conditions are reflected in open loop by a gain $\beta(\omega_0)$ strictly greater than the unit with the pulsation ω_0 for which the phase $\phi(\omega_0)$ (of the open loop) is null. Thus, for a given order m, the value of the open loop gain $\beta(\omega_0)$ (greater than unity) increases with the pressure P_m at the mouthpiece input (i.e. in the artificial mouth) and for a given pressure P_m, the curves of $\beta(\omega_0)$ as a function of the order m have a different local minimum depending on the value of P_m.

General Conclusion and Perspective

The interpretation and discussion of the main results presented in this thesis are the subject of the general conclusion.

Chapter 1 constitutes the first essential modeling step for the reader unfamiliar with wind instruments. Indeed, due to its structuring and its didactic progression, it allows to "soak up" the dynamic behavior of an acoustic tube of constant radius including the effect of visco-thermal losses due to the boundary layers in the vicinity of the walls. The ***knowledge model*** used in this work, called Webster-Lokshin 1D, is mono-spatial dependent. It characterizes the linear propagation of acoustic waves in axially symmetrical tubes taking into account visco-thermal losses. Thus, in an axisymmetric tube of constant section, the sound pressure and the sound flow rate are governed by the horn equation, known as Webster-Lokshin, and the Euler equation. This dissipative model includes a term that involves a fractional derivation of order $m = 0.5$. The classical resolution in the operational domain of the system of partial differential equations leads to the analytical expression of the acoustic impedance and admittance of the tube as a function of its length L, of its radius r and of the position x of the tube point considered.

One of the contributions of this chapter is the introduction of an extension of the fractional expression used to take into account visco-thermal losses where the order m is usually equal to 0.5. This extension makes it possible to consider an uncertainty of the order m, whose domain bounds are 0 (conservative system) and 1. Another contribution is the introduction of a system vision aiming to causally decompose the global model into sub models, to facilitate analysis in the frequency domain. One of the conclusions of this frequency analysis is that the fractional model can be simplified over the range [20; 20,000] Hz audible frequencies. Finally, for the simulation in the time domain, two rational forms composed of an integrator of order one and N cells of the second order, one in cascade and the other in parallel, are introduced as a ***model of behavior***. The parametric values of the rational cascade form are determined using the ***Frequency Domain System Identification*** (FDSI) module of the CRONE Toolbox with the frequency response of the ***knowledge model*** as target. As for the parametric values of the parallel form, they are obtained by a decomposition into simple elements of the cascade form.

Chapter 2 falls within the framework of the dynamics of complex systems. Indeed, the self-oscillation mechanism, characterized by the ability of the instrument to produce an acoustic wave from a stationary or quasi-stationary energy source with respect to the acoustic variables, is inseparable from the non-nature. linearity of the exciter and its coupling with the resonator. This phenomenon results from the oscillation of a naturally unstable air jet around a bevel. Thus, the self-oscillation mechanism relies on a synchronization of the oscillation of the jet and the acoustic waves. The jet-bevel system must therefore excite the resonator at the periodicity of the acoustic field.

From a bibliographic synthesis, a complete nonlinear model frequently used in the literature is developed in this chapter. Faced with the poor digital conditioning of this model, a solution is proposed in order to be able to develop a digital simulator programmed under MatLab / Simulink. This solution constitutes a first contribution in this chapter. A scenario is then defined while respecting, not only the domain of validity of the nonlinear model, but also the values of pressure attainable experimentally by the artificial mouth presented in chapter 4. The detailed analysis of the simulated time responses makes it possible, in particular, to observe that the variations of a certain number of physical quantities (pressure at the input of the resonator, acoustic speed, etc.) are small and around zero. This observation allows us to legitimize the realism of the hypothesis of small variations. Thus, two linearized models, one for the analysis of ***phase 1*** (start of the simulation), the other for that of ***phase 3*** (self-oscillations) are developed and used to better understand the phenomena brought to light. clearance, especially the self-oscillation conditions.

Chapter 3 presents the model-based design approach of an artificial mouth, its realization and the experimental characterization of each of its components, in order to adjust the nonlinear models integrated in the digital simulator associated with this part. The use of an artificial mouth, in the context of comparative studies of the complex dynamic phenomena present in wind instruments, is necessary to ensure reproducibility of test conditions that are difficult to achieve with a human being. This three-step engineering approach is essential to fully understand the non-linear behavior of each component, define the limits of their operating range and establish the influence of different physical quantities on the pressure at the mouthpiece inlet. Note that this last point is essential to understand the need for a pressure regulation loop. Thus, the first step in this approach was the development of a first simulator on the basis of a bibliographic synthesis concerning artificial mouths used in musical acoustics. This first simulator made it possible to fully understand the operation of such a system, thus facilitating the choice and sizing of the components of the regulation loop (the flow servo valve, the sensors (flow, pressure and temperature), the volume of the pneumatic capacity, etc.), as well as the summary of the pressure control (feedforward and feedback parts). The second step was the realization of the test bench with the assembly of the various parts and their tuning. Finally, the third step consisted of a second iteration, not only of modeling applied precisely to the experimental device produced, but also of synthesis of the pressure control. This step lead to a second digital simulator. The latter was the subject of a retiming from comparisons between experimental and simulation results. Thus, for a real recorder (made of plastic with a length of the resonator L = 30 cm, an average radius r = 5 mm, a fractional order associated with visco-thermal losses m = 0.5, ...), the simulator reproduces with a good precision the study conditions specified in chapters 2 and 3. This very real behavior (reproduced in simulation) is considered in chapter 4 as the nominal reference behavior.

Finally, ***Chapter 4*** brings together the developments and results of the first three chapters to deepen the analysis of the influence of the fractional order m on the mechanism leading to the stationary periodic system.

One of the strong points of this chapter concerns the development of a method allowing to pass from the initial fractional form of the $Y_{in}(s)$ impedance from chapter 1, where the modes of the resonator ***appear implicitly*** through the periodicity from the *tanh(.)* function, to another fractional form $Y_N(s)$ where, on the contrary, the modes of the resonator ***appear explicitly*** through the product of N fractional cells of order 2. Indeed, even if the form $Y_{in}(s)$ remains the reference for the plot of the frequency responses, the form $Y_N(s)$ makes it possible to reveal in an explicit way the parameters ω_{zi}, ζ_{zi}, ω_{pi}, ζ_{pi} which characterize the modes of the resonator. This method facilitates the analysis by showing that the order m has no influence on the pulsations ω_{zi} and ω_{pi}, but that it does have an influence on the damping factors ζ_{zi} and ζ_{pi}. For a given rank i and for a variation of the order of m from 0 to 1, the damping factors are zero for $m = 0$ (conservative case), go through a maximum, then decrease. In addition, for a fixed order m, the damping factors decrease with rank i. Finally, the analysis of the influence of the order m on the conditions of existence of the stationary periodic system observed in the time domain using the complete simulator (artificial mouth + nonlinear exciter + resonator) is an important contribution. which completes the first analysis made in chapter 2. Indeed, these conditions result in open loop by a gain $\beta(\omega_0)$ strictly greater than the unit with the pulsation ω_0 for which the phase $\phi(\omega_0)$ (of the open loop) is zero. Thus, for a given order m, the value of the open loop gain $\beta(\omega_0)$ (greater than unity) increases with the pressure P_m at the entrance to the mouthpiece (i.e. in the artificial mouth) and for a given pressure P_m, the curves of (ω_0) as a function of the order m have a different local minimum depending on the value of P_m.

More generally in terms of fractional models, this study of the influence of order m on visco-thermal losses leads to a finding similar to that already made in other fields. Indeed, the main interest of the fractional form lies in the parametric parsimony, that is to say the capacity possessed by the integro-differential operator of non-integer order to model with a minimum of parameters the greatest number of dynamic phenomena.

The medium-term outlook falls directly within the continuity of the work in progress, that is to say within the framework of the dynamics of complex systems.

From a modeling point of view, a first perspective concerns the introduction of the extension of the fractional expression used to take account of visco-thermal losses in the more general framework of the pavilion equation as encountered in the literature. wind instruments. Indeed, in this case, the radius of the acoustic tube depends on the longitudinal position x of the point considered within the resonator. In addition, its apparent length may vary depending on the number of closed holes. Thus, taking into account a fractional order m between 0 and 1, associated with variations in radius and apparent length, should make it possible to extend the domain of validity of the model developed in Chapter 1.

At the same time, the increase in the field of study defined in chapters 2 and 4 by considering a pressure P_m at the entrance to the mouthpiece, no longer constant, but variable (like that generated by a musician) constitutes a second perspective. To achieve this goal, it is

necessary to solve the problem of causality due to the presence of a shunt in the model used to describe the interaction between the air jet and the bevel. The solution proposed in this thesis, namely the use of a frequency bounded derivation operator, only makes it possible to better condition the model numerically for a constant pressure P_m from the initial moment of the simulation.

From a systems theory point of view, an interesting perspective is the definition of a fractional resonator with one degree of freedom (1 dof). The first step will consist in defining its structure from the decomposition into simple elements of the product of the N fractional cells of order 2 present in the expression of the acoustic impedance $Y_N(s)$ introduced in chapter 4. Then, the structure being perfectly defined, the study of the fundamental properties of this fractional resonator with 1 dof will constitute the second stage. The progression proposed within the framework of systems whose dynamics are described by differential equations of integer orders, with first the study of systems with 1 dof, then that of systems with q dof which in the modal space are in the form of q 1-DOF systems, will be generalized to SDNE (Non-Integer Derivative Systems which include the dynamic systems of integer orders).

Finally, ***from an experimental point of view*** at the level of the artificial mouth, the integration of components designed specifically for the medical sector, in particular those used in automatic respiratory assistance devices (servo valves, sensors, etc.), should make it possible to improve the performance of the test bench.

Appendix -A

From the initial form of the fractional impedance $Y_{in}(s)$ from chapter 1 to its fractional form $Y_N(s)$ from chapter 4

This appendix presents the details of the analytical developments allowing to pass from the initial form of the fractional impedance $Y_{in}(s)$ of chapter 1 to its form $Y_N(s)$ of chapter 4.

Thus, as a reminder and for the field of study defined within the framework of this thesis work, the input admittance $Y_{in}(s)$ of the acoustic tube (resonator) of length L and radius r has the expression:

$$Y_{in}(s) = \frac{S}{Z_{ac}} I_m(s) \frac{1}{\tanh\left(z(s)\right)} \quad , \tag{A.1}$$

with

$$I_m(s) = \sqrt{\frac{1+\left(\frac{s}{\omega_{r,m}}\right)^m}{\left(\frac{s}{\omega_{r,m}}\right)^m}} \tag{A.2}$$

and

$$z(s) = \left(\frac{s}{\omega_L}\right) \sqrt{\frac{1+\left(\frac{s}{\omega_{r,m}}\right)^m}{\left(\frac{s}{\omega_{r,m}}\right)^m}} \quad . \tag{A.3}$$

The expression (A.1) of $Y_{in}(s)$ can be put in a form $Y_N(s)$ composed of an integrator of order 1 in cascade with N fractional cells of order 2, namely:

$$Y_{in}(s) = \lim_{N\to\infty} Y_N(s) \quad , \tag{A.4}$$

with

$$Y_N(s) = \frac{Y_0}{s} \prod_{i=1}^{N} \left(\frac{1+2\zeta_{zi}\left(\frac{s}{\omega_{zi}}\right)^{2-m}+\left(\frac{s}{\omega_{zi}}\right)^2}{1+2\zeta_{pi}\left(\frac{s}{\omega_{pi}}\right)^{2-m}+\left(\frac{s}{\omega_{pi}}\right)^2} \right) \quad , \tag{A.5}$$

where

$$Y_0 = \frac{S}{\rho_a L} \tag{A.6}$$

and

$$\begin{cases} \omega_{zi} = c_{zi}\,\omega_L \quad ; \quad \zeta_{zi}(m) = \dfrac{2K_0}{r}\left(\dfrac{L}{c_{zi}}\right)^m m \\ \omega_{pi} = c_{pi}\,\omega_L \quad ; \quad \zeta_{pi}(m) = \dfrac{2K_0}{r}\left(\dfrac{L}{c_{pi}}\right)^m m \end{cases} , \tag{A.7}$$

where c_{zi} and c_{pi} are constants resulting from the procedure allowing to pass from $Y_{in}(s)$ to $Y_N(s)$ This procedure consists of 4 steps:

- **Step 1:** finite expansion of the function *tanh(z)* into a continuous fraction in *z*;

- **Step 2:** reduction of the continuous fraction to a ratio of two polynomials in *z*;

- **Step 3:** factorization of each polynomial in *z*;

- **Step 4:** rewriting $Y_{in}(s)$ in the form $Y_N(s)$, namely an integrator of order 1 in cascade with a product of *N* fractional cells of order 2.

Step 1

The finite expansion of the function *tanh(z)* into a continuous fraction in *z* is given by (Wyman & Wyman, 1985)

$$tanh(z) = \cfrac{z}{1+\cfrac{z^2}{3+\cfrac{z^2}{5+\cfrac{z^2}{7+\cfrac{z^2}{9+\ldots}}}}} \quad , \tag{A.8}$$

or, by adopting a more condensed writing convention,

$$tanh(z) = \frac{z}{|1} + \frac{z^2}{|3} + \frac{z^2}{|5} + \frac{z^2}{|7} + \frac{z^2}{|9} + \ldots \quad . \tag{A.9}$$

Step 2

The reduction of the continued fraction defined by relation (A.8) leads to an expression in the form of a product of the variable *z* and a ratio of two polynomials in *z* voluntarily limited to an order of 4/4 for the analytical developments, namely:

$$tanh(z) = z\left(\frac{num(z)}{den(z)}\right) \quad , \tag{A.10}$$

with

$$\begin{cases} num(z) = n_0 + n_2\, z^2 + n_4\, z^4 \\ \\ den(z) = d_0 + d_2\, z^2 + d_4\, z^4 \end{cases} \quad , \tag{A.11}$$

$$\text{or} \begin{cases} n_0 = 3\times5\times7\times9 = 945 \\ n_2 = 3\times5 + 7\times9 + 3\times9 = 105 \\ n_4 = 1 \end{cases} \quad \text{and} \quad \begin{cases} d_0 = 3\times5\times7\times9 = 945 \\ d_2 = 3\times5 + 7\times9 + 3\times9 + 5\times7\times9 = 420 \\ d_4 = 1 + 5 + 9 = 15 \end{cases} \quad . \tag{A.12}$$

Step 3

Factoring each polynomial in z requires finding their roots. To do this, we perform the change of variable by setting $X = z^2$, hence the system to be solved:

with
$$\begin{cases} num(z) = 0 \quad \Rightarrow \quad n_0 + n_2\, X + n_4\, X^2 = 0 \\ \\ den(z) = 0 \quad \Rightarrow \quad d_0 + d_2\, X + d_4\, X^2 = 0 \end{cases} . \tag{A.13}$$

Solving this system made up of two quadruple equations in X does not present any particular difficulty. Each polynomial in X has two distinct real roots, namely:

- for the numerator:

$$\begin{cases} X_{n1} = -95 \\ \\ X_{n2} = -9.94 \end{cases} ; \tag{A.14}$$

- for the denominator:

$$\begin{cases} X_{d1} = -25.533 \\ \\ X_{d2} = -2.467 \end{cases} . \tag{A.15}$$

Finally, the expression (A.10) of *tanh(z)* is rewritten as:

$$tanh(z) = z \left(\frac{\left(z^2 + 9.94\right)\left(z^2 + 95\right)}{15\left(z^2 + 2.467\right)\left(z^2 + 25.533\right)} \right) . \tag{A.16}$$

Step 4

Finally, knowing that

$$z(s) = \left(\frac{s}{\omega_L} \right) \sqrt{\frac{1 + \left(\frac{s}{\omega_{r,m}} \right)^m}{\left(\frac{s}{\omega_{r,m}} \right)^m}} , \tag{A.17}$$

the introduction of the expression (A.17) of *z(s)* in the relation (A.16) of *tanh(z)* leads to:

$$tanh(z)=\left(\left(\frac{s}{\omega_L}\right)\sqrt{\frac{1+\left(\frac{s}{\omega_{r,m}}\right)^m}{\left(\frac{s}{\omega_{r,m}}\right)^m}}\right)\times$$

$$\left(\frac{\left(\left(\left(\frac{s}{\omega_L}\right)\sqrt{\frac{1+\left(\frac{s}{\omega_{r,m}}\right)^m}{\left(\frac{s}{\omega_{r,m}}\right)^m}}\right)^2+9.94\right)\left(\left(\left(\frac{s}{\omega_L}\right)\sqrt{\frac{1+\left(\frac{s}{\omega_{r,m}}\right)^m}{\left(\frac{s}{\omega_{r,m}}\right)^m}}\right)^2+95\right)}{15\left(\left(\left(\frac{s}{\omega_L}\right)\sqrt{\frac{1+\left(\frac{s}{\omega_{r,m}}\right)^m}{\left(\frac{s}{\omega_{r,m}}\right)^m}}\right)^2+2.467\right)\left(\left(\left(\frac{s}{\omega_L}\right)\sqrt{\frac{1+\left(\frac{s}{\omega_{r,m}}\right)^m}{\left(\frac{s}{\omega_{r,m}}\right)^m}}\right)^2+25.533\right)}\right). \qquad \text{(A.18)}$$

Taking into account the expression (A.1) of $Y_{in}(s)$, where $I_m(s)$ is defined by:

$$I_m(s)=\sqrt{\frac{1+\left(\frac{s}{\omega_{r,m}}\right)^m}{\left(\frac{s}{\omega_{r,m}}\right)^m}}\quad , \qquad \text{(A.19)}$$

the introduction of the relation (A.18) in the expression (A.1) allows (after some manipulations and simplifications) the transition to the form $Y_N(s)$ for $N = 2$, that is:

$$Y_{N=2}(s)=\frac{Y_0}{s}\prod_{i=1}^{2}\left(\frac{1+2\zeta_{zi}\left(\frac{s}{\omega_{zi}}\right)^{2-m}+\left(\frac{s}{\omega_{zi}}\right)^2}{1+2\zeta_{pi}\left(\frac{s}{\omega_{pi}}\right)^{2-m}+\left(\frac{s}{\omega_{pi}}\right)^2}\right)\quad , \qquad \text{(A.20)}$$

with
$$\begin{cases} c_{z1}=\sqrt{2.467} \\ c_{p1}=\sqrt{9.94} \end{cases}. \qquad \text{(A.21)}$$

with the generalization of the relation (A.20) to any N is developed in chapter 4.

References

Abou Haidar, G., Abi Zeid Daou, R., & Moreau, X. (2019). Modelling and Identification of the Musicians Blowing Part and the Flute Musical Instrument. *Fourth International Conference on Advances in Computational Tools for Engineering Applications.* Zouk, Lebanon.

Abou Haidar, G., Moreau, X., & Abi Zeid Daou, R. (2021). Identification and Analysis of the Effects of the Viscous Thermal Losses in the Flute Musical Instruments. *Fractal Fract. 2021*, Volume 5, Issue 1, 11: fractalfract-1030736; doi: 10.3390/f.

Abou Haidar., G., Abi Zeid Daou, R., & Moreau, X. (2018). Robust Control of an Artificial Mouth for a Wind Musical Instrument. *International Conference on Fractional Differentiation and its Applications.* Jordan.

Andréa, D., & Matignon , D. (1995). Spectral and time-domain consequences of an integro-differential perturbation of the wave PDE. *3rd WAVES conference.* Mandelieu, France.

Assaf, R. (2015). *Modélisation des phénomènes de diffusion thermique dans un milieu fini homogène en vue de l'analyse, de la synthèse et de la validation de commandes robustes.* Bordeaux: Université de Bordeaux.

Auvray, R. (2010). *Fréquence de jeu des instruments à embouchure de flutes.* Université Pierre et Marie Curie: Mémoire de stage de Master 2 Sciences et technologie.

Auvray, R., Fabre, B., & Lagrée, P. (2012). Regime change and oscillation thresholds in recorder-like instruments. *Journal of the Acoustical Society of America, 131*(4), 1574–1585.

B Fabre, A. H. (1996). Vortex shedding in steady oscillation of a flue organ pipe . *Acta Acustica united with Acustica*, 82(6):863–877 .

Bernoulli, D. (1762). *Sur le son et sur les tons des tuyaux d'orgue differemment construits.* Paris: Mémoires de l'Académie Royale des Sciences.

Blanc, F. (2009). *Production de son par couplage écoulement/résonateur : étude des paramètres de facture des flûtes par expérimentations et simulations numériques d'écoulements.* Paris: Université Paris VI.

Boutin, H., Le Conte, S., Le Carrou , J., & Fabre, B. (2018). Modèle de propagation acoustique dans un tuyau cylindrique à paroi poreuse. *Congrès Français d'Acoustique.* Le Havre.

Chaigne, A., & Kergomard, J. (2013). Acoustique des instruments de musique. *Edition Belin, 2ème édition revue et augmentée, Paris, 2013.* Paris.

Chaigne, A., & Kergomard, J. (2008). *Acoustique des instruments de musique.* Paris: Belin.

Coltman, J. (1968). Sounding mechanism of the flute and organ pipe. *The Journal of the Acoustical Society of America, 44*, 983–992.

Coltman, J. (1976). Jet drive mechanisms in edge tones and organ pipes. *Journal of the Acoustical Society of America,, 60*(3), 725–733.

Cuadra, P. d. (2005). *The sound of oscillating air jets: Physics, modeling and simulation in flute-like instruments.* Stanford University: Thèse de doctorat, .

Cuadra, P., Vergez , C., & Fabre, B. (2007). Visualization and analysis of jet oscillation under transverse acoustic perturbation. *Journal of Flow Visualization and Image Processing*, 14(4):355–374.

Debut, V. (2004). Deux études d'un instrument de musique de type clarinette : analyse des fréquences propres du résonateur et calcul des auto-oscillations par décomposition modale. *PhD Thesis, Université Aix-Marseille II, 2004.* Marseille.

Ducasse, E. (1990). Modélisation d'instruments de musique pour la synthèse sonore : application aux instruments à vent. *Journal de Physique Colloques, 51*, 837-840.

Ducasse, E. (2001). *Modélisation et simulation dans le domaine temporel d'instruments à vent à anche simple en situation de jeu : méthodes et modèles.* Maine: Université du Maine.

Elder, S. (1973). On the mechanism of sound production in organ pipes. *The Journal of the Acoustical Society of America, 54*, 1554–1564.

F Blanc, V. F. (2014). Modeling the receptivity of an air jet to transverse acoustic disturbance with application to musical instruments. *The Journal of the Acoustical Society of America,*, 135(6):3221–3230.

Fabrice, S. (2009). *Émergence des auto-oscillations dans un instrument de musique à anche simple.* AIX-MARSEILLE I: UNIVERSITÉ DE PROVENCE.

FactMonster. (2001). *Families of Musical Instruments*. (KidsSAFE Seal Program) Retrieved 10 28, 2018, from www.factmonster.com

Falkovich, G. (2011). *Fluid mechanics: A short course for physicists.* Cambridge: University Press.

Ferrand, D., & Vergez, C. (2008). Blowing machine for wind musical instrument: toward a real-time. *in 16th Mediterranean Conference on Control and Automation.* Ajaccio,France.

Ferrand, D., Vergez, C., Fabre , B., & Blanc, F. (2010). High-precision regulation of a pressure controlled artificial mouth : the case of recorder-like musical instruments. *Acta Acustica united with Acustica, Hirzel Verlag,, vol. 96, no. 4*, (pp. pp. 701-712).

Fletcher. (1979). Air flow and sound generation in musical wind instruments. *Annual Review of Fluid Mechanics, 11*, 123-146.

Fletcher, N. H. (1993). Autonomous vibration of simple pressure-controlled valves in gas flows. *Journal of the Acoustical Society of America*, 93(4):2172–2180.

G. Abou Haidar, R. A. (2019). Modelling and Identification of the Musicians Blowing Part and the Flute Musical Instrument. *Fourth International Conference on Advances in Computational Tools for Engineering Applications.* Zouk, Lebanon.

Haddar, H., & Matignon, D. (2008). *Analyse théorique et numérique du modèle de Webster Lokshin.* France: INRIA.

Haddar, H., Hélie, T., & Matignon, D. (2003). A Webster-Lokshin model for waves with viscothermal losses and impedance boundary conditions: strong solutions. *International congress in Mathematical and numerical aspects of wave propagation.* Jyväskylä, Finland.

Hamilton, R. (2019). Coretet: A Dynamic Virtual Musical Instrument for the Twenty-First Century. *IEEE Conference on Virtual Reality and 3D User Interfaces (VR).* Osaka, Japan.

Helie, R., Mignot, R., & Matignon, D. (2011). Simulation en guides d'ondes numériques stables pour des tubes acoustiques à profil convexe. *JESA*, Vol. 45, pp.547-574, ISSN 1269-6935, 2011.

Helie, T. (2003). Modélisation physique d'instruments de musique en systèmes dynamiques et inversion. *JESA, 37*(10), 1305-1310.

Helie, T. (2006). Ondes découplées et ondes progressives pour les problèmes mono-dimensionnels d'acoustique linéaire. *Congrès Français d'Acoustique, CFA'06, Tours, 24-27 Avril 2006.*

Hélie, T., Gandolfi, G., & Hezard, T. (2014). Estimation paramétrique de la perce d'un instrument à vent à partir de la mesure de son impédance d'entrée. *Congrès Français d'Acoustique.* Poitiers.

Heller. (2017). An Augmented Flute for Beginners. *NIME 2017.* Denmark.

Henríquez, V., & Chocano, G. V. (2017). Viscothermal Losses in Double- Negative Acoustic Metamaterials. *Phys. Rev. Applied 8, 014029, 8*, 12.

Hirschberg, B. F. (2000). Physical modeling of flue instruments : A review of lumped models. *Acta Acustica united with Acustica*, 86:599–610.

Howe, M. (1975). Contribution to the theory of aerodynamic sound, with application to excess jet noise and the theory of the flute. *Journal of Fluid Mechanics, 71*, 625–673.

Ivanova, E. (2017). *Identification de systèmes multivariables par modèle non entier en utilisant la méthode des sous-espaces.* Bordeaux: Université de Bordeaux.

Kergomard, A., & Chaigne, J. (2013). *Acoustique des instruments de musique.* Belin (Echelles): 2ème édition revue et augmentée.

Lanusse, P. (1994). *De la commande CRONE de première génération à la commande CRONE de troisième generation.* France: PhD Thesis, Bordeaux I University.

Lanusse, P. (2010). *CRONE Control System Design, a CRONE toolbox for Matlab*. Retrieved from http://www.ims-bordeaux.fr/CRONE/toolbox.

Lefebvre, A. (2011). *Computational Acoustic Methods for the Design of Woodwind Instruments.* Montreal: McGill University.

Lokshin , A., & Rok, V. (1978). *Fundamental solutions of the wave equation with retarded time.* Dokl. Akad. Nauk .

Lopes, N. (2016). *Approche passive pour la modélisation, la simulation et l'étude d'un banc de test robotisé pour les instruments de type cuivre.* Paris: Université Pierre et Marie Curie.

M P Verge, B. F. (1994). Jet formation and jet velocity fluctuations in a flue organ pipe. *The Journal of the Acoustical Society of America*, 95(2):1119–1132.

M P Verge, B. F. (1997). Sound production in recorderlike instruments. I. dimensionless amplitude of the internal acoustic field. *The Journal of the Acoustical Society of America*, 101(5):2914–2924.

Maki-Patola, M. K. (2004). Physics-based modeling of musical instruments for interactive virtual reality. *IEEE Workshop on Multimedia Signal Processing.* Siena, Italy.

Malti, R., & Victor, S. (2015). CRONE Toolbox for system identification using fractional differentiation models. *17th IFAC Symposum on System Identification, SYSID'15, pp. 769-774, Beijing, China, Oct. 2015.* Beijing.

Matignon, D. (2014). *Viscoelastic materials and viscothermal losses.* Toulouse: University of Toulouse.

Matignon, D., Mignot, R., & Helie, T. (2007). Waveguide modeling of lossy flared acoustic pipes: derivation of Kelly-Lochbaum structure for real-time simulations. *IEEE Workshop on Applications of Signal Processing to Audio and Acoustics, New Paltz, NY, Oct. 21-24 2007.* New York.

McIntyre. (1983). On the oscillations of musical instruments. *The Journal of the Acoustical Society of America, 74*(5), 1325-1345.

Meissner, M. (2001). Aerodynamically excited acoustic oscillations in cavity resonator exposed to an air jet . *Acta Acustica united with Acustica*, 88(2):170–180.

Mersenne, M. (1636). *Harmonie Universelle Contenant la théorie et la pratique de la musique.* Paris: Sebastien Cramoisy.

Mignot, R. (2009). *Réalisation en guides d'ondes numériques stables d'un modèle acoustique réaliste pour la simulation en temps réel d'instruments à vent.* Paris: Télécom ParisTech.

Mignot, R., Hélie, T., Matignon, D., & . (2011). From a model of lossy frared pipes to a general framework for simulation of waveguides. *Acta Acustica united with Acustica, 97*(3), 477-491.

Nolle, A. (1998). Sinuous instability of a planar jet: propagation parameters and acoustic excitation. *Journal of the Acoustical Society of America*, 103:3690–3705.

Oustaloup, A. (1991). *La commande CRONE.* Paris: Paris: Hermes.

Oustaloup, A. (1995). *La dérivation non entière : Théorie, synthèse et applications.* Paris: Paris: Hermes,.

P. Lanusse, R. M. (2013). CRONE control system design toolbox for the control engineering community: tutorial and case study. *Philosophical transaction of the royal society* , (pp. vol. 391, pp. 1-14).

Paine, G. (2013). New Musical Instrument Design Considerations. *IEEE MultiMedia , vol. 20, no. 4, p. IEEE MultiMedia .*

Powell, A. (1961). On the edgetone. *The Journal of the Acoustical Society of America,, 33*(4), 395 - 409.

R Auvray, B. F. (2012). Regime change and oscillation thresholds in recorder-like instruments. *Journal of the Acoustical Society of America*, 131(4):1574–1585.

R. Saar, G. L. (2014). Implementing physical models of musical instruments in the TMS320C6748. *6th European Embedded Design in Education and Research Conference (EDERC).* Milano.

Rayleigh, J. (1984). *The theory of sound.* New York: Dover.

Reid, P. G. (2002). *Hydrodynamic stability.* Cambridge: Cambridge university press.

S Terrien, R. A. (2012). *Numerical resolution of a physical model of flute-like instruments : comparison between different approaches.* Nantes, France: In Proceedings of Acoustics 2012.

Ségoufin, C. (2000). *Production du son par interaction écoulement/résonateur acoustique.* Paris: Université Paris VI.

Ségoufin, C. (2000). *Production du son par interaction fluide/ structure/ champ acoustique résonnant : application aux instruments de musique de type flûte à bec.* Paris 6: Thèse de doctorat, Université Pierre et Marie Curie,.

Smith. (2006). A Basic Introduction to Digital Waveguide Synthesis. *Center for Computer Research in Music and Acoustics (CCRMA).* California: CCRMA.

Takanishi, J. S. (2010). Toward understanding the nature of musical performance and interaction with wind instrument-playing humanoids . *19th International Symposium in Robot and Human Interactive Communication.* Viareggio.

Tassart, S. (1999). Modélisation, simulation et analyse des instruments à vent avec retards fractionnaires. *PhD Thesis, Université Paris VI.* Paris.

Terrien, S. (2011). *ANALYSE DE DEUX PHÉNOMÈNES OBSERVÉS SUR BOUCHE ARTIFICIELLE.* Marseille: Université de Provence.

Terrien, S. (2015). *Instruments de la famille des flûtes: analyse des transitions entre régimes.* Aix-Marseille Université: Thèse de doctorat.

Terrien, S., Vergez, C., & Fabre, B. (2013). Flute-like musical instruments: a toy model investigated through numerical continuation. *Journal of sound and vibration,*, 332(1):3833–3848.

Terrien., S. (2014). *Instrument de la famille des flûtes : analyse des transitions entre régimes.* Marseille: Université Aix-Marseille.

V. Chatziioannou, A. H.-V. (2008). An artificial blowing machine to investigate single-reed woodwind instruments under controlled articulation conditions. *174th Meeting of the Acoustical Society of America.* New Orleans, Louisiana.

Verge, M. (1995). *Aeroacoustics of confined jets: with applications to the physical modeling of recorder-like instruments.* Technische Universiteit Eindhoven: Thèse de doctorat.

Verge, M., Hirschberg, A., & Caussé, R. (1997). Sound production in recorder-like instruments. *Journal of the Acoustical Society of America*, 101(5):2925–2939.

Vigué, P., Vergez, C., Lombard, B., & Cochelin, B. (2019). Continuation of periodic solutions for systems with fractional dérivatives. *Nonlinear Dynamics, 95*(1), 479-493.

Wyman, M., & Wyman, B. (1985). An essay on continued fractions. *Math. Systems Theory*, 18, 295–328 https://doi.org/10.1007/BF01699475.